ESTIMATING AND MODELING TRANSPIRATION OF A MOUNTAIN MEADOW ENCROACHED BY CONIFERS USING SAP FLOW MEASUREMENTS

A Thesis

presented to

the Faculty of California Polytechnic State University,

San Luis Obispo

In Partial Fulfillment

of the Requirements for the Degree

Master of Science in Environmental Sciences and Management

by

Simon Joseph Marks

December 2021

COMMITTEE MEMBERSHIP

TITLE: Estimating and Modeling Transpiration of a Mountain Meadow Encroached by Conifers Using Sap Flow Measurements

AUTHOR: Simon Joseph Marks

DATE SUBMITTED: December 2021

COMMITTEE CHAIR: Christopher Surfleet, Ph.D., PH, CPESC
Professor of Watershed Management and Hydrology

COMMITTEE MEMBER: Bwalya Malama, Ph.D.
Associate Professor of Groundwater and Soil Physics

COMMITTEE MEMBER: John Jasbinsek, Ph.D.
Professor of Geophysics

ABSTRACT

Estimating and Modeling Transpiration of a Mountain Meadow Encroached by Conifers Using Sap Flow Measurements

Simon Joseph Marks

Mountain meadows in the western USA are experiencing increased rates of conifer encroachment due to climate change and land management practices. Past research has focused on conifer removal as a meadow restoration strategy, but there has been limited work on conifer transpiration in a pre-restoration state. Meadow restoration by conifer removal has the primary goal of recovering sufficient growing season soil moisture necessary for endemic, herbaceous meadow vegetation. Therefore, conifer water use represents an important hydrologic output toward evaluating the efficacy of this active management approach. This study quantified and evaluated transpiration of encroached conifers in a mountain meadow using sap flow prior to restoration by tree removal. We report results of lodgepole pine transpiration estimates for an approximate 1-year period and an evaluation of key environmental variables influencing water use during a dry growing season.

The study was conducted at Rock Creek Meadow (RCM) in the southern Cascade Range near Chester, CA, USA. Sap flow data were collected in a sample of lodgepole pine and scaled on a per-plot basis to the larger meadow using tree survey data within a stratified random sampling design (simple scaling). These estimates were compared to a MODIS evapotranspiration (ET) estimate for the meadow. The 1-year period for transpiration estimates overlapped each of the 2019 and 2020 growing seasons partially. The response of lodgepole pine transpiration to solar radiation, air temperature, vapor pressure deficit, and volumetric soil water content was investigated by calibrating a modified Jarvis-Stewart (MJS) model to hourly sap flow data collected during the 2020 growing season, which experienced below average antecedent winter

precipitation. The model was validated using spatially different sap flow data in the meadow from the 2021 growing season, also part of a dry year. Calibration and validation were completed using a MCMC approach via the DREAM$_{(ZS)}$ algorithm and a generalized likelihood (GL) function, enabling model parameter and total uncertainty assessment. We also used the model to inform transpiration scaling for the calibration period in select plots in the meadow, which allowed comparison with simple scaling transpiration estimates.

Average total lodgepole pine transpiration at RCM was estimated between 220.57 $\pm$ 25.28 and 393.39 $\pm$ 45.65 mm for the entire campaign (mid-July 2019 to mid-August 2020) and between 100.22 $\pm$ 11.49 and 178.75 $\pm$ 20.74 mm for the 2020 partial growing season (April to mid-August). The magnitude and seasonal timing were similar to MODIS ET. The model showed good agreement between observed and predicted sap velocity for the 2020 partial growing season (RMSE = 1.25 cm h^{-1}), with meteorological variables modulating early growing season sap flow and volumetric soil water content decline imposing transpiration decrease in the late growing season. The model validation performed similarly to calibration in terms of performance metrics and the influence of meteorological variables. The consistency of the declining volumetric soil water content effect during the late growing season between periods could not be evaluated due to an abridged validation period. Overall, the implementation GL-DREAM$_{(ZS)}$ showed promise for future use in MJS models. Lastly, the model derived transpiration estimates for the 2020 partial growing season showed some of the potential utility in using the MJS model to scale sap flow at the study locale. It also highlights some of the key limitations of this approach as it is executed in the present study.

ACKNOWLEDGMENTS

This work was made possible by grants from the Sierra Institute for the Community and Environment (Taylorsville, CA, USA) under contract number GDO 19-291 and the California Board of Forestry's Monitoring Effectiveness Committee: Agreement Number 9CA04453. I express abundant gratitude to the Collins Pine Company for the use of their private land and provision of housing in support of this research. I would also like to acknowledge the Maidu People who were stewards of this research land long before our present attempts.

I would first and foremost like to thank my committee chair Dr. Chris Surfleet for providing me the opportunity to continue my studies in hydrology. Chris, this research would not have been possible without your mentorship, but also your empowerment that enabled me to explore, learn, and struggle through my first formal research project. I cannot thank you enough for your hard work and patience in supporting me. I thank my other committee members, Dr. Bwalya Malama and Dr. John Jasbinsek, for their research input. Thank you Bwalya for your feedback on modeling and thank you John for your ERT expertise. I also extend appreciation to Dr. Jasper Vrugt who provided his DREAM MATLAB package. Thank you to the many fellow students who assisted with research efforts, especially Joe Murphy, Grecia Pizano, Evan Reed, and Nick Cary. A special thank you to Tyler Davis who showed me the ropes on meadow field work/research during his time as a graduate student.

Finally, thank you to my partner Clare for your endless love, support, and encouragement of me during my graduate studies. All were needed, especially during such a difficult and trying time in the world. Last but certainly not least, thank you to my parents, sister, grandparents, and other family members for your love and support during my educational pursuits.

TABLE OF CONTENTS

LIST OF TABLES

LIST OF FIGURES

ABBREVIATIONS

amsl above mean sea level.

AR autoregressive.

CHPM compensation heat pulse method.

DBH diameter at breast height.

DREAM DiffeRential Evolution Adaptive Metropolis.

ERT electrical resistivity tomography.

ET evapotranspiration.

GL generalized likelihood.

GWD groundwater depth.

HRM heat ratio method.

MCMC Markov Chain Monte Carlo.

MJS modified Jarvis-Stewart.

ML maximum likelihood parameter estimates.

MODIS moderate resolution imaging spectroradiometer.

PBIAS percent bias.

PET potential evapotranspiration.

PM Penman-Monteith.

RCM Rock Creek Meadow.

RMSE root mean square error.

SEP skew exponential power.

SFP sap flow plot.

SLR simple linear regression.

STRS stratified random sampling.

TDR time domain reflectometry.

VPD vapor pressure deficit.

WY water year.

FREQUENT NOTATION

D_b Bark depth [L].

D_s Sapwood depth [L].

Q Volumetric sap flow [L^3 T^{-1}].

$\bar{v}_{s,n}$ Normalized average sap velocity [].

$\bar{v}_s$ Average sap velocity [L T^{-1}].

α Thermal diffusivity [L^2 T^{-1}].

ρ_b Sapwood basic density [M L^{-3}].

θ_v Volumetric soil water content [].

$f_{p,1}(r)$ sap velocity radial profile retaining constant sap velocity across the tree sapwood.

$f_{p,2}(r)$ sap velocity radial profile representing a linear decrease of sap velocity to half of its measured value at the tree heartwood-sapwood boundary.

$f_{p,3}(r)$ sap velocity radial profile representing a linear decrease of sap velocity to 0 at the tree heartwood-sapwood boundary.

m_c Sapwood moisture content [].

v_c Corrected heat velocity [L T^{-1}].

v_h Heat velocity measured by heat pulse based sap flow sensors [L T^{-1}].

v_s Sap velocity [L T^{-1}].

CHAPTER 1: INTRODUCTION

Mountain meadows comprise a small proportion of the Sierra Nevada and Cascade landscape, but their hydrologic and ecologic function make them indispensable environmental features. Among other functions, meadows promote biodiversity in forest ecosystems and enhance water storage in upper watersheds (Viers et al., 2013). The last century, however, has seen meadows in these regions degrade by conifer encroachment, referring to the replacement of meadow vegetation by conifer forest (Dailey, 2007; Stillwater Sciences, 2012; Takaoka and Swanson, 2008; Taylor, 1995; Vale, 1981). Meadow degradation typically results in drier soils with less organic matter, lowered water tables, and changes in vegetation species (Ratliff, 1985; Viers et al., 2013). The past and ongoing decline of meadows due to conifer encroachment suggest implementation of active management restoration techniques to preserve these environments (Lang and Halpern, 2007; Swanson et al., 2007; Stillwater Sciences, 2012; Surfleet et al., 2020).

One restoration approach is conifer removal, which is thought to increase both seasonal soil moisture and seasonal water table levels by reducing water losses through interception and evapotranspiration (ET) (Fie, 2018; Surfleet et al., 2019, 2020). This change in hydrology is envisioned to facilitate the return of meadow vegetation species that are largely controlled by soil water, thus encouraging biodiversity (Mitsch and Gosselink, 2000; Stillwater Sciences, 2012; Swanson et al., 2007). A holistic understanding of the hydrologic impact of conifer removal restoration requires consideration of all inputs, outputs, and storage of water within a meadow system before and after restoration. Conifer transpiration represents a water output part of the pre-restoration baseline; however, past studies have not explicitly measured this quantity.

Measuring conifer transpiration by a direct method could enable partitioning of ET in a meadow water budget and a nuanced comparison of ET before and after conifer removal restoration. Recently, Surfleet et al. (2020) published results highlighting changes in hydrology in a southern Cascades meadow 4 years following removal of lodgepole pine. Before and after restoration water budgets showed little change in soil ET suggesting relatively similar transpiration from newly established meadow vegetation compared to the removed conifers. ET was estimated based on a water balance approach from field data.

Determination of conifer transpiration also provides a basis for the amount of water that will be placed back into storage with tree removal in addition to potential water increases due to decreased canopy interception (Surfleet et al., 2020). This information would be useful in determining the capacity for meadow vegetation recovery following restoration, a primary goal of restoration efforts. Herbaceous meadow vegetation establishment is thought to be largely a function of soil water content and depth to groundwater (Hammersmark et al., 2009, 2010; Loheide and Gorelick, 2007). Meadows degraded by woody vegetation (not conifers) have shown lower ET rates relative to their restored counterparts with herbaceous vegetation, further substantiating a need for sufficient soil water availability in meadow recovery (Hammersmark et al., 2008; Loheide II and Gorelick, 2005).

Lastly, conifer transpiration measurement enables potential insights into how this quantity is modulated by the hydrologic and climatic characteristics of the meadows they encroach. This is important in the context of increasingly variable precipitation and changing snowmelt regimes in the western USA, with snow generally expected to melt earlier with warming climate (Mote et al., 2018; Musselman et al., 2017). This is relevant to mountain meadows, as they are characterized by shallow groundwater and high soil moisture, with water inputs originating from the snowpack (Lowry et al., 2011; Ratliff, 1985). Changes in snowmelt amount and timing due to climate

change has impact on the growing season length, with soil moisture expected to recede earlier seasonally (Harpold, 2016). Understanding the soil moisture modulation on meadow conifer transpiration throughout the growing season is important for future water budget evaluations of conifer encroached meadows, especially in light of anticipated increases in hydrologic variability. Climate and energy variables such as air temperature, vapor pressure deficit, and solar radiation also exert controls on conifer transpiration (e.g., Cooper et al., 2020; Link et al., 2014; Pataki et al., 2000). Similar to soil moisture control, our knowledge of climatic and energy drivers of meadow conifer transpiration is insufficient given increasing temperatures and climatic variability. Generally speaking, mountain meadows in the Sierra Nevada and southern Cascades are considered highly vulnerable to a changing climate (Albano et al., 2019; Hauptfeld et al., 2014).

Heat pulse based sap flow instruments provide a means to measure tree transpiration. The instrumentation measures sap velocity [L T^{-1}] using heat based sensors in individual trees, enabling tree and stand-scale estimates of volumetric sap flow [L^3 T^{-1}] and transpiration (Forster, 2017; Steppe et al., 2010). The conversion of sap velocity to transpiration at these spatial scales requires substantial assumptions about tree wound response to instrument installation, sapwood area, and sapwood thermal properties (Forster, 2017; Looker et al., 2016). Scaling transpiration to the stand or landscape level is typically accomplished using the average sap velocity derived from a small sample of trees coupled with an estimate of stand/landscape sapwood area (e.g., Granier et al., 1996; Moore et al., 2004; Solum, 2020; Wilson et al., 2001; Wullschleger et al., 2001). This approach assumes that tree transpiration is spatially well mixed, without consideration of environmental variables that influence tree water use (e.g., soil moisture, micro-climates) that are spatially heterogeneous.

This thesis presents results from monitored conifer sap flow in a mountain meadow prior to its restoration by tree removal. The study site, Rock Creek Meadow (RCM), is

a historical meadow located in the southern Cascade Range, which was encroached by *Pinus contorta ssp. murrayana* (lodgepole pine) at the time of the research. The goal of the work was to estimate lodgepole pine transpiration in RCM for an approximate 1-year period and to investigate environmental drivers of lodgepole pine transpiration during a dry growing season. The work features the following objectives:

1. Measure heat ratio method sap flow in a sample plot of lodgepole pine and apply data correction to address sapwood properties, probe misalignment, and tree wound response.

2. Scale sap flow data to transpiration on a per plot basis throughout the larger meadow via a simple scaling approach based on average sap velocity and tree survey data.

3. Compare the simple scaling lodgepole pine transpiration estimates to remote sensing-based moderate resolution imaging spectroradiometer (MODIS) ET estimates.

4. Calibrate and validate a MJS model to assess the response of lodgepole pine transpiration to environmental drivers and predict transpiration, both during a dry growing season.

The sap flow measurement, sap flow scaling, MODIS comparison, and MJS model presented in this work will be useful to studies that seek to study the impact of vegetation removal restoration on mountain meadows and similar environments. Future work will integrate the lodgepole pine transpiration estimates into RCM's pre-restoration water budget, as part of a larger study that will examine changes in hydrology and vegetation communities following conifer removal restoration at the meadow. To our knowledge sap flow measurement has not been applied toward a meadow restoration oriented research problem. Moreover, comparisons of sap flow

based lodgepole pine transpiration to MODIS ET estimates will allow comment on the precision of this approach, broadening the reach of this work to sap flow practitioners in general. We also hope that our use of a Markov Chain Monte Carlo (MCMC) approach via the DiffeRential Evolution Adaptive Metropolis (DREAM) algorithm and a generalized likelihood (GL) function to fit the MJS model is helpful toward Jarvis-type transpiration (and stomatal conductance) modeling efforts. As a whole, the work contributes scientifically-defensible information needed for land managers and other stakeholders to make informed restoration decisions regarding mountain meadows encroached by conifers.

CHAPTER 2: LITERATURE REVIEW

2.1 Background and Objective of Review

Changes in climate and land management decisions in the western USA have resulted in mountain meadows with increased depth to the groundwater and decreased soil moisture triggering a succession of meadow vegetation to woody plant species (Cooper et al., 2006; Loheide et al., 2009). It is well documented over the last century that mountain meadows in the Sierra Nevada and Cascade ranges have decreased drastically in quantity and quality due to conifer encroachment (Takaoka and Swanson, 2008; Taylor, 1990; Vale, 1981; Vankat and Major, 1978). *Pinus contorta ssp. murrayana* (lodgepole pine) is the prevalent conifer species encroaching meadows in these regions. Existing research suggests the number of conifer encroached meadows will increase in the future, largely due to climate change (Lubetkin et al., 2017; Miller and Halpern, 1998; Viers et al., 2013). Concerned with the pace of meadow loss, federal land managers have implemented meadow restoration strategies that include tree removal. However, the efficacy of this approach is not well understood, especially the impact of restoration on meadow hydrology. Evapotranspiration (ET) from conifer encroached meadows is crucial to understanding the water balance of these landscape features prior to restoration. Measurement of conifer sap flow can enhance the understanding of the ET component of the meadow hydrologic cycle in this degraded state.

The primary mechanism that connects encroached conifers and meadow hydrology is transpiration. Conifers typically feature as the dominant vegetation and accordingly contribute heavily toward the meadow ET flux. The amount of water used by conifers is imperative information to computing the meadow water balance and un-

derstanding the hydrologic implications of vegetation removal. Sap flow has emerged as a practical approach to approximate transpiration in larger trees and thus presents opportunity to quantify conifer transpiration in a meadow setting. A variety of sap flow methods exist; however, not all are well suited to measure sap flow in conifers such as lodgepole pine. Furthermore, sap flow methods have several potential error sources that require mitigation to ensure sound transpiration estimates for individual trees. Sap flow measurements in individual trees are scaled to approximate the landscape transpiration flux via a bottom-up approach. Transpiration, however, is spatially heterogeneous due to variability in vegetation composition, energy/climate, and soil moisture content across the larger landscape. A sap flow scaling approach would ideally incorporate all these facets, but this is typically not done.

The major objective of this literature review is to inform a sound application of sap flow methods to quantify the transpiration flux of lodgepole pine in a mountain meadow encroached by this species. The first half of the review will address mountain meadows, conifer encroachment, and the state of knowledge regarding mountain meadow ET. The second half of the review will focus on heat pulse based sap flow methods and commonly used approaches to scale sap flow measurements made in individual trees to larger land areas. An emphasis is put on potential error sources that can hinder the accuracy of these approaches. Characteristics of lodgepole pine and conifer trees relevant to sap flow measurements are also incorporated into these sections. The surveyed literature will aid interpretation of results, elucidate limitations, and highlight improvement areas for the present study.

2.2 Mountain Meadows and Conifer Encroachment

Mountain meadows are found at elevations exceeding 500 meters above mean sea level (amsl) in mountainous terrain (Viers et al., 2013; Weixelman et al., 2011).

They are ecosystems defined by a unique combination of hydrologic, vegetative, and geomorphic conditions (Viers et al., 2013). According to Weixelman et al. (2011), a broad definition of a meadow is a groundwater-dependent ecosystem type dominated by herbaceous plant species where woody vegetation may be present, which supports plants that use surface water and/or shallow groundwater at some point during the growing season. Meadows in the Cascades and Sierra Nevada often appear as small, secluded habitats and are estimated to comprise less than than 1% of the total area in this region (Viers et al., 2013). They contain biologic communities that differ from those of the surrounding forest matrix and accordingly contribute disproportionately to the biodiversity of the regions they occupy (Hickman, 1976). In addition to their role as biodiversity hubs, meadows provide functions including flood attenuation, water storage, late season baseflow, water filtration, nitrogen attenuation, and carbon sequestration (Hammersmark et al., 2008; Hill and Mitchell-Bruker, 2010; Loheide et al., 2009; Norton et al., 2011).

While mountain meadows provide many ecosystem services, they are incredibly sensitive environments to climate and land use influence. Historic livestock grazing, drainage, and other land management decisions have contributed to degradation pathways that alter the meadow hydrology, geomorphology, and/or vegetation communities. In the context of meadows, the term degradation implies that their structure and processes are altered to the point that the functions they provide to the greater landscape are impaired (Stillwater Sciences, 2012). Meadow structure and processes are largely controlled by hydrology, so degradation is typically linked to a hydrologic alteration. The most commonly documented degradation pathways for meadows in the literature include channel incision and widening (e.g., Hammersmark et al., 2008; Lindquist and Wilcox, 2000; Loheide et al., 2009; Stillwater Sciences, 2012) and invasion of meadows by upland vegetation including sagebrush scrub and conifers (e.g.,

Berlow et al., 2002; Stillwater Sciences, 2012; Ratliff, 1985; Vale, 1981; Vankat and Major, 1978).

The invasion of mountain meadows by conifer forest is a widely documented phenomenon in the western USA. Over the past century invasion has been observed in Colorado Plateau (e.g., Moore and Huffman, 2004), Rocky Mountains (e.g., Dyer and Moffett, 1999; Vale, 1978), Sierra Nevada (e.g., Helms, 1987; Millar et al., 2004; Vankat and Major, 1978), and Cascade Range (e.g., Taylor, 1990; Vale, 1981). Takaoka and Swanson (2008) investigated the change in areal extent of mountain meadows and shrub fields in the central western Cascade Range and reported the total area of these patches decreased from 5.5% of the study area in 1946 to 2.5% in 2000. Here it was observed that mesic (wetter) and xeric (drier) meadows with adjacent conifer forest most commonly underwent forest succession. Dailey (2007) reported a similar percentage of meadows lost to conifer encroachment in the Chucksney-Grasshopper complex, located in the Willamette National Forest (OR, USA), between 1946 and 2005. With regards to meadows in the Sierra Nevada, D'Antonio et al. (2002) reported that approximately 60% of meadows in Sequoia and Kings Canyon National Park and approximately 42% of meadows in the Lake Tahoe Basin, contain both saplings and seedlings of lodgepole pine.

Pinus contorta ssp. murrayanaa, henceforth lodgepole pine, is the conifer species commonly documented to invade mountain meadows in the Sierra Nevada and Cascade Range (D'Antonio et al., 2002; Helms, 1987; Taylor, 1990; Vale, 1987). In the northern Sierra Nevada, lodgepole pine typically dominate forests at elevations of about 1830 to 2400 m amsl (Fites-Kaufman et al., 2007). Lodgepole pine is also ubiquitous in the upper montane zone of the southern Cascades. Here it grows in monospecific and mixed stands with red fir (*Abies magnifica var. magnifica*), white fir (*Abies concolor*), and Jeffrey pine (*Pinus jeffreyi*) at elevations of approximately 1900 to 2200 m amsl (Parker, 1991). While the upper montane zone is where lodgepole

pine is most abundant in both these regions, the species can appear in large numbers at lower and higher elevations (lower montane and sub-alpine zones). This tree is robust to topographical and soil conditions that typically limit other conifer species. It thrives in a wide variety of topographic positions ranging from gentle slope and basins to steep slopes and ridges (Lotan and Critchfield, 1990). Lodgepole pine can grow in infertile soils, although this may limit potential growth. The species does best in moist soils, but can tolerate a wide variety of hydrologic conditions including high watertable environments with poor soil aeration (Cochran, 1972; Lotan and Critchfield, 1990; Minore, 1970). This enables lodgepole pine to strongly establish itself around the margins of mountain meadows, positioning it to encroach when provided the appropriate driver(s) (Gross and Coppoletta, 2013; Ratliff, 1985).

The transition area between meadows and conifer forest is sensitive to variation in land use and environmental factors. Climate change effects (e.g., Lubetkin et al., 2017; Millar et al., 2004; Viers et al., 2013), fire suppression (e.g., Hadley, 1999; Taylor, 1990), grazing activity (e.g., Gross and Coppoletta, 2013; Miller and Halpern, 1998; Vale, 1981; Vankat and Major, 1978), and positive feedback loops among encroaching trees and other biotic and abiotic components are four non-exclusive causes for conifer encroachment. Examples of the fourth listed cause include alteration of soil characteristics and canopy shade that facilitate tree establishment (e.g., Griffiths et al., 2005; Rice et al., 2012). In Lassen National Park (CA, USA), located closely to Rock Creek Meadow (the location for this study), conifer encroachment into meadows accelerated following cessation of grazing and burning associated with park establishment between 1916 and 1933 (Taylor, 1990). Studies that have reconstructed patterns of conifer encroachment in individual meadows have observed considerable variability in the strength of individual factors and their interaction with one another influencing invasion through space and time (Lubetkin et al., 2017; Miller and Halpern, 1998; Norman and Taylor, 2005). Generally, lower elevation meadows have a more complex

land use history than higher elevation meadows and have shown greater correlation of encroachment with land disturbances (Gross and Coppoletta, 2013; Norman and Taylor, 2005). The high variability in hypothesized drivers highlights the importance of understanding differences in physical environment, vegetation, and land management history between meadows at different scales.

Understanding the importance of climate variability across different spatial and temporal scales in promoting conifer encroachment is of current interest, as we face warming temperatures and declining snowpack in the Sierra Nevada and Cascade range (Mote et al., 2018; Reich et al., 2018; Surfleet and Tullos, 2013). Warming temperatures and reduced snow is expected to cause decreased ground and surface water inputs and increased ground and surface water losses via ET in these regions. In areas containing conifer encroached meadows where land disturbance has been historically absent (typically higher elevation meadows), climate is hypothesized as an important driver given the control it exerts on meadow hydrologic regime and growing season duration (Lubetkin et al., 2017; Miller and Halpern, 1998). For example, in a landscape-scale study of conifer encroachment into Sierra Nevada sub-alpine meadows, climate factors contributing to a drier hydrologic regime were sufficiently able to explain differences in conifer density among meadows (Lubetkin et al., 2017). The same study provided evidence that climate explained historic variation in the recruitment timing of conifers to meadows, mainly by controlling conifer seed production and establishment. More research is needed to close knowledge gaps pertaining to the relative importance of warmer temperatures versus lower snowpack in conifer establishment to accurately estimate levels of conifer invasion risk alongside climate projections. It is conservatively anticipated that with reduced hydrologic input by snow, early season soil drying will be increased and the growing season lengthened, which makes meadow environments more vulnerable to conifer invasion (Harpold,

2016; Lubetkin et al., 2017; Miller and Halpern, 1998; Petrie et al., 2016; Viers et al., 2013).

2.3 Evapotranspiration in Mountain Meadows

ET is a significant part of the meadow water balance, making a substantial return of water inputs to the atmosphere. Possible water inputs to mountain meadows, stemming mostly from snowfall, include local infiltration and recharge, recharge from the greater basin, and recharge from watercourses (Lowry et al., 2011). ET includes the water that evaporates from plant surfaces and soil (evaporation) and the water that moves from soil through plant roots eventually exiting through the stomata as water vapor (transpiration) (Allen et al., 1998; Ward and Trimble, 2016). Depending on the environment type, transpiration can be the dominant component of ET. One meta analysis found 13 studies that portioned transpiration from ET in temperate coniferous forests and found on average 55% (±15%, 1 s.d.) of ET was transpiration (Schlesinger and Jasechko, 2014). ET is controlled spatially and temporally by the dynamic inter-play between climatic, edaphic, and biotic (largely vegetation) factors. Ultimately, the variability in these factors contributes heavily to interannual or the seasonal variation of ET within and between individual meadows. This section will advance a discussion about the climatic, edaphic, and biotic (vegetative) controls that can impact ET in mountain meadow environments. The section will also discuss examples of past studies that have quantified ET for mountain meadows, including meadows encroached by conifer trees or other woody vegetation.

2.3.1 Climatic controls

ET is influenced by a variety of climatic factors. The rate of transpiration usually increases with increases in solar radiation, vapor pressure deficit, air temperature, and

wind speed. It usually decreases with increases in relative humidity, leaf wetness, and precipitation (Allen et al., 1998; Ward and Trimble, 2016). The parameters influencing transpiration do so by contributing to the total amount of energy available to be partitioned into latent heat (Moore and Heilman, 2011). Increases in the evaporation rate tend to coincide with the same climatic variables increasing the transpiration rate, as these facilitate an increased vapor pressure deficit between the evaporating surface and the surrounding atmosphere.

The high seasonality of precipitation in the Sierra Nevada and Cascades results in the driest portion of the year corresponding with the growing season. For meadow settings in these regions, the growing season is defined as the period when herbaceous plants are actively growing, typically April or May through August annually (e.g., Hammersmark et al., 2010; Loheide et al., 2009; Surfleet et al., 2019). The growing season provides meteorological conditions associated with high available energy for ET, as well as plant available soil moisture from snowmelt. Consequently, the meadow ET flux is highest with peak rates during this period relative to the rest of the year (Loheide II and Gorelick, 2005; Lucas, 2016). The control exerted by climatic variables on ET is the most pronounced when other factors that could potentially limit ET are not an issue. In meadow environments, inadequate soil water availability can constrain ET, especially the sub-process of transpiration. When soil moisture is non-limiting, the ET rate is expected to mirror the potential evapotranspiration (PET) rate, which is largely regulated by available energy (Lucas, 2016; Moore and Heilman, 2011). The actual ET rate would be expected to diverge from PET in the later months of the growing season as soil moisture dwindles and water becomes limited.

2.3.2 Edaphic controls

Soil water availability is a major constraint for ET. It is mediated by edaphic factors such as soil depth, soil water holding capacity, and soil hydraulic conductivity. Meadows are highly groundwater dependent systems and support vegetation communities using surface water or groundwater during the growing season; this is evidenced by ET induced water-table fluctuations in wet meadow environments in the Sierra Nevada and Cascade ranges (Allen-Diaz, 1991; Loheide et al., 2009; Weixelman et al., 2011). Many authors have shown that groundwater depth (GWD) is highly correlated with vegetation community type in meadow systems (Allen-Diaz, 1991; Dwire et al., 2004; Hammersmark et al., 2009; Loheide and Gorelick, 2007). Shallow watertables support wet meadow vegetation (obligate or faculative species), while deeper watertables support xeric vegetation indicative of a dry meadow. The relationships along this hydrologic gradient are further controlled by temporal fluctuations in the watertable (e.g. the period of high groundwater, rate of watertable declines, total range of GWD) during the growing season and individual plant hydrophysiology (e.g., plant oxygen and water stress tolerance) (Castelli et al., 2000; Dwire et al., 2006; Hammersmark et al., 2009; Lowry et al., 2011). Past work has shown that wet meadows generally exhibit a greater ET flux than their dry counterparts because of decreased GWD during the growing season and increased evaporation of standing water (Hammersmark et al., 2008; Loheide II and Gorelick, 2005). This suggests that ET in wet meadow environments is largely constrained by energy availability, at least throughout the period of growing season where vegetation can access groundwater.

The relative importance of the edaphic factors controlling the amount and timing of ET during the late growing season in mountain meadows is not well understood. These factors are those that influence soil water availability in the vadose zone and interactions at the capillary fringe (Loheide et al., 2005, 2009). During the late

growing season, when the watertable declines due to transpiration and groundwater discharge to streams, plant water availability is predicated on the volume of water in the unsaturated zone. For example, the volume of water available for uptake following watertable decline is greater in finer textured soils that facilitate a larger capillary fringe, stronger upward hydraulic gradient, and higher water retention in micropores relative to coarser textured soils (Loheide et al., 2009; Steinwand et al., 2006). This range of fine to coarse soils excludes high clay textured soils because these do not typically appear in meadows. The partitioning of plant water uptake between soil water and groundwater during the growing season for different watertable depths and vegetation assemblages is not extensively studied in meadow environments. One study in the Owens Valley (CA, USA) found groundwater accounted for 20 to 30% of ET from shrubs, but 60 to 80% of ET from high-cover meadows with groundwater 1 to 3 meters beneath the surface (Steinwand et al., 2006). This suggests a higher percentage of ET as groundwater use would be expected in a hydrologically functioning wet meadow, as compared to a dry meadow or one degraded by upland vegetation invasion. Edaphic variables would likely drive the variation in ET in the latter because of limited water; however, this may not be the case if the dry meadow vegetation were able to access deeper soil water (Moore and Heilman, 2011).

2.3.3 Biotic (vegetation) controls

The type, amount, and spatial distribution of vegetation assemblages ultimately cause local variation in ET across any ecosystem. This subject is poorly studied in mountain meadow environments, despite the heterogeneity of vegetation in meadows largely consequence of shrub and conifer encroachment. What follows, therefore, is a qualitative discussion of the vegetation controls that have potential to influence local variation in ET in heterogeneously vegetated meadows based on research in other

ecosystems/regions. The discussion is broken into how spatial variation in vegetation can generally influence the sub-processes of transpiration and evaporation.

With regards to transpiration, this sub-process will vary at a fine-scale if vegetation patches vary in their ability to partition available energy into latent heat and access available water (Moore and Heilman, 2011). Variation in vegetation amount and structure dictate differences in energy balance partitioning (e.g., leaf area, rooting depth); however, abiotic factors can also constrain the partitioning of energy into latent heat, such as water retention in the root zone (Litvak et al., 2010; Moore and Heilman, 2011). Differences in water availability will be recognized if differences in rooting depths or other plant hydraulic properties exist between vegetation patches (Moore and Heilman, 2011; Moore et al., 2012). For example, woody vegetation tend to root deeper than herbaceous plants (Schenk and Jackson, 2002). Soil properties and soil depth, however, can limit rooting. In a scenario where properties of the sub-surface limited rooting depth, it is possible that transpiration would be similar across the landscape despite different vegetation types because of similar available water in the root zone (Porporato et al., 2002). This ultimately is an instance where a heterogeneity in vegetation communities across the landscape do not translate into heterogeneity in transpiration.

The affect of vegetation on evaporation is generally less complex than it is on transpiration. The amount and density of vegetation ultimately impact soil evaporation and interception loss. Past studies have shown correlations between vegetation density and variations in near-ground solar radiation, soil temperature, and potential evaporation (Breshears and Ludwig, 2010; Raz-Yaseef et al., 2010; Veatch et al., 2009). Most of these works focus on the affect canopy cover has on these processes. Interception, which is also correlated with canopy cover, ultimately increases evaporation and decreases water inputs from precipitation into the system. Overall, this highlights the

potential of upland vegetation in mountain meadows to impact processes impacting the water and energy budgets of these systems.

2.3.4 ET quantification examples for mountain meadows

Few studies have quantified the ET flux for dry and wet meadows in the Sierra Nevada and Cascade Range. This state variable is typically included in the context of meadow restoration. Furthermore, no single methodology for computing ET is used across existing studies. Loheide II and Gorelick (2005) quantified daily ET for paired degraded and pond-and-plug restored meadows along Last Chance Creek in the Feather River Watershed (CA, USA) using their high-resolution evapotranspiration mapping algorithm (ETMA) derived. The study reported a peak ET flux of 1.5 to 4 mm/d in the dry meadow setting dominated by upland vegetation community (degraded) and a peak ET flux of 5 to 6.5 mm/d in the wet meadow setting dominated by sedges and rushes (restored) (Table 2.1). The approximate doubling of the daily ET flux between the degraded and restored meadows corresponded with future findings by Hammersmark et al. (2008) that pond-and-plug restored wet meadows have higher rates of ET compared to a degraded state. ET by Hammersmark et al. (2008) was calculated using the MIKE SHE modeling system. More recent work by Lucas (2016) quantified daily ET for a wet mountain meadow in the Sierra Nevada using an eddy flux station during two growing seasons (Table 2.1). Daily ET was similar to PET and ranged from 0 to 7 mm/d, with the highest rates between June and August (Figure 2.1). The ET flux quantities from the studies by Loheide II and Gorelick (2005), Hammersmark et al. (2008), and Lucas (2016) are summarized in Table 2.1.

The ET output of mountain meadows invaded by conifers has only been explored to a limited extent. Evaluation of the hydrologic impact of conifer removal on meadow

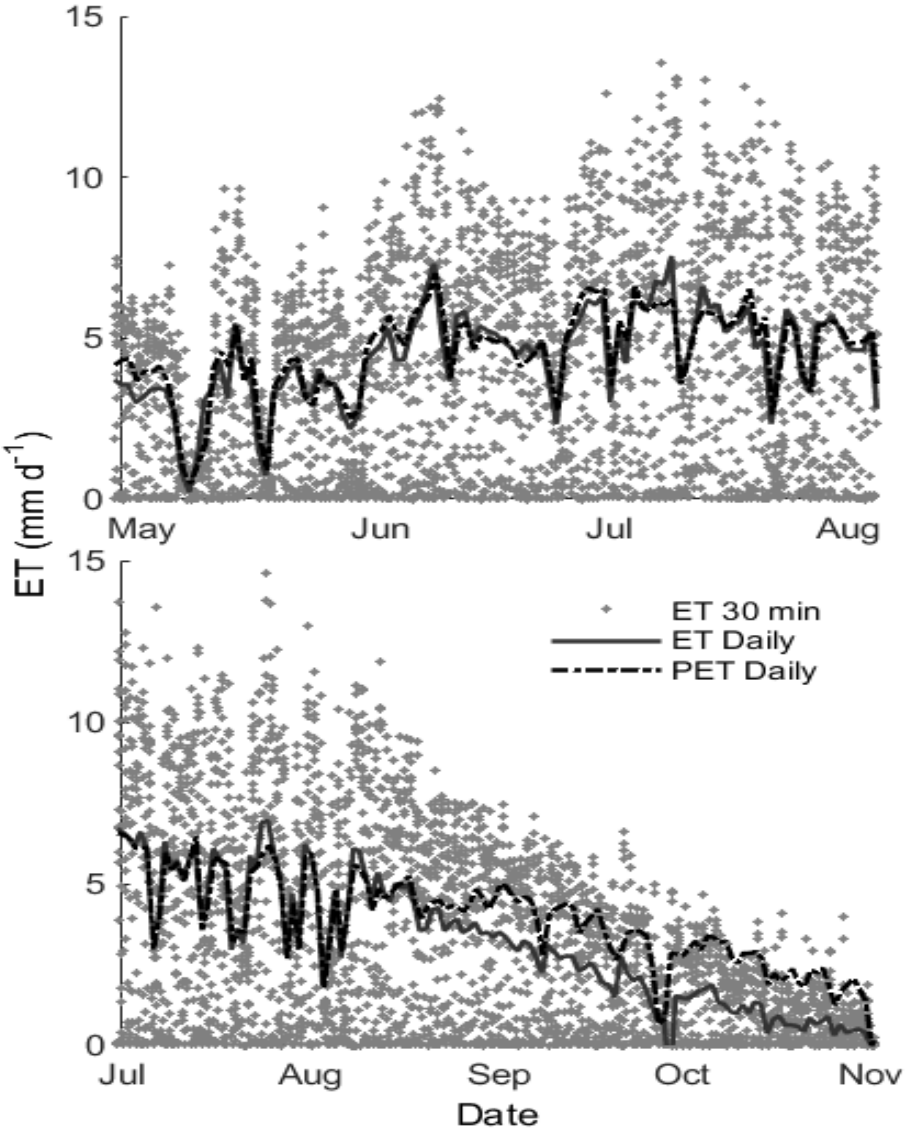

Figure 2.1: Daily and 30-minute ET values measured by the eddy flux station and plotted with daily PET for instrument deployments from April 28 through August 5, 2013 (top) and July 1 through October 1, 2014 (bottom) (excerpted from Lucas (2016)).

Table 2.1: ET flux estimates for wet, degraded, and restored mountain meadows reported in the literature.

	ET		
Study	*Wet Meadow*	*Degraded Meadow*	*Restored Meadow*
Loheide and Gorelick (2005)	–	1.5 - 4 mm/d	5 - 6.5 mm/d
Hammersmark et al. (2008)	–	419 - 530 mm/yr	626 - 661 mm/yr
Lucas (2016)	366 mm/yr	–	–
Surfleet et al. (2020)	–	457 - 482 mm/yr	399 - 425 mm/yr

hydrology was assessed by Lesh (2010) via a modeling approach. This study estimated the lodgepole pine transpiration rate during summer months with a modified version of the Penman-Monteith (PM) equation derived for conifers. The monthly rates were used in groundwater model simulations of tree removal, which suggested decreased GWD in the meadow after restoration. The accuracy of transpiration estimates was limited by data availability; the climate data used in the PM equation was not directly local to the meadow site and the lodgepole pine leaf area index may have been overestimated given the available remote sensing data. Furthermore, the tree removal groundwater simulations did not factor in the continued ET by non-woody vegetation following restoration.

The hydrologic response of mountain meadows to lodgepole pine removal, including ET, has also been assessed via direct comparisons of pre and post-restoration meadow hydrology using field measurements across years (Fie, 2018; Sanford, 2016; Surfleet et al., 2019, 2020; Van Oosbree, 2015). Surfleet et al. (2020) developed pre and post-restoration relationships for soil moisture and GWD between two southern Cascade meadow sites, one evaluated for hydrologic change due to conifer removal (treatment) and the other restored prior to the study (control). Linear regression analysis supported a consistent trend of lower soil moisture during the dry season, but higher soil moisture during the wet season for the treatment meadow relative to

its pre-restoration state. The GWD regression analysis showed an average decrease of 0.15 m (range 0.08–0.23 m) for the four years monitored post-restoration in the treatment meadow compared to before restoration. A comparison of meadow ET, computed using a soil moisture fluctuation approach similar to a single layer single step calculation, showed a decreased rate between the degraded and restored states (Table 2.1). The ET decrease after restoration was attributed to diminished interception, which supported the temporal trends in soil moisture and GWD following conifer removal.

2.4 Heat Pulse Based Sap Flow Methods

Sap flow sensors provide a means to measure transpiration in trees. The term sap flow, as it relates to transpiration, refers to the movement of fluids through the tree xylem, parallel to the axis of the tree bole. Sap flow is measured using thermometric methods based on heat convection and conduction (Swanson, 1994). Therefore, estimates of tree transpiration from sap flow are derived from measurements of heat transfer and movement within the xylem (Forster, 2017). There exist several types of methods that use heat as a tracer to measure sap flow, but in entirely different ways. These include thermal heat balance, thermal dissipation, and heat pulse methods (Forster, 2017; Smith and Allen, 1996). The thermal heat balance and dissipation method classes rely on continuous heating to measure mass heat flow, while heat pulse methods involve instantaneous heating (hence pulse) to measure heat velocity. For the purposes of this literature review, only heat pulse based methods are discussed.

Heat pulse based sap flow methods rely on a timed transport of a heat pulse from a heat source to a point downstream (upward on the plant stem) in the sapwood to approximate heat velocity (v_h) [L T^{-1}]. Generally, these methods use a heater to deliver a short heat pulse directly into the tree sapwood. The temperature increase is

measured by thermocouple(s) inserted radially into the sapwood as to calculate a v_h. Because v_h represents both convection and conduction of heat through the sapwood, v_h is converted to sap velocity (v_s) accounting for sapwood and fluid properties. Theseproperties include sapwood moisture content, basic density of sapwood and water, and specific heat capacity of sapwood and sap (Barrett et al., 1995; Becker and Edwards, 1999). Volumetric sap flow (Q) can then be estimated for an instrumented tree by multiplying v_s by the area of sapwood (Forster, 2017).

Marshall (1958) established much of the theoretical framework behind heat pulse based sap flow methods using a two probe configuration with an implanted heater and downstream temperature sensor, although the first reference to a heat pulse method was made by Huber (1932). The work developed an analytical solution to the conduction equation including convection by sap within an infinite medium given by

$$T = \frac{Q}{4\pi\alpha} exp\left(\frac{-(x - v_h t)^2 + y^2}{4\alpha t}\right), \tag{2.1}$$

where T is temperature rise measured at the thermocouple at a distance of $r = \sqrt{(x^2 + y^2)}$, Q is heat from the heat pulse, α is thermal diffusivity [L^2 T^{-1}], t is time since application of the heat pulse, and v_h is heat pulse velocity. Marshall (1958) solved Equation 2.1 using various time and temperature combinations to determine v_h. Other authors have solved Equation 2.1 for other time-temperature and sensor spacing configurations, hence yielding a variety of heat pulse based sap flow empirical methods. Notable and widely used methods include the compensation heat pulse method (CHPM), T-max method, and heat ratio method (HRM) (Fernández, 2017; Swanson, 1994). The various heat pulse based methods have been developed mainly to accommodate varying rates of sap flow among woody plants and mitigate measurement error.

The CHPM was developed by Closs (1958) and further developed by Swanson (1962) in order to consider the effect of both convection by moving sap and the thermal conduction of heat within sapwood. Swanson (1962) proposed a three-probe configuration with a central line heater between two temperature sensors spaced 5 mm upstream and 10 mm downstream. With this sensor configuration, v_h is obtained by

$$v_h = \frac{x_d + x_u}{2t_0}, \tag{2.2}$$

where x_d is the distance between the heater and the downstream temperature sensor, x_u is the distance between the heater and the upstream temperature sensor (a negative distance), and t_0 is the time after the heat pulse when the registered temperatures at the upstream and downstream sensors are equal. No term is needed for thermal properties in Equation 2.2 because the presence of an upstream probe removes the effect of sapwood heat conduction (Swanson, 1962).

The T-max method was developed by Cohen et al. (1981) with a two-probe configuration consisting of a line heater and temperature sensor located 15 mm downstream. Cohen et al. (1981) adapted the analytical theory developed by Marshall (1958) to calculate v_h by

$$v_h = \frac{\sqrt{x^2 - 4\alpha t_m}}{t_m}, \tag{2.3}$$

where x is the distance between the heater and the downstream temperature sensor, α is thermal diffusivity, and t_m is the time to maximum temperature rise measured by the downstream temperature sensor following a heat pulse.

The HRM was developed to provide better approximations of very slow rates and reverse sap flow. Both the CHPM and T-max have been shown to overestimate sap flow at low flows (Becker, 1998). Marshall (1958) laid the initial groundwork for a method to measure slow rates of flow by proposing a three-probe configuration where temperature is recorded at two equidistant points above and below an in line heater.

The work stated v_h is calculated by

$$v_h = \frac{\alpha}{x} \ln\left(\frac{\Delta T_d}{\Delta T_u}\right), \tag{2.4}$$

where α is thermal diffusivity, x is the distance from the heater to a temperature probe, ΔT_d is the temperature rise in the downstream probe, and ΔT_u is the temperature rise in the upstream probe. Burgess et al. (2001) expanded on Marshall (1958) and formally proposed the HRM with v_h calculated by Equation 2.4. This work included pertinent operational details of the HRM including probe spacing (0.6 cm), measurement time following the heat pulse, correction for tree wounding, and correction for probe misalignment.

2.5 Heat Pulse Based Sap Flow Error Sources

Sap flow at the individual tree level has been largely found to underestimate tree transpiration when using both heat pulse and continuous heat based approaches (Forster, 2017; Peters et al., 2018; Steppe et al., 2010). The underestimation is a result of errors associated with the theoretical and empirical equations that aim to directly estimate transpiration from thermal based measurements. Steppe et al. (2010) reported the least amount of error in sap flow measurements to be associated with the v_h based CHPM compared to two thermal heat balance methods, namely thermal dissipation and heat field deformation. More recently, a meta-analysis performed by Forster (2017) collected data from every peer-reviewed published paper where transpiration measured by heat pulse based methods was tested against an independent measure of plant water use. Statistical analyses showed that heat pulse methods have high precision, but a bias towards underestimating transpiration with an average error of 34.706% across all methods (Table 2.2). The study also showed that the HRM and Sapflow+ methods had the least amount of error among all heat pulse methods.

The common sources of error that contribute to this inaccuracy include insufficient measurement ranges, probe misalignment, wounding, and sapwood traits (Forster, 2017; Looker et al., 2016).

Table 2.2: A summary of descriptive statistics derived from a meta-analysis of research on the accuracy of heat pulse based methods against an independent measurement of plant water use and heat velocity measurement range for each method (excerpted from Forster (2017)).

Method	n	R^2	Slope	Deviation from slope (%)	Minimum Range (cm/h)	Maximum Range (cm/h)
All methods	104	0.822	0.860	34.706	–	–
T-max	10	0.859	0.672	36.560	5-10	>200
CHPM	59	0.723	0.863	30.611	2-5	>200
HRM	11	0.916	0.833	16.949	-10	45
Sapflow+	7	0.986	0.620	38.000	-10	>200
Dual	17	0.892	1.071	59.706	-10	>200

2.5.1 Insufficient measurement range

An insufficient or limited measurement range of v_h measured by a sap flow sensor will result in transpiration measurements over certain parts of the day or segments of the campaign that are not accurately recorded. This has the largest implication with trees that exhibit nocturnal (nighttime), slow, and reverse sap flow rates.

The significance of nighttime sap flow to total sap flow has been increasingly realized (Dawson et al., 2007; Forster, 2014). Forster (2014) conducted a synthesis of literature and unpublished data to determine the percentage of nighttime sap flow as a proportion of total daily sap flow across seasons, biomes, phylogenetic groups, and different thermometric sap flow methods. The analysis in the study concluded that on average approximately 12% of daily sap flow was comprised of nightime sap flow across all data sets. Generally, the rate of nighttime sap flow is slow (Forster,

2014, 2017). Studies on nighttime sap flow have also evidenced that reverse sap flow, where the flow direction is downwards along the trunk (also known as hydraulic lift or hydraulic redistribution), commonly occurs during the nighttime hours (Burgess and Bleby, 2006; Nadezhdina et al., 2009). With regards to conifer species, Fisher et al. (2007) observed significant nighttime sap flow coupled with small amounts of reverse sap flow for *Pinus ponderosa* in the Sierra Nevada (CA, USA).

Table 2.2 shows the limited measurement range of respective heat pulse methods. The only methods well suited to address nocturnal, slow, and reverse flow are the HRM, Sapflow+, and dual methods. The maximum range of sap flow that can be measured by a given method need also be considered. For example, the HRM becomes inaccurate with high rates of sap flow. An implementation of this method would only be accurate for tree species that do not feature high heat velocities. Of consideration in this present study are conifer trees; however, using the HRM on this tree type would likely not have accuracy issues due to insufficient measurement range. Swanson (1983) stated a v_h range of 0-35 cm hr^{-1} for conifer trees without consideration of reverse flow.

2.5.2 Probe misalignment and tree wounding

It is common that temperature probes are not situated in perfect parallel alignment with the heater in the tree sapwood during sap flow installation. As shown in Equations 2.2, 2.3, and 2.4, the calculation of v_h is heavily reliant on distances between temperature and heater probes. Errors in probe spacing, therefore, can impart large error in sap flow measurements. Depending on the direction of the misalignment, the error will result in either an over or under estimation of true sap flow (Forster, 2017; Looker et al., 2016). Further, the fewer the number of probes associated with a given method leads to a lesser chance of probe misalignment error. Slight errors in probe

misalignment can generally be corrected. For example, Burgess et al. (2001) offered a probe misalignment correction procedure for the HRM based on observed measurements over a duration where sap flow should be zero, sometimes called a zero-flow event. A zero-flow event can be induced by physically severing the stem above the sap flow measurement location or can be inferred when there is no biophysical driving force for transpiration (i.e., pre-dawn, low vapor pressure deficit, and saturated soil) (Burgess et al., 2001; Forster, 2017; Larsen et al., 2020).

While probe misalignment is often associated with the initial installation of sap flow probes, misalignment can also be dynamic over the course of the measurement campaign. If sap flow sensors are left in trees for an extensive duration, it is possible that the probe spacing will change over time due to tree growth, sapwood heterogeneity, or wood properties (Barrett et al., 1995). Larsen et al. (2020) proposed an adaptation of the method developed by Burgess et al. (2001) to introduce a dynamic probe misalignment correction for the HRM. This correction method is suited for HRM sap flow application where sensors are left installed for longer than 3 months; however, applicability may be limited by an insufficient number of zero-flow events documented over the measurement campaign.

Drilling into trees to install sap flow probes results in wounding of the adjacent vessels of the xylem. The plant responds to the wound by forming tyloses over those vessels, consequently reducing the amount of heat reaching the sapwood from the heater (Barrett et al., 1995). Previous work studying the effect of wounding on sap flow estimation indicates this reduction of heat can result in an under estimation of actual heat velocity by 50% or more (Forster, 2017; Green et al., 2003; Swanson and Whitfield, 1981). Often wounding is corrected for using wound correction factors that correspond with the width of the wound introduced to the instrumented tree. Many studies rely on published tables that list correction factors for T-max, CHPM, and

HRM (Burgess et al., 2001; Forster, 2017; Green et al., 2003; Swanson and Whitfield, 1981).

2.5.3 Sapwood traits

The conversion procedure of v_h to volumetric sap flow (Q) relies on estimation of parameters related to the tree sapwood including sapwood moisture content (m_c), sapwood basic density (ρ_b), and sapwood depth (D_s). Depending on whether the chosen heat pulse based method requires an estimation of sapwood thermal diffusivity (α) for its calculation of v_h, values of m_c and ρ_b are necessary to estimate α (Burgess et al., 2001; Vandegehuchte and Steppe, 2012). All heat pulse based sap flow methods typically utilize values of m_c and ρ_b to convert v_h to sap velocity (v_s) (Barrett et al., 1995; Burgess et al., 2001; Marshall, 1958). Sapwood cross-sectional area is typically estimated on the basis of D_s, which is needed to convert to Q. Furthermore, because sap flow probes take measurements at a singular point in the sapwood, it is imperative to consider the sapwood structure of the measured tree type that could impart variation in sap flow across the sapwood radial profile. Given the heavy reliance on sapwood traits toward the final computation of Q, it is important to be aware of potential uncertainties stemming from the sampling and methodology used to determine these parameters.

Thermal diffusivity (α) as it pertains to the calculation of v_h is the movement of heat through sapwood cell walls, intercellular space, and fluids (Forster, 2017). Many sap flow studies use a default value for α of 2.5 x 10^{-3} cm^2 s^{-1} following Burgess et al. (2001). Other studies measure and calculate α at the end of the measurement campaign from a sapwood sample. Several methods exist for calculating α including the approaches proposed by Burgess et al. (2001) and Vandegehuchte and Steppe (2012); both approaches rely on the sapwood parameters m_c and ρ_b. The work of

Looker et al. (2016), which investigated various methods for calculating α, recommended the approach of Vandegehuchte and Steppe (2012). While ρ_b is thought to remain constant over time, m_c has been shown to be dynamic on a daily and seasonal basis within and between individual trees (Forster, 2017; López-Bernal et al., 2012; Vergeynst et al., 2014). This indicates that a one time sampling of sapwood from instrumented trees at the end of a sap flow study may not adequately capture the variability in this parameter. The error in an estimation of α due to inaccurate m_c would also compound in the calculation of v_s from v_h.

Sapwood depth (D_s) is challenging to accurately measure because of heterogeneous tree structure around the bole (Forster, 2017; Quiñonez-Piñón and Valeo, 2017). The heterogeneity in D_s can result in inaccurate estimates of sapwood cross-sectional area, which is typically calculated by measurements of D_s from a tree core and diameter at breast height (DBH). It is best to sample D_s using several cores taken around the tree circumference as to capture more variability. Looker et al. (2016) found that conifer sapwood cross-sectional area estimated from D_s measured on a single core could differ from a circumferential four-core average sapwood cross-sectional area by as much as 40%.

The distribution of heartwood and sapwood in stems of lodgepole pine is not extensively reported. Overall, cross-sectional area of the sapwood relative to the total area of stemwood can be highly variable in different growth environments within species (Meinzer et al., 2005). Koch (1987) examined variations in D_s for lodgepole pine by collecting cores from three DBH tree classes (averaging 76, 152, and 228 mm) at four latitudes (37.5, 40, 42.5, and 45°) at medium elevation (relative to the given latitude) in California and Oregon. The study observed that for all latitudes, D_s was greatest at stump height and diminished sharply between stump height and 10% of tree height, but remained relatively constant between 10 and 50% of tree height. Sapwood depth averaged 24, 39, and 50 mm for the 76, 152, and 228 mm

DBH classes respectively across all latitudes at constant percentage range of total tree height (i.e., 10 to 50%). D_s was found to be negatively correlated with latitude on average. Overall, more sampling of heartwood and sapwood dimensions has been done for *Pinus contorta ssp. latifolia*, a variant of the species found in the Rockies. Several studies have reported allometric relationships between D_s or sapwood area and DBH for *latifolia*, but D_s or area are not always proportional to the tree size for this sub-species (Pataki et al., 2000; Quiñonez-Piñón and Valeo, 2017). In general conifer trees such as lodgepole pine have deep functional sapwood.

Sap flow itself can vary with radial depth in trees due to sapwood structure. The sap velocity (v_s) radial profile varies between wood types (Berdanier et al., 2016; Phillips et al., 1996). For example, conifer trees, which contain non-porous or tracheid xylem, tend to show a curved v_s radial profile with a peak below the cambium and a decreasing rate with depth toward the heartwood (Berdanier et al., 2016; Ford et al., 2004). Mark and Crews (1973) found for lodgepole pine a low flow in the vicinity of the cambium, a peak flow in the region from 30 to 42 mm from the cambium, and a tailing off of flow as the distance from the cambium increased; however, these dimensions would differ depending on tree size. Further, conifer trees feature sapwood structure consisting of alternating earlywood and latewood tissue that impart differences in hydraulic and thermal properties (Domec and Gartner, 2002). The v_s radial profile can also vary with changing environmental factors such as the variability of soil water availability and atmospheric water demand (Dragoni et al., 2009; Ford et al., 2004). The apparent variability in v_s with radial depth advocates for use of sap flow sensors with multiple measurement points distantly spaced along the sapwood profile. Authors have also developed models to estimate radial patterns in v_s, which are useful when the functional sapwood extends beyond the length of the sap flow probe (Berdanier et al., 2016; Ford et al., 2004). Besides variations in radial depths, other studies have documented variation of v_s with azimuth around the tree

bole (Čermák et al., 2004; Tateishi et al., 2008; Tsuruta et al., 2010). Multiple sap flow sensors are typically placed around a single tree to capture this variability in sap flow measurement; however, this is not always feasible due to instrument power requirements and project budget constraints.

2.6 Scaling Sap Flow to the Larger Landscape

The previous sections discussed the application of heat pulse based sap flow measurements to estimate sap velocity (v_s) and potential error sources. Point measurements of v_s are used to estimate tree level volumetric sap flow (Q). The simplest technique to obtain tree Q is to multiply the point v_s estimate by tree sapwood cross-sectional area. Tree level Q can also be approximated by integrating point v_s across the sapwood to obtain a quantity called sapwood sap flux density (J_v) and multiplying this quantity by tree sapwood cross-sectional area. Therefore, sapwood sap flux density is able to consider radial variability in v_s.

Estimates of Q traverse two more spatial levels of scale to obtain bottom-up estimates of landscape transpiration: 1) tree to the plot/stand and 2) plot to the landscape/catchment. This sequence necessitates accurate estimates of transpiration for the tree species of interest, as well as an appropriate biophysical variable for the trees distributed across the landscape to scale this flux. A number of variables have been utilized for the latter including basal area, canopy position, and leaf area; however, sapwood cross-sectional area is the most common. Overall, sap flow scaling is an error prone method. Variations in transpiration among different stands could be a major source of error for landscape-scale transpiration estimates (Ford et al., 2004; Kume et al., 2010).

Many studies scale individual tree measurements of sap flow to the plot level using the mean sap velocity or sapwood sap flux density of monitored trees coupled with an

estimate of sapwood area in the plot. Plot transpiration is estimated using sapwood sap flux density by (e.g., Granier et al., 1996; Moore et al., 2004; Wilson et al., 2001; Wullschleger et al., 2001)

$$T = \bar{J}_v \frac{A_s}{A_G}, \tag{2.5}$$

where T is transpiration [L T^{-1}], $\bar{J}_v$ is the mean plot sapwood sap flux density [L T^{-1}], A_s is the plot sapwood cross-sectional area [L^2], and A_G is the plot ground area [L^2]. Equation 2.5 shows plot transpiration estimated on the basis of mean plot sapwood sap flux density, but this term could be interchanged with one representing mean plot sap velocity. Ideal scaling from the plot scale to the landscape scale would entail multi-plot measurements for sap velocity/sapwood sap flux density and sapwood area within the larger landscape that follow the same plot approach (Ford et al., 2007; Kumagai et al., 2008). The accuracy of plot and landscape scaling is contingent upon reasonable estimates of mean plot sap velocity/sapwood sap flux density and A_s. Past studies have estimated A_s using anywhere between 5 and 20 trees (Kume et al., 2010; Vertessy et al., 1995; Wilson et al., 2001), while mean plot sap velocity/sapwood sap flux density has been approximated with measurements on 15 or fewer trees (Kume et al., 2010; Moore et al., 2004; Solum, 2020; Williams et al., 2004; Vertessy et al., 2001). Several works have focused on potential errors in plot scale transpiration resulting from the sample size of trees used to estimate these parameters (Kumagai et al., 2005b; Kume et al., 2010; Oren et al., 1998b). The cumulative results of these works suggest optimal sample sizes vary with stand environmental conditions and forest types. Ideally measurements of sap velocity/sapwood sap flux density and A_s are made in trees that represent the entire range of size distributions for a given species in the area of interest; however, in common practice sampling is stratified by selecting trees across a wide range of diameter classes. Stands or landscapes are likely to include tree size classes outside of the sampled distribution.

While the scaling approach encapsulated by Equation 2.5 uses a mean plot sapwood sap flux density/sap velocity from measured trees, other studies have shown positive relationships between sapwood sap flux density/sap velocity and DBH. This allows sapwood sap flux density/sap velocity to be estimated as a function of DBH for non-instrumented trees. Several studies have shown a linear relationship between these variables, but these are typically weak (Jung et al., 2011; Kume et al., 2010). Non-linear scaling relationships have also been considered. For example, Meinzer et al. (2005) fit sigmoidal relationships between tree sap flow and diameter and aboveground biomass for several angiosperm and conifer species, finding stronger fits for angiosperms. Overall, sigmoidal (or asymptotic) relationships between these variables suggest that beyond a certain tree size there is a 'diminishing return' of transpiration (Berry et al., 2017).

The assumption of how DBH relates to sap flux density/sap velocity impacts the estimation of plot or landscape transpiration, as well as the proportional contribution of large trees to this estimate. One notable study by Berry et al. (2017) considered the relationship between sap velocity (v_s) and DBH in the estimation of stand-level transpiration in a tropical montane forest. The work simulated the effect of different asymptotic values (DBH above which v_s is held constant) alongside a wide range of stand structure parameters (e.g., stem density and DBH distributions resulting in basal area $\sim$ 5 - 60 m^2 ha^{-1}) on plot transpiration. The work showed an overestimation of transpiration, attributed to the uncertainty in predicting v_s in the largest trees. Overestimation was achieved less frequently in scenarios where an asymptote was included in the v_s versus DBH relationship at a low value of DBH. Together these results suggest the importance of adequately sampling large trees when scaling sap flow and consideration of potential relationships between v_s and DBH that are non-linear.

The approaches described to scale sap flow over space assume that tree transpiration is spatially well mixed, but they ignore explicit consideration of environmental variables related to transpiration that are spatially heterogeneous. Most sap flow studies that scale to the larger landscape ignore edaphic and climatic spatial variability despite their impact on transpiration in certain settings. For example, a number of studies have observed decreases in sap flow with declines in soil moisture for specific tree species. Relevant to this present study, Pataki et al. (2000) observed a relationship between sap flow and both soil moisture and vapor pressure deficit for *Pinus contorta ssp. latifolia* on days without high vapor pressure deficit during a drought growing season in the Medicine Bow Mountains (WY, USA) (Figure 2.2). While this example deals with temporal variation in sap flow with soil moisture, sap flow variability has been shown alongside soil moisture heterogeneity explained by topography, soil composition, and soil depth during transitions between wet and dry periods (Tromp-van Meerveld and McDonnell, 2006). One study by Loranty et al. (2008) assessed the spatial autocorrelation in sapwood sap flux density and whole tree transpiration as a function of environmental and biological drivers (e.g., soil moisture, vapor pressure deficit, sapwood area) across a gradient from forested wetland to a forested upland near Peak Falls (WI, USA). In this work, sapwood sap flux density did not exhibit spatial autocorrelation with soil moisture; however, transpiration was spatially variable and attributed to spatial variability in sapwood area. Moreover, vapor pressure deficit was shown to effect spatial patterns in transpiration temporally. Both the upland and the wetland soil moisture conditions were deemed non-limiting to transpiration, thus explaining the lack of spatial variance in sapwood sap flux density in reference to this parameter.

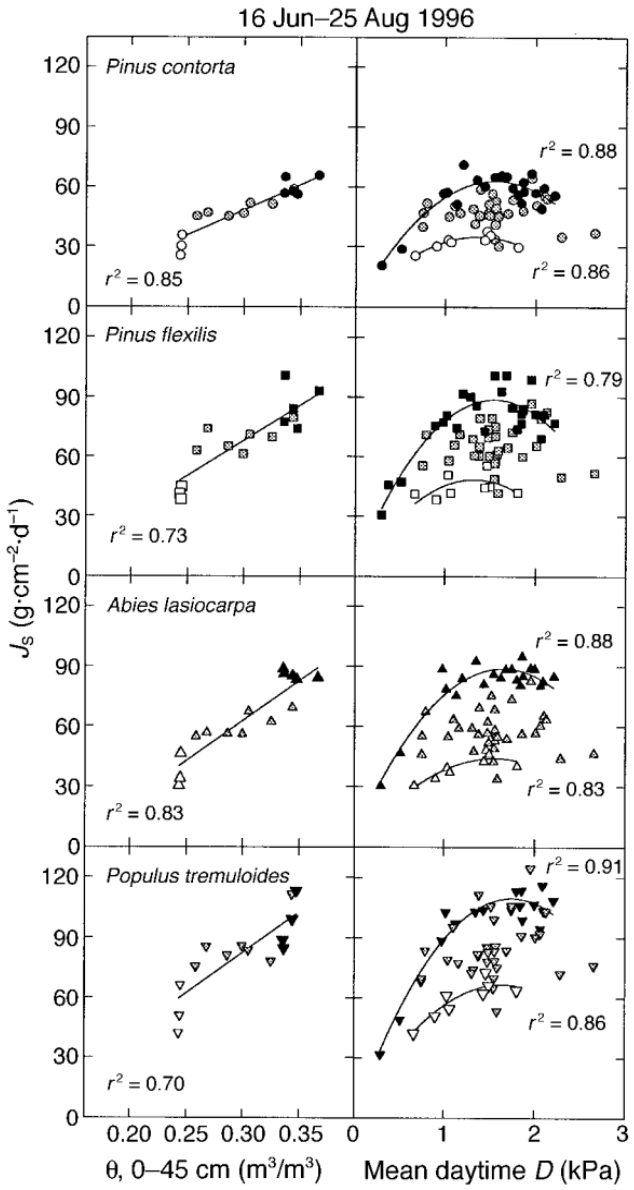

Figure 2.2: Daily sap flux density (J_s) in relation to volumetric soil moisture content (θ) and vapor pressure deficit (D). On the left, regression lines are given for the relationship between J_s and θ during the study period ($p < 0.05$). Three periods during the season are differentiated; symbol shading represents the same sample period on the right and left. For June 16-25, θ appeared relatively constant at 0.35 m^3/m^3 (filled symbols). During this period a second-order polynomial was found to describe the relationship between J_s and D ($p < 0.05$). From June 26 to August 14 (shaded symbols), θ rapidly decreased with small variations in D, such that no relationships were found in all species ($p < 0.05$). In the remaining portion of the season (open symbols), θ appeared to stabilize at $\sim$ 0.25 m^3/m^3, and a second order polynomial was again fitted to J_s vs. D ($p < 0.05$) for all species except *Pinus flexilis)* (excerpted from Pataki et al. (2000)).

2.7 Synthesis/Summary

Mountain meadows encroached by conifers, mainly lodgepole pine, are ubiquitous in the Sierra Nevada and Cascade Range. This degradation pathway detracts from the wide array of ecosystem services that meadows provide that relate to their hydrologic regime and native vegetation communities. More knowledge is needed surrounding the water balance of these systems in their degraded state in order to comprehend the potential effects of restoration techniques such as tree removal. One large component on the meadow water balance is evapotranspiration (ET); however, this has only been studied and quantified to a limited extent in meadow environments, let alone meadows encroached by conifers.

Evapotranspiration (ET) is comprised of two sub-processes, evaporation and transpiration. Transpiration would be anticipated to dominate in in a meadow environment encroached by conifers given prior studies of ET in conifer forest ecosystems. Like any ecosystem, meadow ET is controlled by interacting climatic, edpahic, and biotic (vegetative) factors. Most of the existing knowledge base surrounds wet meadows, which shows herbaceous vegetation species with high transpiration rates during the growing season when the meadow is not a water limited environment and climate/energy availability is conducive to this process. The edaphic factors governing transpiration in the late growing season are less clear, as the saturated zone may be located below the root zone. Transpiration will then be governed by vadose zone processes and the volume of water accessible here. Importantly, it is not clear whether or not conifer trees use water over the course of the growing season following patterns indicative of a non-water limited environment, such as what has been observed for wet meadows. Woody vegetation generally have deeper roots than herbaceous plants; however, the water availability may constrain conifers from reaching a maximum rate provided there is high atmospheric demand for water. A study by Loheide II and

Gorelick (2005) showed higher ET in a restored historical wet meadow compared to its degraded, dry state with woody vegetation, but the invasive woody vegetation were not conifers.

Past studies have quantified meadow ET using models, eddy flux stations, and water balances. There is no common approach to quantifying meadow ET or to our knowledge a method that has been employed to directly measure and quantify conifer transpiration in degraded meadows. Heat pulse based sap flow methods provide a relatively simple means to measure whole tree water use. All these methods calculate heat velocity (v_h), which is converted to sap velocity (v_s) and multiplied by the sapwood area to calculate volumetric sap flow (Q). Sap velocity can also be integrated/averaged across tree sapwood to match a radial profile of sap flow. Heat pulse based methods, however, are imperfect and suffer from several error sources. The heat ratio method (HRM) is able to mitigate many of these errors. It is well suited to measure conifer sap flow given its range of measurements, calibration flexibility to probe misalignment and tree wounding, and ability to measure radial variability in sap flow. This is the sap flow method used in this present study.

Sap flow measurements made in a small number of trees are typically scaled to the larger landscape using sapwood area as a scaling parameter. Many studies use an average value of sap velocity/sapwood sap flux density taken from measurements in instrumented trees; however, positive relationships have also been shown between these measurements and tree size variables (e.g., DBH) that can help scale sap flow. Any study scaling sap flow with these relatively simple approaches should carefully evaluate how v_s and sapwood area are sampled in the area of interest. Most sap flow scaling approaches ignore the heterogeneity of factors such as soil moisture and local climate, despite knowledge that these variables vary spatially and temporally with transpiration. Not every environmental setting, however, will present conditions that impart significant variability in sap flow over space. Given the potentially small

and non-representative sample of trees used to scale sap flow for the area of interest, it is good practice to compare scaled transpiration to ET approximated by another method.

Sap flow measurements executed with careful consideration of potential errors offer a means to estimate water consumption by lodgepole pine in a mountain meadow. Currently, only a few studies have estimated meadow ET in this degraded state (Fie, 2018; Sanford, 2016; Surfleet et al., 2019, 2020; Van Oosbree, 2015). The transpiration estimates produced by this present work will support efforts of evaluating the hydrologic response of a meadow degraded by conifer encroachment to tree removal restoration. The work will also apply sap flow to conifer encroached meadow for the first time and contribute to the limited knowledge base regarding meadow ET overall.

CHAPTER 3: STUDY SITE

3.1 Site Overview

The study reported in this work was conducted at Rock Creek Meadow (RCM), 40.329°, -121.088°. RCM is located near the city of Chester, California, USA in the southern Cascade Range (Figure 3.1). The site is accessed through an unpaved road off the highway and is part of the 94,000-ac Collins Almanor Forest owned by the Collins Pine Company (Chester). RCM occupies approximately 75 ha (185.3 ac) and intersects the 1524 m (5000 ft) elevation contour (Figure 3.1a). The meadow underwent restoration by removal of lodgepole pine beginning in August 2020. The majority of the lodgepole pine was removed from RCM during fall 2020, including around the measurement locations used in this study. A small portion of the RCM conifer removal, not in the primary study area, was completed during summer 2021.

RCM is largely a dry meadow based on its observed hydrology and vegetation according to the classification system devised by Weixelman et al. (2011), although mesic (wetter) meadow conditions exist along Rock Creek's riparian corridor and in openings near the stream. Dry meadows occur where the main source of water is precipitation or runoff with groundwater generally deeper than 1 m for most or all of the growing season. Vegetation for dry meadows is typically comprised of grasses, dryland sedges, and dryland rushes (Weixelman et al., 2011). The following sections describe in greater detail the climate, vegetation, hydrology, geology, and soils for the meadow.

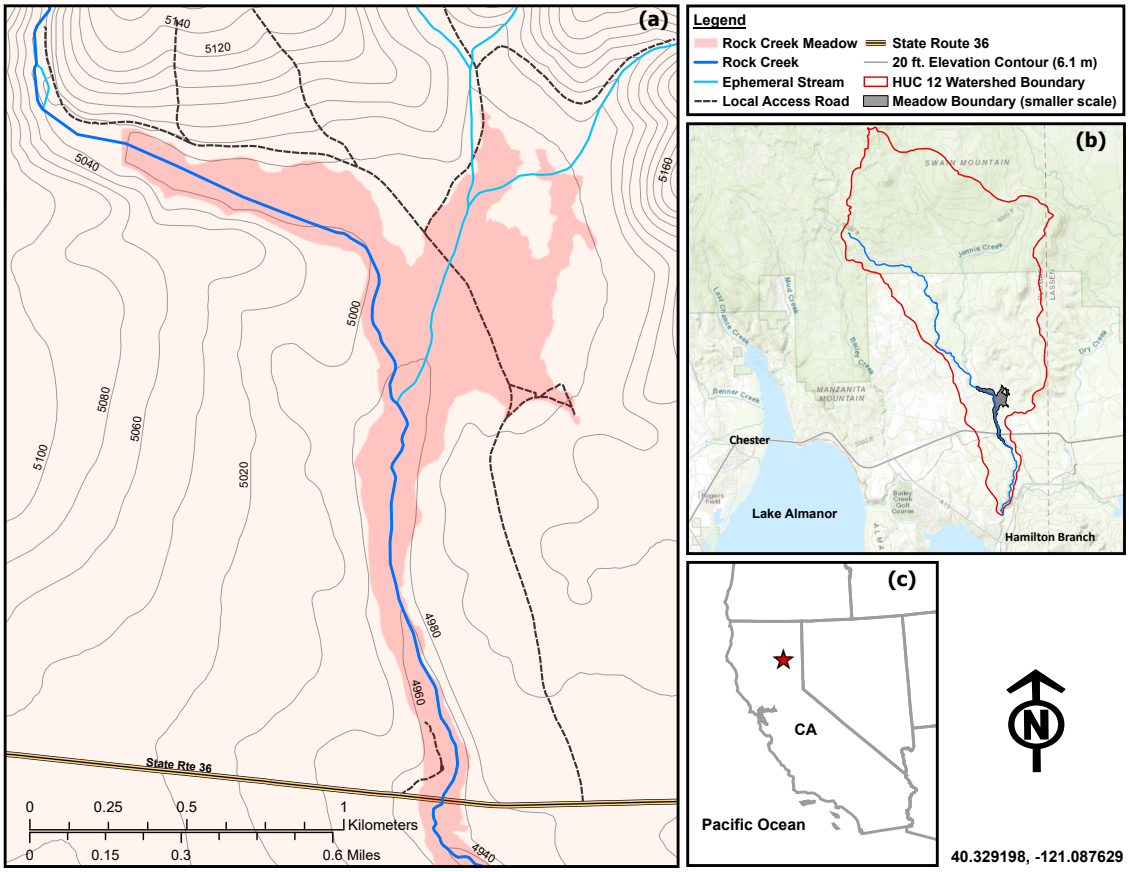

Figure 3.1: RCM study site near Chester, CA: (a) meadow boundary, watercourses, and elevation information; (b) meadow location within HUC-12 watershed; and (c) meadow location within CA, USA.

3.2 Climate

As part of the southern Cascade Range, RCM experiences a climate characterized by wet, cool winters and dry, warm summers, with large daily temperature differences. The latest seasonal normals (three-decade averages, 1981-2010) calculated from data collected by the National Oceanic and Atmospheric Administration (NOAA) climate station (station ID USC00041700) at Chester, CA are presented in Table 3.1. The normals indicate mean summer air temperature highs of 27.4 °C and mean winter lows of -5.9 °C. Winters (DJF) for this time period experienced on average 437 mm of precipitation (includes snow water equivalent), while summers (JJA) average 32.5 mm. Monthly normals indicate the rain and snow season occurs between October and May, with average precipitation greater than 44 mm in each of these months. Average yearly precipitation summed from the monthly normals is 872.5 mm. It should be noted that the elevation of the Chester NOAA station is 1381 m above mean sea level (amsl) compared to the 1524 m amsl elevation of RCM. Temperatures are likely cooler and precipitation greater during the wet season at RCM compared to Chester.

3.3 Vegetation

Plant surveys were completed at RCM along the Rock Creek riparian corridor and adjacent meadow openings as part of a timber harvest plan in July of 2017 by Collins Pine Company. The survey reported a variety of trees, shrubs, forbs, and graminoids including lodgepole pine (*Pinus contorta ssp. murrayana*), prostrate ceanothus (*Ceanothus prostratus*), Western mountain aster (*Symphyotrichum spathulatum*), and Kentucky bluegrass (*Poa pratensis*) (Appendix Table A.1). Lodgepole pine and other conifer species were most dense on the west side of the main access road prior to restoration, closest to Rock Creek watercourse, compared to the meadow

Table 3.1: Monthly climate normals (1981-2010) from data collected at the Chester, CA NOAA Station (ID USC00041700).

Month	Avg. Max Temp. (°C)	Avg. Min Temp. (°C)	Avg. Temp. (°C)	Avg. Precip. (mm)	Avg. Snowfall (mm)
Jan.	4.9	-6.4	-0.7	151.38	881.4
Feb.	7.0	-5.7	0.7	135.13	708.7
Mar.	10.3	-3.3	3.5	122.68	497.8
Apr.	13.9	-1.3	6.3	63.25	124.5
May	19.2	2.2	10.7	44.20	7.6
Jun.	24.2	5.6	14.9	19.05	2.5
Jul.	29.2	8.4	18.8	7.37	0.0
Aug.	28.8	7.2	18.0	6.10	0.0
Sep.	25.2	4.2	14.7	16.00	2.5
Oct.	18.6	0.4	9.5	51.82	17.8
Nov.	9.6	-3.2	3.2	104.90	322.6
Dec.	4.8	-5.8	-0.4	150.62	635.0

area east of the road (Figure 3.1a). Average basal area was estimated as 22.34 and 29.54 m^2/ha for the eastern and western meadow portions respectively from a tree survey performed before restoration. The meadow edge consists of mixed conifer forest including lodgepole pine, white fir (*Albies concolor*), Jeffrey pine (*Pinus jeffreyi*), and sugar pine (*Pinus lambertiana*).

3.3.1 Surface Hydrology

RCM is located in the northern portion of the Upper Feather River Watershed (UFRW) feeding the North Fork Feather River. The UFRW is a 8288 km^2 basin and includes all waters tributary to the Feather River from the headwaters downstream to Lake Oroville. At a larger scale, RCM belongs to a 7992 ha sub-watershed, 12-digit hydrologic unit (HUC-12) as delineated by the United States Geologic Survey (Figure

3.1b). Rock Creek is the main watercourse in this sub-watershed with a length of 18.5 km that forms a confluence with the Hamilton Branch discharging to Lake Almanor.

The local surface hydrology of RCM includes one intermittent stream in Rock Creek and several ephemeral streams that flow during high runoff events (Figure 3.1a). Rock Creek typically begins flow at the start of the annual snow melt (typically March or April) with flow supplemented by precipitation events during the flow season. Flows continue until snow has completely melted and similar streams have stopped flow upstream, gradually approaching no streamflow generally in either late summer or early fall. Streamflow data collected by the Plumas Corporation (Quincy, CA, USA) at a stream gauge in the southern portion of RCM showed peak hourly average flow rates in 2017, 2018, and 2019 of 1.4, 0.7, and 6.4 m^3/s respectively. The disparity in peak flows between these three years show Rock Creek's heavy reliance on the amount of snow pack in any given year.

3.4 Geology and Soils

RCM is located in the Cascade Range and Modoc Plateau geomorphic provinces. Just to the south, is the Sierra Nevada geomorphic province. The intersection of these three provinces is thought to create the fault zone beneath nearby Mount Lassen, the southernmost active volcano in the Cascades located approximately 70 km southeast from RCM. The lithology and structural continuities of the Cascade Range and Modoc Plateau are similar, with the Modoc Plateau comprised of an ancient basalt floodplain that extends southwest from Oregon and the Cascades associated with pyroclastic rock material connected to Mount Lassen (Macdonald and Gay, 1966). RCM sits a few miles east from the Almanor Fault Zone and west of the Walker Spring Fault Zone which comprise a series of normal to sinistral-normal faults which are known to offset Pliocene-age basalt bedrock (Bryant, 2000). In line with the

regional geology, the geologic material for RCM is mapped as Pleistocene or Pliocene volcanic basalt rock. Both balsaltic and rhyolitic rock, however, have been observed at the meadow site.

Two soil map units comprise RCM (Soil Survey Staff, 2020). The meadow area adjacent to Rock Creek and to the west of the main access road as the meadow widens is mapped as Mountmed loam, 0 to 2 percent slopes. The meadow area east of the main access road including the specific site for sap flow measurements is mapped as Inville very gravelly sandy loam, 0 to 5 percent slopes. Given the site geology, the soil parent materials are volcanic and alluvial material of mixed rock types. Mountmed loam is described as poorly drained with a shallow water table existing between 0 and 0.45 m of the soil surface. A typical profile of this soil series consists of a loam surface to a depth of 0.15 m, clay to a depth of 0.76 m, and stratified sand to very gravelly sandy clay loam to a depth of 1.5 m (Bochard, 2004). Inville very gravelly loam is described as well drained with a water table 2 m or below the soil surface. A typical profile of this soil series consists of a very gravelly sandy loam surface to a depth of 0.25 m, very cobbly loam to a depth of 0.53 m, extremely gravelly loam to a depth of 0.76 m, and very gravelly loam to a depth of 1.5 m (Bochard, 2004). Soil samples collected from the meadow coinciding with the Mountmed loam map unit at depths of less than 20 cm and greater than 20 cm returned textural classes (US Soil Taxonomy) of loam (31% sand, 44% silt, clay 25%) and silty clay loam (18% sand, 53% silt, 29% clay) respectively from a particle size distribution analysis. Soil samples collected from the meadow coinciding with the Inville very gravelly sandy loam map unit at the same two sampling depths returned textural classes of sandy loam (50 % sand, 37% silt, 13% clay) and loam (48% sand, 45% silt, 6% clay) respectively.

CHAPTER 4: METHODOLOGY

In order to accomplish the objectives of the present study, both field and modeling methods were adopted. The field methods include (1) measurement of lodgepole pine (*Pinus contorta ssp. murrayana*) sap flow, (2) measurement of meadow hydrometeorological conditions, and (3) a tree survey focused on lodgepole pine. The sap flow and hydrometeorological measurements served as calibration, input, and validation data for a modified Jarvis-Stewart (MJS) model linking lodgepole pine sap flow with environmental variables.

The sap flow and tree survey data were used to estimate lodgepole pine transpiration for RCM on a per plot basis in a simple scaling approach. This upscaling spanned an approximate 1-year period from mid-July 2019 to mid-August 2020, overlapping partially with two growing seasons (April through August annually). The simple scaling in the 2020 partial growing season was compared to a separate per plot basis extrapolation informed by the calibrated model in select plots. Lastly, transpiration estimates from the simple scaling were compared to a moderate resolution imaging spectroradiometer (MODIS) evapotranspiration (ET) estimate for RCM. The following sections detail the sap flow theoretical foundation, field data collection, sap flow modeling, extrapolation approaches, and MODIS ET estimation.

4.1 Sap Flow Theoretical Basis

Sap flow was measured in lodgepole pine using three-probe configuration heat pulse velocity sensors (East 30 Sensors, Pullman, WA, USA). The sensor follows the design described in Burgess et al. (2001). Each sensor consisted of three 35 mm long stainless-steel needles spaced 6 mm apart. The middle needle consisted of an

Evanohm heater (Carpenter Technology Corp., Philadelphia, PA, USA). Both the downstream and upstream needles featured three 10K precision thermistor sensors positioned at distances of 5 mm, 17.5 mm, and 30 mm respectively from the probe shroud (Figure 4.1). The heater delivered a heat pulse to the tree sapwood for 8 seconds and temperature was measured at each downstream and upstream thermistor 52 seconds after heat pulse deliverance. Therefore, measurements were recorded 60 seconds after the heat pulse was released, consistent with the recommendation for measurement time made by Burgess et al. (2001).

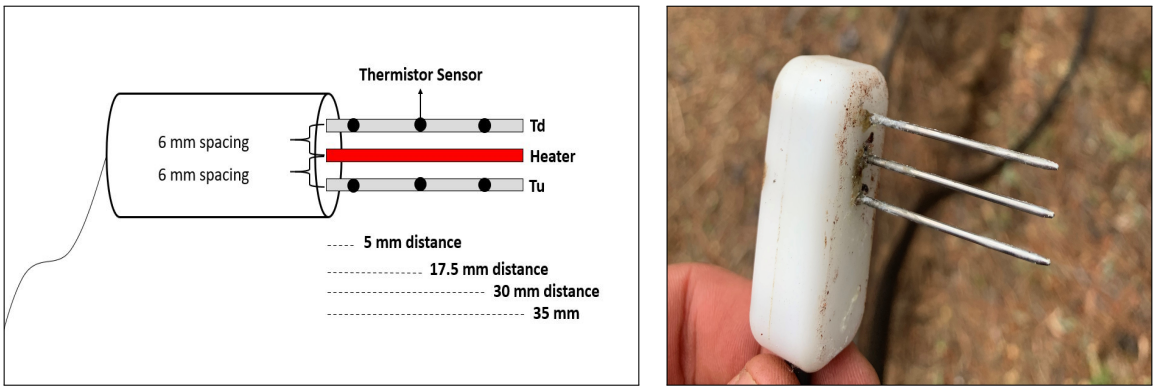

(a) (b)

Figure 4.1: (a) Schematic of the three-probe heat pulse velocity sap flow sensor manufactured by East 30 Sensors including probe and thermistor spacing dimensions. (b) Sap flow sensor manufactured by East 30 Sensors, Pullman, WA, USA.

We used the heat ratio method (HRM) proposed by Burgess et al. (2001) to determine heat velocity (v_h) [L T^{-1}]. Heat velocity is calculated using the measured ratio of the increase in temperature, following the release of a pulse of heat, at points equidistant downstream and upstream from a line heater. The calculation follows an empirical equation proposed initially by Marshall (1958) and formally for the HRM by Burgess et al. (2001):

$$v_h = \frac{\alpha}{x} \ln\left(\frac{\Delta T_d}{\Delta T_u}\right), \tag{4.1}$$

where v_h is the heat velocity (cm s^{-1}), α is the thermal diffusivity of green (fresh) sapwood (cm s^{-1}), x is the distance between the heater and either temperature probe (0.6 cm), and ΔT_d and ΔT_u are changes in temperature (60 s following heat pulse release) at equidistant points downstream and upstream respectively. Heat velocity was converted to units of cm h^{-1} by multiplying the result of Equation 4.1 by 3600. The accuracy of the v_h calculation was improved by calculating thermal diffusivity for lodgepole pine sapwood at RCM and correcting measurements for probe misalignment and tree wounding (see Section 4.3). Corrected heat velocity (v_c) is then converted to sap velocity (v_s) [L T^{-1}].

Corrected heat velocity was converted to v_s using the equation proposed by Marshall (1958):

$$v_s = \frac{\rho_b}{\rho_s}\left(m_c + \frac{c_{dw}}{c_s}\right) v_c, \tag{4.2}$$

where v_s is sap velocity (cm h^{-1}), ρ_b is the basic density of sapwood (g cm^{-3}), ρ_s is the density of sap, assumed equal to water (1.0 g cm^{-3}), m_c is water content of sapwood, c_s is the specific heat capacity of sap, assumed equal to water (4.186 J g^{-1} K^{-1}), c_{dw} is the specific heat capacity of oven-dry sapwood (J g^{-1} K^{-1}), and c_{dw}/c_s is the normalized specific heat capacity of dry sapwood (dimensionless). Normalized specific heat capacity of dry sapwood was assumed constant at 0.33 (=1.380 J g^{-1} K^{-1}/4.186 J g^{-1} K^{-1}) by Edwards and Warwick (1984), but has also been shown to be a function of temperature by Dunlap (1912). We used the equation from Dunlap (1912) to estimate c_{dw}/c_s, which has also been used in more recent works (e.g., Steppe et al., 2010; Swanson and Whitfield, 1981):

$$\frac{c_{dw}}{c_s} = 0.266 + 0.00116T, \tag{4.3}$$

where T is temperature (°C).

Sap velocity measurements were used to estimate volumetric sap flow (Q) [L^3 T^{-1}] for instrumented trees by integrating v_s across the conducting sapwood. The assumptions and calculation of this quantity are described in more detail in Section 4.7.

4.2 Sap Flow System Installation

Sap flow probes were deployed twice within RCM over the course of the study (Figure 4.2). The probes were first installed in a 25 m x 25 m plot in eastern RCM, hereafter referred to as the sap flow plot (SFP). The measurements collected in the plot are the primary sap flow data for this work and are used for model calibration and estimation of lodgepole pine transpiration for the larger meadow. The probes in the SFP were removed from their respective trees in August 2020, corresponding with the beginning of RCM's restoration. The probes were re-installed in western RCM, with the purpose of providing spatially and temporally different validation data for the calibrated model. Table 4.1 provides the data collection periods for both sap flow system deployments.

Table 4.1: Data collection periods for the two sap flow system deployments at RCM.

Deployment	Start Date-Time (GMT-7)	End Date-Time (GMT-7)
Sap Flow Plot (SFP)	2019-07-20 15:30:00	2020-08-17 07:30:00
Model Validation	2021-05-01 15:00:00	2021-07-06 11:00:00

Eight lodgepole pine were selected for instrumentation within the SFP based on their diameter at breast height (DBH) (10 cm - 40 cm) and proximity to the data logger. One probe was inserted into each tree. The location of individual trees within the plot are shown in Figure 4.2. The same tree selection criteria was applied during the second sap flow deployment; however, only six trees were instrumented.

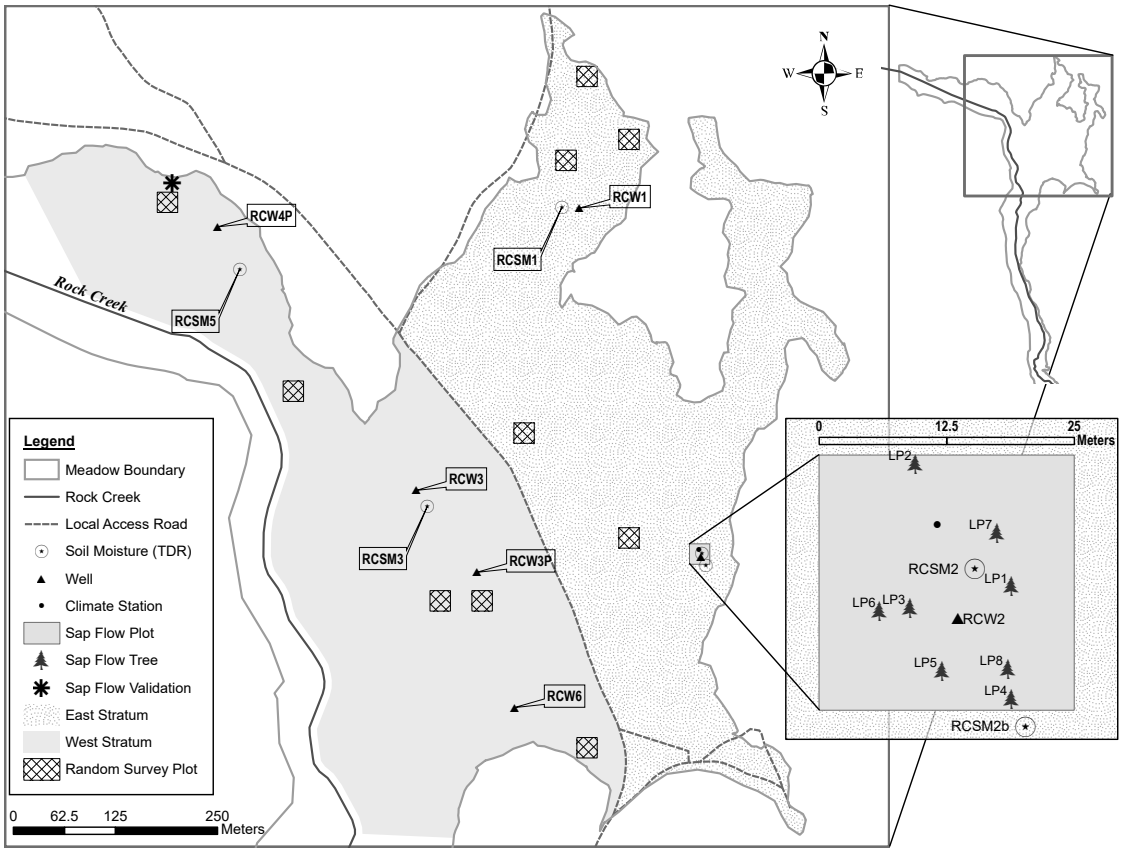

Figure 4.2: The RCM instrumented study area including the sap flow plot (SFP) and model validation site. The main map shows the location of soil moisture instruments, wells, climate station, and tree survey plots. The SFP map, displayed at a larger scale, shows the locations and IDs for the eight instrumented lodgepole pine.

The installation procedure for the sensors began by scraping off the tree's outer bark to its cambium from a 5 cm x 7.5 cm area with a putty knife. This ensured the the sensor could be installed completely flush and the shallowest thermistor would be located in sapwood. A number 55 (1.32 mm) drill bit and drilling guide was used to drill holes into the tree with 6 mm vertical needle spacing and 35 mm needle depth. Grafting wax was then applied to the sensor needles to ease insertion into the drilled holes. After ensuring the holes were clear from drilling debris, the needles were aligned with the holes and slowly inserted into the tree until flush (Figure 4.3a). Insulation was then placed around the sensor and tree to protect from any incoming solar radiation (Figure 4.3b).

(a) (b)

Figure 4.3: (a) Heat pulse velocity sap flow sensor inserted flush into a lodgepole pine tree. (b) Two sap flow instrumented lodgepole pine in the SFP wrapped with reflective insulation.

The heat pulse and temperature differential measurement sequence with the HRM sensors was repeated every 30 minutes using a CR1000 Measurement and Control Datalogger (Campbell Scientific, Logan, UT, USA) and a AM16/32 relay multiplexer

(Campbell). Both pieces of hardware were housed inside a weather-resistant enclosure and powered using a 12V, 12Ah sealed rechargeable lead-acid battery, solar panel, and 12V charging regulator (Figure 4.4a). The enclosure was mounted to a 1.6 m tall homemade stand, stabilized by counter-balancing galvanized wire tie-downs to protect it further from inclement weather and wildlife (Figure 4.4b). Sensor cables were encased in irrigation tubing and buried underground to protect against rodent damage. LoggerNet Software (Campbell) was used to communicate between the data logger and a Windows PC.

(a) (b)

Figure 4.4: (a) CR1000 datalogger and AM16/32 relay multiplexer housed inside weather resistant enclosure. (b) Home constructed stand used to protect sap flow system enclosure located near LP1 in the SFP.

4.3 Heat Velocity Data Processing

Heat pulse velocity calculations by the HRM were refined by implementing the three major correction measures recommended by Burgess et al. (2001). These three

correction measures, outlined procedurally in the subsections below, included calculation of lodgepole pine sapwood thermal diffusivity, correction for probe misalignment, and correction for tree wounding. The corrections were applied to the data in the order presented. Following these procedures, corrected heat pulse velocity data were evaluated for quality.

4.3.1 Thermal diffusivity calculation

Thermal diffusivity (α) was calculated for lodgepole pine at RCM using the methodology proposed by Vandegehuchte and Steppe (2012). To implement the calculation for α, fresh mass, oven-dry mass, and fresh volume of sapwood were determined for a sample of lodgepole pine. A sapwood core was removed from the eight instrumented trees in the SFP at the end of the measurement campaign in August 2020 using a increment borer (Haglöf, Sweden). Cores were also taken from the six instrumented trees at the model validation site and two non-instrumented trees nearby in May 2021, as to match the sample size from the SFP. Fresh volume was calculated for each core using the equation for volume of a cylinder. The fresh sample was weighed, placed in an oven at 80 °C for 72 hours, and weighed again to gather the fresh and oven-dry masses. Density of the fresh sapwood, density of the dry sapwood, and water mass were calculated from these measurements.

Thermal diffusivity (α) ($m^2\ s^{-1}$) was calculated using an equation from Bouguerra et al. (2001):

$$\alpha = \frac{k}{\rho c}, \tag{4.4}$$

where k is the thermal conductivity of the sapwood ($W\ m^{-1}\ K^{-1}$), ρ is the density of fresh sapwood ($kg\ m^{-3}$), and c is the specific heat capacity of the fresh sapwood ($J\ kg^{-1}\ K^{-1}$). Specific heat capacity of the sapwood describes its ability to store heat and

was calculated for each sample using Equation 4.5 from Burgess et al. (2001):

$$c = \hat{w}_d c_d + (1 - \hat{w}_d) c_w, \tag{4.5}$$

where $\hat{w}_d$ is the ratio of oven-dry mass and fresh mass of the sapwood sample and c_d and c_w are the specific heat capacity of dry sapwood (1200 J kg^{-1} K^{-1}) and water at 20 °C (4186 J kg^{-1} K^{-1}), respectively (Edwards and Warwick, 1984). Thermal conductivity was calculated by Equation 4.6 from Vandegehuchte and Steppe (2012):

$$k = k_w(m_c - m_{cFSP})\frac{\rho_b}{\rho_w} + 0.04186(21.0 - 20.0F_{vFSP}), \tag{4.6}$$

where k_w is the thermal conductivity of water at 20 °C (0.5984 W m^{-1} K^{-1}), m_c is the moisture content of the sapwood (water mass divided by dry sapwood mass), m_{cFSP} is the fibre saturation point (dimensionless), ρ_b and ρ_w are the density of dry sapwood and water (kg m^{-3}), and F_{vFSP} is the void fraction of the sapwood at fibre saturation point (dimensionless). Fibre saturation point values were calculated according to Roderick and Berry (2001) using Equation 4.7:

$$m_{cFSP} = 0.2\sqrt{\rho_b/\rho_w}. \tag{4.7}$$

Void fraction at fibre saturation is calculated by

$$F_{vFSP} = 1 - G\left(\frac{\rho_w}{\rho_{cw}} + m_{cFSP}\right), \tag{4.8}$$

with G being the specific gravity of sapwood (dry mass per fresh volume divided by the density of water) and ρ_{cw} the cell wall density of sapwood (1530 kg m^{-3}). The derivations of Equation 4.4 through 4.8 are explained in more detail by Bouguerra

et al. (2001), Burgess et al. (2001), Roderick and Berry (2001), and Vandegehuchte and Steppe (2012).

We used the average α determined from the 16 total cores in the v_c calculation for each tree. Average α was determined as 2.44 x 10^{-3} $\pm$ 2.3 x 10^{-4} cm^2 s^{-1}. The procedure of Vandegehuchte and Steppe (2012) also informed the values of m_c and ρ_b needed to convert v_c to v_s in Equation 4.2. A constant value of 1.00 $\pm$ 0.26 was used for m_c, while a constant value of 0.534 $\pm$ 0.109 g cm^{-3} was used for ρ_b.

4.3.2 Probe misalignment correction

We implemented a zero flow approach to correct for probe misalignment following Burgess et al. (2001). The approach assumes that $v_h = 0$ cm hr^{-1} when there is no biophysical force driving transpiration. Assuming perfect symmetry of the downstream and upstream thermistors and $v_h = 0$ cm hr^{-1}, probe placement can be calculated as:

$$x_2 = \sqrt{4\alpha t \ln\left(\frac{\Delta T_d}{\Delta T_u}\right) + x_1^2}, \tag{4.9}$$

where x_1 and x_2 are the downstream and upstream probe spacing relative to the central heater respectively (the negative direction is upstream, cm), α is thermal diffusivity of the sapwood (cm^2 s^{-1}), and t is the time after the heat pulse at which the downstream and upstream temperature are measured (60 s). Equation 4.9 was solved using downstream and upstream temperature (ΔT_d and ΔT_u) data collected during zero-flow events that occurred during the measurement campaign. Zero-flow events were flagged when it was pre-dawn, soil moisture was close to saturation, and the vapor pressure deficit was close to zero. Equation 4.9 was solved twice for each zero-flow event, first assuming x_1 was properly spaced at 0.6 cm when solving for x_2 and vice versa (x_2 = -0.6 cm). This was done for each thermistor pair at the three radial depths. The probe alignment calculations were averaged for each event and

then the median value for all averages across events was taken as the final estimated misalignment.

Equation 4.10 from Marshall (1958) was used to correct heat pulse velocity measurements using the estimated misalignment values:

$$\begin{aligned} v_{c,1} &= \frac{4\alpha t * \ln\left(\frac{\Delta T_d}{\Delta T_u}\right) - (-0.6)^2 + x_1^2}{2t(x_1 + 0.6)} \\ v_{c,2} &= \frac{4\alpha t * \ln\left(\frac{\Delta T_d}{\Delta T_u}\right) - x_2^2 + 0.6^2}{2t(0.6 - x_2)}. \end{aligned} \tag{4.10}$$

The two corrected heat velocity solutions obtained from Equation 4.10 were averaged to avoid biasing the misalignment correction in either the upstream or downstream direction. Two instrumented trees between the SFP and model validation sites had severe probe misalignment at the 17.5 mm and 30 mm measurement depths. These data were abandoned in favor of the 5 mm depth data because of the uncertainty associated with correcting badly misaligned probes (Burgess et al., 2001).

4.3.3 Tree wound correction

To correct for tree wounding we use the published correction factors and equation from Burgess et al. (2001). Wounding is corrected for by:

$$v_c = bv_h + cv_h^2 + dv_h^3, \tag{4.11}$$

where b, c, and d are coefficients for numerical solutions derived for a range of wound diameters corresponding to the -0.6, 0, and 0.6 cm probe configuration, where probes are 1.3 mm in diameter. Wounding corrections were only applied to the v_h data collected in the SFP because the data were used directly for lodgepole pine transpiration estimation. The wounding correction was unnecessary for the data collected in the

second deployment because the correction is a linear factor and is thus removed by the data normalization we applied in our modeling approach (see Section 4.6.1).

Wounding diameter ideally would be measured periodically throughout the measurement campaign to contend with the tree's dynamic response to wounding; however, this was not done to avoid destruction to tree xylem. Instead, wound diameters were measured for SFP trees following probe removal in August 2020. The average wound diameter was 2.4 $\pm$ 0.3 mm for the eight trees.

There was evidence in our SFP v_h data that the wound diameters were not as extreme as 2.4 mm for the entire measurement campaign. When the correction coefficients corresponding with 2.4 mm wounds were applied to v_h data early in measurement period (July - October 2019), v_h commonly exceeded the 35 cm/hr in all monitored trees. The exceedance of 35 cm/hr was suspicious because Swanson (1983) stated an upper v_h threshold of 35 cm/hr for conifer trees. Accordingly, we assumed a smaller wound diameter of 1.9 mm for SFP trees between probe installation in July 2019 and April 1, 2020. This was assumed based on anatomical investigations by Barrett et al. (1995) for trees with closely spaced xylem vessels similar in physiology to conifers; their study reported the total wound diameter likely extends 0.3 mm on either side of the drill hole for a given probe. The measured 2.4 mm wound diameter was assumed for all instrumented SFP trees from April, 1 2020 to August 17, 2020.

4.3.4 Missing data and quality control

We use the 30-minute SFP v_c data collected between July 21, 2019 and August 16, 2020, so the start and end of the SFP campaign would reflect complete days. The data logger exceeded memory capacity and wrapped over data from December 10, 2019 through January 10, 2020, so data is missing for this period. Our SFP measurements, therefore, cover 362 full days.

The HRM only measures $-10 < v_c < 45$ cm h^{-1}, as this is the range within which the $\Delta T_d/\Delta T_u$ ratio can be assumed accurate in Equation 4.1 (Barrett et al., 1995; Burgess et al., 2001; Forster, 2017). The majority of recorded negative heat velocities within this valid range were between -5 and 0 cm h^{-1} (96% of all negative $v_{h'}$ measurements). Furthermore, the number of negative values between -10 and -5 cm h^{-1} were disproportionately produced by the the probes in LP5 and LP6 (47% of v_c values recorded in this range). This observation is likely attributable to the more severe probe misalignment in LP5 and LP6 compared to the other trees. The data from these two trees also had more noise.

The combination of the low number of v_c observations < -5 cm h^{-1} and a disproportionate number of these measurements coming from two trees suggest the values in this range are uncharacteristic of the true reverse flow. Accordingly, we decided to remove all $v_c <$ -5 cm h^{-1} and $v_c >$ 45 cm h^{-1}. For the non-missing data collected across the eight SFP trees, a total of 5413 v_c observations were removed, 1.4% of the total available data. Missing values were linearly interpolated, as they sporadically occurred throughout the data set.

4.4 Other Environmental Data

We monitored soil moisture, groundwater, and climate data at RCM. This data collection is ongoing and part of the pre and post-restoration hydrologic quantification of the meadow. Because the present study is focused on lodgepole pine transpiration, we discuss this environmental data as it corresponds with our sap flow measurements.

4.4.1 Soil moisture monitoring

Soil moisture was monitored at seven locations in RCM, overlapping fully or in part temporally with the sap flow measurements depending on instrument installa-

tion timing and occasional instrument failure (Figure 4.2 and 4.5). Measurement set-up RCSM2 is located within the SFP, while RCSM2b is located just outside the plot (Figure 4.2). Soil moisture sensors were also installed in the vicinity of the six lodgepole pine trees part of the model validation site (RCSM6). All locations measured volumetric soil water content (θ_v) (dimensionless) by time domain reflectometry (TDR) with data logged every 30 minutes. Data from RCSM1, RCSM2b, RCSM3, and RCSM5 were only used for this study in the context of SFP data, hence the presented timeline for these set-ups do not reflect measurements collected after August 17, 2020 (Figure 4.5a). Data from RCSM6 had full temporal overlap the with sap flow measurements from the model validation site beginning in May 2021 (Figure 4.5b).

Moisture content values at the soil moisture set-ups were computed from measured dielectric (relative) permittivity using the Topp et al. (1980) equation. Topp et al. (1980) used sandy loam, two clay loams, and clay soil textural classes to determine the dependence of the dielectric constant on θ_v empirically. The textural classes of the soils at RCM are similar to those used in Topp et al. (1980), so no site-specific TDR calibration was performed. We did, however, perform a calibration-check in July 2020 using soil samples collected at 30 cm depth in the vicinity of soil moisture set-ups RCSM1, RCSM2b, and RCSM5. Volumetric soil water content calculated from the samples showed agreement with shallow soil depth TDR θ_v measurements for their respective soil moisture set-up.

Two sampling locations, RCSM1 and RCSM5, measured θ_v using 10HS Soil Moisture Smart Sensors (Decagon Devices, Pullman, WA, USA), installed at depths of 10, 30, and 100 cm. Data at these locations was collected using a HOBO USB Micro Station Data Logger (Onset Computer Corporation, Cape Cod, MA, USA). RCSM6 measured θ_v with the same sensor and logger, but only at 30 and 60 cm depths. Data at RCSM2 and RCSM3 was measured using a SoilVUE10 TDR Soil Moisture and Temperature Profile Sensor (Campbell Scientific, Logan, UT, USA), with nine

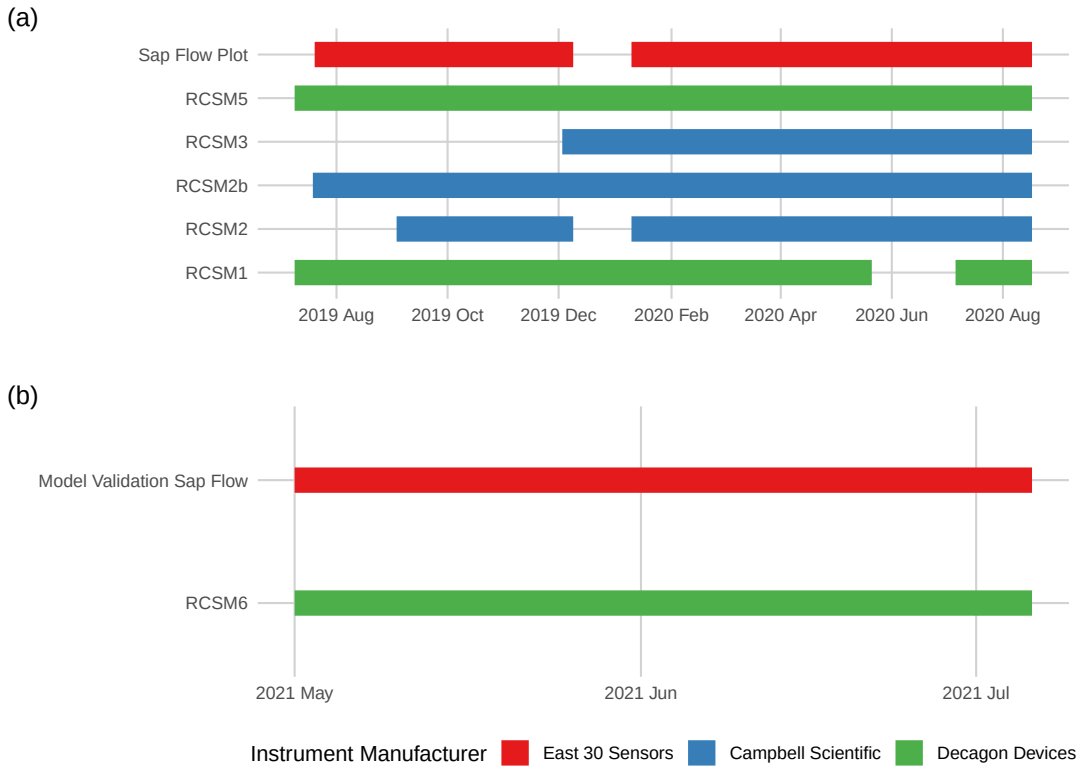

Figure 4.5: RCM soil moisture instrument measurement timeline in the context of sap flow deployments (a) SFP and (b) model validation site. The start of bars represent set-up installation and gaps reflect missing data.

sensors along a 1 m profile. Data were logged at RCSM2 and RCSM3 by CR1000 and CR300 Measurement and Control Dataloggers (Campbell) respectively. Two CS650 Soil Moisture and Temperature Sensors (Campbell) were used at the remaining sample location, RCSM2b, installed at a 40-50 cm depth with logging by a CR800 Measurement and Control Datalogger (Campbell).

The θ_v data given by the SoilVUE10 for RCSM2 gave unusually low measurements that departed heavily from what was observed in close proximity by RCSM2b. We believe the values were low at RCSM2 because of poor contact between the instrument's TDR sensors and soil due to high gravel content. We abandoned the measurements given by RCSM2 in favor of those given by RCSM2b for this study. These measurements appeared more accurate of true soil moisture conditions for the SFP and overlapped the entire SFP measurement campaign. The calibration-check performed in July 2020 using soil samples near RCSM2b showed good agreement with the TDR derived θ_v data logged by RCSM2b.

4.4.2 Groundwater monitoring

Groundwater depth (GWD) was monitored in RCM using six groundwater wells (Figure 4.2). Four of the wells (RCW1, RCW2, RW3, and RCW6) were installed by Cal Poly, while the remaining wells (RCW3P and RCW4P) were installed by Plumas Corporation (Quincy, CA, USA), a non-profit involved in RCM's restoration. One well location, RCW2, is located in the SFP. GWD measurements throughout the meadow overlaps fully or in part temporally with sap flow measurements from the the SFP depending on when well instruments were deployed and occasional instrument failure (Figure 4.6). We were not concerned with GWD data collected during the period of the model validation. Cal Poly wells were installed between July 10, 2018 and September 3, 2019, while Plumas Corporation wells were installed in July 2017.

All well instruments measured water pressure at either a 15 or 30 minute interval, which was then converted to water depth and subsequently to GWD, the depth in the soil to water from the ground surface. Table 4.2 documents the dimensions for each well.

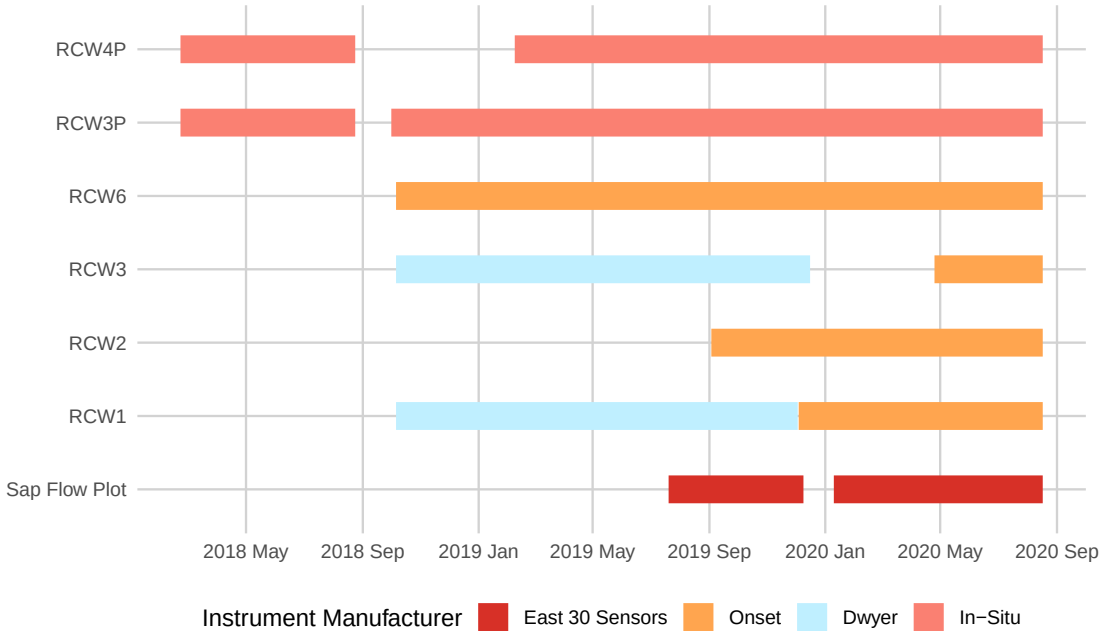

Figure 4.6: RCM groundwater well instrument timeline. Well instruments are shown on the y-axis, as well as sap flow (bottom red bar), which is included to compare the well measurement timeline to the SFP campaign. The start of a given bar represents when that instrument began sending data to its respective logger, with the exception of wells RCW3P and RCW4P, that began recording in summer of 2017.

Initially water pressure in wells RCW1 and RCW3 was measured by a Series SBLT2 Submersible Level Transmitter (Dwyer, Michigan City, IN, USA), with data logged by a EL-USB-3 Voltage Data Logger (Lascar Electronics, Erie, PA, USA). Pressure data collected by the vented pressure transducers in these wells was converted to GWD using known well depths and riser heights. The instrumentation in these wells were replaced by U20L-04 Water Level Data Loggers (Onset) during the study period due to instrument failure (Figure 4.6). These instruments were not

Table 4.2: RCM well ID codes and depths. Wells with their ID ending with "P" were installed and maintained by Plumas Corporation for the study, while all others were installed and maintained by Cal Poly.

Well ID	Depth (m)
RCW1	2.90
RCW2	1.41
RCW3	2.63
RCW6	2.90
RCW3P	1.86
RCW4P	2.16

vented, requiring adjustment of the measured water pressure by atmospheric pressure. Atmospheric pressure was measured and logged by a U20L-02 Water Level Data Logger (Onset), mounted on the climate station in RCM. Well pressure data, once calibrated, was then converted to GWD using the relationship between water pressure and known well depths and riser heights. Water pressure in wells RCW2 and RCW6 was measured and recorded by a U20L-04 Water Level Data Logger for the entire study period. The wells maintained by Plumas Corporation measured water pressure with Level TROLL 500 vented pressure transducers (In-Situ Inc., Fort Collins, CO, USA).

4.4.3 Climate monitoring

A climate station (Onset) was installed in the SFP on September 4, 2019 (Figure 4.2). The station was equipped with sensors for air temperature, relative humidity, wind speed, wind direction, barometric pressure, and incoming and outgoing shortwave solar radiation. Measurements from all instruments were recorded at a 30 minute interval by a HOBO U30 USB Weather Station Data Logger (Onset). Data time-stamped prior to the installation of the climate station at RCM was taken from an identical climate station found at another research meadow (Control Meadow),

located approximately 30 km west of RCM at a similar elevation (1463 m) (Surfleet et al., 2019, 2020). Daily precipitation data were collected from the National Oceanic and Atmospheric Administration (NOAA) climate station (station ID USC00041700) at Chester, CA. This station is part of NOAA's Global Historical Climatology Network daily (GHCNd) database (Menne et al., 2012).

4.5 Tree Survey

A tree survey was performed at RCM in July 2020. We collected measurements of lodgepole pine diameter at breast height (DBH), sapwood depth (D_s), and bark depth (D_b) in 10 random plots (each 625 m^2) part of a stratified random sampling (STRS) design. The measurements were used to develop individual relationships of D_b and D_s versus lodgepole pine DBH for RCM. These relationships were necessary to scale sap velocity measurements taken in the SFP to all individual trees measured for DBH in the random plots.

The 10 sample random plots were equally allocated between two strata delineated in RCM (Figure 4.2). The meadow access road demarcated the border between the strata. This stratification boundary was convenient, however, it was largely based on auxiliary information about site vegetation, soil moisture, and groundwater conditions. Aerial imagery of RCM suggested greater vegetation density in the portion of the meadow west of the road compared to the portion east of the road pre-restoration (Appendix Figure B.1). Soil moisture is typically higher and depth to groundwater lower in the western portion of the meadow compared to the eastern portion because of its proximity to Rock Creek watercourse. The STRS design technique was chosen to ensure that the lodgepole pine forest at RCM was adequately sampled; implementing simple random sampling may have inadvertently biased sample plots toward one

of these differing regions. Secondarily, the approach allows for potential decreases in the standard error associated with population parameter estimates.

DBH was measured for all lodgepole pine greater than 0.025 m using a standard English diameter tape in all 10 plots. Sapwood and bark depth were measured for a small representative sub-set of lodgepole pine within each random plot with an increment borer (Haglöf, Sweden) (Figure 4.7a). Three to five cores were taken per random plot, with cored trees selected to span a wide range of DBH. For all extracted samples, the delineation between sapwood and heartwood was based on the darker color of the heartwood and/or transparency of sapwood (Figure 4.7b). The visual inspection technique was consistent with methods described in other studies (e.g., Hatton et al., 1995; McDowell et al., 2008; Vertessy et al., 1995). These data were used to develop linear regression equations to predict D_b and D_s in non-cored lodgepole pine at RCM from DBH.

(a) (b)

Figure 4.7: (a) Process of coring a tree with the increment borer. (b) An example tree core used to determine sapwood depth.

Simple linear regression (SLR) was used to fit D_s and D_b versus DBH, respectively (Figure 4.8). The relationship between D_s and DBH was log-log transformed to better linearize the model and achieve homoscedascity. Prior to transformation, the model was highly heteroscedastic, showing increased variation in D_s with increased DBH. Therefore, we used the log-log model to predict D_s from DBH. Diagnostic plots used to assess satisfaction of SLR assumptions for the two models, including residual versus fitted values and quantile-quantile plots, are provided in Appendix C.

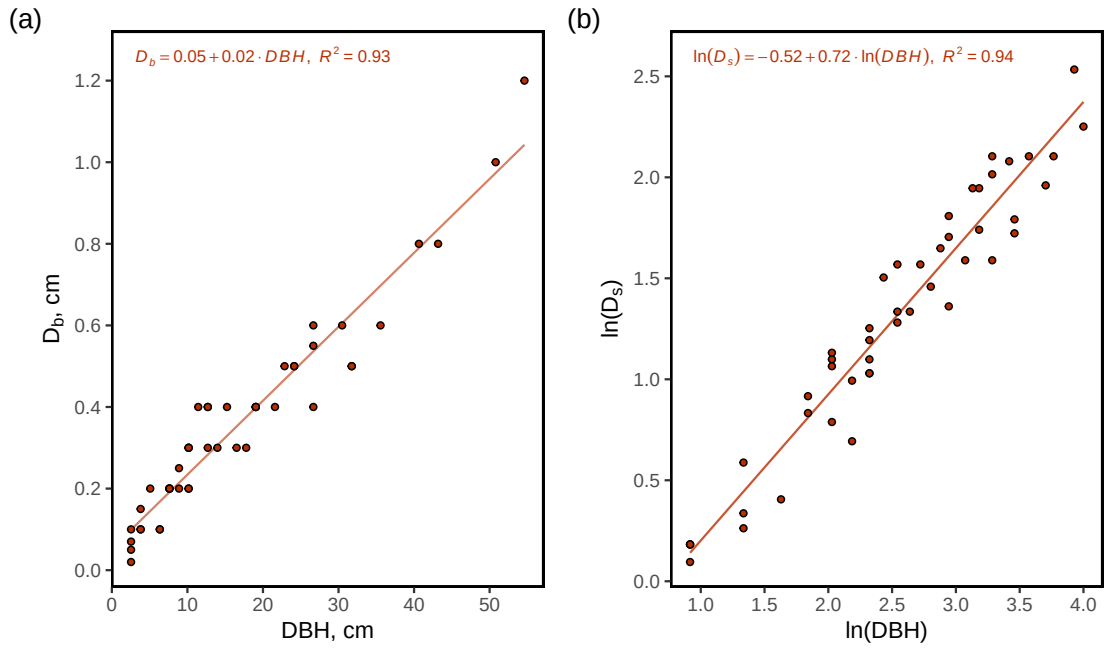

Figure 4.8: (a) Scatter plot of bark depth (D_b) versus DBH and (b) sapwood depth (D_s) versus DBH in log-log space, both including SLR equation, R^2, and line of best fit. Data (n = 47) in (a) and (b) is from *cored* trees sampled in the 10 random sample plots. The original data for DBH and D_s in (b) were in units of cm.

DBH was also measured for all lodgepole pine in the SFP. This was necessary to estimate transpiration on a per plot basis for the SFP, incorporating the non-instrumented trees. We also measured DBH for all lodgepole pine in three 25 m x 25 m plots encompassing RCSM1, RCSM3, and RCSM5. The plots containing

soil moisture instruments were used for our extrapolation approach involving the calibrated modified Jarvis-Stewart model.

4.6 Sap Flow Modeling

One objective of this work was to model lodgepole pine sap velocity (v_s) from concurrently monitored environmental variables at RCM, as to assess key drivers of transpiration during a dry growing season. We especially wanted to incorporate soil moisture content into the model, as to investigate soil water limitation on transpiration. Another objective was to use the calibrated model to scale lodgepole pine transpiration during the 2020 partial growing season (part of a dry year). This enabled exploration of how inclusion of spatially variable soil moisture in RCM influenced sap flow scaling in contrast to scaling informed only by the tree survey. Observations of v_s from the 2020 partial growing season in SFP were used to calibrate a modified Jarvis-Stewart (MJS) model. Model parameters and uncertainty were estimated using a Markov Chain Monte Carlo approach and a generalized likelihood function. Model validation was performed using v_s data from the 2021 partial growing season collected in western RCM (Figure 4.2). The following sub-sections describe the model data, formulation, calibration, and validation.

4.6.1 Model data

The MJS model was calibrated and validated using the average sap velocity ($\bar{v}_s$) from instrumented lodgepole pine trees. We computed $\bar{v}_s$ by taking the v_s from the measurement depth in each tree that was most frequently the largest (active depth), and averaging these values across trees as in Link et al. (2014) (Table 4.3). The v_s measurements within each tree taken at the 5, 17.5, and 30 mm radial depths showed high, positive correlations (Pearson r^2 values shown in Table 4.3). Correlation was

highest in each between the two measurement depths that frequently registered the highest v_s values. Using one measurement depth per tree to calculate $\bar{v}_s$ avoided redundancy.

Both model calibration and validation were performed using normalized average sap velocity ($\bar{v}_{s,n}$) (dimensionless). Normalization was performed to eliminate differences in magnitude between the $\bar{v}_s$ measurements taken at the SFP and validation locales during their respective monitored growing seasons, thus facilitating a fair evaluation of model performance. We follow the normalization procedure performed by Link et al. (2014) by dividing the hourly $\bar{v}_s$ measurements by the average of the hourly 99.5th percentile v_s values from each instrumented tree's active depth (Table 4.3). The observation time series was reduced to an hourly interval, as to diminish autocorrelation between model residuals. Hourly average sap velocity ($\bar{v}_s$) observations were normalized as follows:

$$\bar{v}_{s,n} = \bar{v}_s / \bar{v}_{s,max}, \tag{4.12}$$

where $\bar{v}_{s,max}$ is the average of the 99.5th percentile hourly v_s values from each instrumented tree from either the calibration or validation period.

Model input/forcing data consisted of concurrent hourly observations of incoming solar radiation, vapor pressure deficit (VPD), air temperature, and volumetric soil water content (θ_v). All climatic variables were measured by the climate station at the SFP. Soil moisture data were taken from RCSM2b and RCSM6 for the SFP and validation sites, respectively. Model calibration used $\bar{v}_{s,n}$ and input data collected between April 7 and August 17, 2020, while model validation used data collected between May 1 and July 6, 2021. April 7th was chosen as the start date for calibration modeling because this was the day the diurnal (maximum during the day and minimum at night) pattern indicative of transpiration returned to our sap flow measurements. There would have been a longer period of data for the validation period;

Table 4.3: Sensor correlation (Pearson r^2 coefficient showing sap velocity (v_s) correlation between measured radial depths), highest magnitude v_s radial depth (active depth), and 99.5th percentile (PCTL) v_s value taken at active depth for each instrumented lodgepole pine in the SFP and validation locales.

SFP					
Tree	Corr. (5, 17.5 mm)	Corr. (17.5, 30 mm)	Corr. (5, 30 mm)	Active depth (mm)	99.5th PCTL v_s (cm h^{-1})[a]
LP1	0.90	0.90	0.88	17.5	15.27
LP2	0.65	0.76	0.61	17.5	13.57
LP3	0.88	0.79	0.78	5	16.70
LP4	0.82	0.62	0.64	5	12.09
LP5	0.80	0.59	0.57	5	12.69
LP6	na	na	na	5	17.42
LP7	0.88	0.90	0.88	5	14.75
LP8	0.86	0.86	0.83	30	12.14
—	—	—	—	—	(14.33)*
Validation					
Tree	Corr. (5, 17.5 mm)	Corr. (17.5, 30 mm)	Corr. (5, 30 mm)	Active depth (mm)	99.5th PCTL v_s (cm h^{-1})[b]
$LP1_v$	0.96	0.92	0.92	17.5	25.15
$LP2_v$	na	na	na	5	13.81
$LP3_v$	0.83	0.82	0.81	17.5	9.13
$LP4_v$	0.95	0.94	0.94	5	24.16
$LP5_v$	0.93	0.94	0.93	17.5	12.39
$LP6_v$	0.93	0.74	0.77	5	15.26
—	—	—	—	—	(16.65)*

[a] Taken from hourly measurements during period of 04/07 - 08/17/2020.

[b] Taken from hourly measurements during period of 05/01 - 07/06/2021.

* Average of 99.5th percentile v_s from each tree used for normalization ($\bar{v}_{s,max}$).

however, the sap flow logger and probes were destroyed in the Dixie Fire in early August 2021 (damage pictured in Appendix D). Both calibration and validation data sets excluded times where solar radiation was 0 W/m^2 (nighttime) or precipitation occurred, as done in other studies implementing a MJS model (e.g., Link et al., 2014; Wang et al., 2016; Whitley et al., 2009, 2013).

4.6.2 Modified Jarvis-Stewart model

We used a modified Jarvis-Stewart (MJS) stomatal conductance model to predict $\bar{v}_{s,n}$ from environmental variables. Jarvis (1976) originally parameterized stomatal conductance in terms of empirical functions of environmental modulators using the following equation:

$$g_c = g_{max} * f_{T_L} * f_D * f_R * f_{\theta_v}, \tag{4.13}$$

where g_c is stomatal conductance [L T^{-1}], g_{max} is the maximum stomatal conductance [L T^{-1}], and f_{T_L}, f_D, f_R, f_{θ_v}, ranging 0 to 1 (dimensionless), are stress functions of leaf temperature, vapor pressure deficit (VPD), solar radiation, and volumetric soil water content (θ_v) respectively. Stewart (1988) utilized an air temperature function (f_{T_a}) in their iteration of the model, rather than a function for leaf temperature, which is why the model is commonly called the Jarvis-Stewart model.

We modify the Jarvis-Stewart model adhering to many of the same assumptions made by Link et al. (2014). The first assumption is that lodgepole pine transpiration [L T^{-1}] is proportional to the product of tree bulk canopy conductance (g_{bc}) [L T^{-1} kPa^{-1}], and the leaf-to-air vapor pressure deficit, which is assumed to be VPD:

$$T = g_{bc} * D, \tag{4.14}$$

where D is VPD (kPa). The second assumption is that lodgepole pine transpiration can also be expressed as the product of $\bar{v}_{s,n}$ (dimensionless) and a coefficient, α [L T^{-1}]:

$$T = \bar{v}_{s,n} * \alpha, \tag{4.15}$$

where α is the product of maximum $\bar{v}_s$ ($\bar{v}_{s,max}$), sapwood cross-sectional area, the profile of $\bar{v}_s$ as a function of radius, and a factor to convert α units from [L^3 T^{-1}] to [L T^{-1}] on the basis of area. The α coefficient is explicitly defined in Section 4.7.2 by Equation 4.36. Following the Jarvis-Stewart model, g_{bc} is modeled as maximum bulk canopy conductance (g_{bcmax}) reduced by environmental stress functions including f_R, f_D, f_{T_a}, and f_{θ_v}. Substituting this information into Equation 4.14 for g_{bc} and setting equivalent to Equation 4.14 results in a model for $\bar{v}_{s,n}$:

$$\bar{v}_{s,n} = \frac{g_{bcmax}}{\alpha} * D * f_D * f_{T_a} * f_R * f_{\theta_v}, \tag{4.16}$$

where $\frac{g_{bcmax}}{\alpha}$ (kPa^{-1}) is a model parameter.

The four stress functions in Equation 4.16 are empirically based and were selected from the literature. We chose functions used to predict conifer transpiration in a MJS context that best fit our calibration data set. Solar radiation stress was represented using an asymptotic function from Whitley et al. (2009):

$$f_R = \frac{R}{k_R + R} * \frac{R_{max} + k_R}{R_{max}}, \tag{4.17}$$

where R is incoming solar radiation (W/m^2), k_R is a fitting parameter (dimensionless), and R_{max} is the maximum observed R during the model calibration period (W/m^2). The VPD response was taken as an asymptotic function:

$$f_D = \frac{1}{1 + D/D_0}, \tag{4.18}$$

where D is VPD (kPa) and D_0 is a parameter describing the sensitivity of $\bar{v}_{s,n}$ to VPD (kPa) (Dang et al., 1997; Link et al., 2014; Lohammar et al., 1980; Looker et al., 2018). We use a sigmoid type function from Wang et al. (2020) for air temperature:

$$f_{T_a} = e^{\frac{-k_a(T_a - T_0)^2}{T_a + T_0}}, \tag{4.19}$$

where T_a is air temperature (°C), k_a is a fitting parameter (dimensionless), and T_0 is a parameter representing the optimal air temperature for $\bar{v}_{s,n}$ after which $\bar{v}_{s,n}$ begins to decline due to temperature stress (°C). Lastly, $\bar{v}_{s,n}$ modulation by θ_v was represented as a sigmoidal approximation of the Feddes et al. (1976) model as in Link et al. (2014):

$$f(\theta_v) = \frac{1}{1 + e^{-k_s(\theta_v - \theta_0)}}, \tag{4.20}$$

where k_s is a parameter describing the rate of decrease in $\bar{v}_{s,n}$ under limiting θ_v conditions (dimensionless), and θ_0 is the θ_v value where $\bar{v}_{s,n}$ decline is centered (dimensionless). In summary, there are seven model parameters contained in Equation 4.16: g_{bcmax}/α, k_R, D_0, k_a, T_0, k_s, and θ_0.

4.6.3 Model calibration and uncertainty analysis

The posterior distributions of the seven parameters contained in Equation 4.16 were identified using Markov Chain Monte Carlo (MCMC) simulation. We executed the MCMC approach using a version of the DiffeRential Evolution Adaptive Metropolis (DREAM) algorithm known as DREAM$_{(ZS)}$ (Laloy and Vrugt, 2012). DREAM$_{(ZS)}$ is a multi-chain MCMC simulation algorithm which yields posterior distributions of model parameters according to Bayes theorem. The algorithm implements efficient sampling schemes, lending itself well to a robust assessment of parameter and total model predictive uncertainty (e.g., errors associated with inputs/forcing data,

observations, parameters, and model structural inadequacies). The algorithm was implemented using the DREAM toolbox in MATLAB R2019a (Vrugt, 2016).

We chose the generalized likelihood (GL) function of Schoups and Vrugt (2010) to measure how well the MJS model fit the hourly $\bar{v}_{s,n}$ time series. In other words, this was the objective function of the optimization problem DREAM$_{(ZS)}$ used to explore the parameter space attempting to match MJS model predictions to observations. The GL function was selected due to its inclusion of an error model that accommodates model residual autocorrelation, non-normality, and heteroscedasticity. This was desirable given our observation data were averaged sap velocity measurements with high temporal resolution. Inclusion of the GL error model coupled with the simulation ability of DREAM$_{(ZS)}$ enabled a robust uncertainty assessment, which was of interest in fitting our model.

The GL function, described in finer detail in Schoups and Vrugt (2010), is written as:

$$L(\theta, \varphi \mid Y, I) = n \log \frac{2\sigma_\xi \omega_\beta}{\xi + \xi^{-1}} - \sum_{t=1}^{n} \log \sigma_t - c_\beta \sum_{t=1}^{n} \mid a_{\xi,t} \mid^{2/(1+\beta)}, \tag{4.21}$$

where $L(\theta, \varphi \mid Y, I)$ denotes the likelihood function that measures how well the model parameters (θ) and parameters of the error model (φ) fit the observation time series (Y), forced by input data (I). In our application of the GL function, Y represents an n x 1 vector of hourly $\bar{v}_{s,n}$ time series observations and I represents a matrix of model forcings containing hourly observations of VPD, incoming solar radiation, air temperature, and θ_v. MJS model parameters are represented by θ. The following paragraph describes the GL error model, which accounts for the remaining terms in Equation 4.21.

The GL error model partitions residuals into components accounting for autocorrelation, non-constant variance, and non-normality. The model for residual errors is

given by Schoups and Vrugt (2010) as:

$$\phi_p(B)e_t = \sigma_t a_t \text{ with } a_t \backsim (0, 1, \xi, \beta), \tag{4.22}$$

where e_t is the residual error at time t, $\phi_p(B) = 1 - \sum_{i=1}^{p} \phi_p B^i$ is an autoregressive (AR) polynomial with p AR parameters ϕ_i, B is the backshift operator ($B^i e_t = e_t - 1$), σ_t is the standard deviation at time t, and a_t is an i.i.d random error at time t with zero mean and unit standard deviation, described by a skew exponential power (SEP) density with parameters ξ and β to account for non-normality. To account for residual correlation we assumed an AR model of the third order, AR(3), with three parameters (ϕ_1, ϕ_2, and ϕ_3) inferred from the data. The AR(3) assumption was checked a-posteriori. Non-constant variance was considered by the following model adapted from Schoups and Vrugt (2010) that assumes the error standard deviations are linearly related to measured $\bar{v}_{s,n}$:

$$\sigma_t = \sigma_0 + \sigma_1 \bar{v}_{s,n}, \tag{4.23}$$

where σ_0 (intercept) and σ_1 (slope) are inferred parameters from the data. Lastly, non-normality of model residuals was handled by a SEP probability density function with SEP(0, 1, ξ, β) given by:

$$p(a_t \mid \xi, \beta) = \frac{2\sigma_\xi}{\xi + \xi^{-1}} \omega_\beta \exp\left\{-c_\beta \mid a_{\xi,t} \mid^{2/(1+\beta)}\right\} \tag{4.24}$$

and

$$a_{\xi,t} = \xi^{-sign(\mu_\xi + \sigma_\xi a_t)}(\mu_\xi + \sigma_\xi a_t), \tag{4.25}$$

where ξ and β are the skewness and kurtosis parameters, respectively, inferred from the data. The terms μ_ξ, σ_ξ, c_β, and ω_β were computed as a function of ξ and β as explained by Schoups and Vrugt (2010).

Uniform priors were assumed for all MJS model parameters (θ) and error model parameters (φ) because of the large number of $\bar{v}_{s,n}$ observations (n = 1675). Boundary conditions for each parameter are provided in Table 4.4. MJS model parameter ranges were adopted from studies that used the same empirical stress functions if provided (e.g., Link et al., 2014). Error model parameter ranges were adopted from Vrugt (2016).

Table 4.4: Boundary conditions for MJS model parameters ($\text{PARM}_{(\theta)}$) and GL error model parameters ($\text{PARM}_{(\varphi)}$).

$\text{PARM}_{(\theta)}$				**$\text{PARM}_{(\varphi)}$**			
	Units	Minimum	Maximum		Units	Minimum	Maximum
$\frac{g_{bcmax}}{\alpha}$	kPa^{-1}	0	9	σ_0	–	0	1
k_R	–	0	20	σ_1	–	-1	1
D_0	kPa	0	2	β	–	0	1
k_a	–	0	1	ξ	–	0	10
T_0	°C	20	100	ϕ_1	–	-1	1
k_s	–	0	200	ϕ_2	–	-1	1
θ_0	–	0.10	0.25	ϕ_3	–	-1	1

A total of 50000 model simulations were performed by $\text{DREAM}_{(\text{ZS})}$ to sample the parameter space, using three chains. Thinning was applied to each Markov chain to reduce autocorrelation between successively stored chain samples (Vrugt, 2016). Algorithm convergence to a stable posterior distribution was assessed using the Gelman and Rubin (1992) R-diagnostic. The final 25% of the simulations meeting convergence criteria were extracted to construct parameter posterior distributions (7502 simulations following thinning). Parameter uncertainty was obtained for the calibration data set using these samples by imputing into the MJS model and computing the 95% confidence interval of the model output. The 95% confidence interval of total

predictive uncertainty was computed using the methodology described in Schoups and Vrugt (2010) using the error model parameter posteriors.

Model calibration performance was evaluated using two different efficiency criteria:

$$RMSE = \frac{\sum_{i=1}^{N}(O_i - Y_i)^2}{N} \tag{4.26}$$

and

$$PBIAS = 100\frac{\sum_{i=1}^{N}(O_i - Y_i)}{\sum_{i=1}^{N} O_i}, \tag{4.27}$$

where N is the number of $\bar{v}_{s,n}$ observations, O_i is the ith $\bar{v}_{s,n}$ observation, and Y is predicted $\bar{v}_{s,n}$. Model predictions were computed using the maximum likelihood parameter estimates (ML) (i.e., optimal parameter set obtained from $\text{DREAM}_{(\text{ZS})}$ that maximized Equation 4.21). Root mean square error (RMSE) provides a measure of the deviation of model predictions from the observed data, while percent bias (PBIAS) measures the average tendency of the predicted values to be higher or lower than their observed counterparts.

4.6.4 Model validation

The ML parameter estimates were used to predict $\bar{v}_{s,n}$ for the validation site during the 2021 partial growing season. We computed the 95% confidence intervals of parameter and total predictive uncertainty for this data set using the same approach described for calibration. Model performance was evaluated using the efficiency criteria described in Equations 4.26 and 4.27.

4.7 Sap Flow Scaling and Transpiration Estimates

The primary objective of this study was to quantify lodgepole pine transpiration in RCM using a simple, bottom-up sap flow scaling approach (e.g., Ford et al., 2007;

Jung et al., 2011; Link et al., 2014; Moore et al., 2004; Solum, 2020). The bottom-up scaling requires estimation of volumetric sap flow (Q) [L^3 T^{-1}] at the tree, plot, and landscape levels. The following sub-sections describe the approach and assumptions used to traverse these spatial levels of scale. Our scaling was based on sap flow measurements taken in the SFP between July 21, 2019 and August 16, 2020. Another objective was to compare simple scaling lodgepole pine transpiration estimates to MODIS ET estimates, which is also described. Lastly, we describe a variation of our scaling performed using the calibrated MJS model ML estimates between April 7 and August 16, 2020.

4.7.1 Tree level sap flow

Volumetric sap flow (Q) was first estimated for the eight instrumented lodgepole pine in the SFP. This calculation requires knowledge of the tree diameter at breast height (DBH), sapwood depth (D_s) and bark depth (D_b). These dimensions were measured for the instrumented trees at the end of the SFP measurement period (Table 4.5). At each sensor location, disks (one per tree) were obtained to measure D_b and D_s (Figure 4.9a). Sapwood was delineated from heartwood by looking for a change in the wood color (Figure 4.9b). D_s was measured in all cardinal directions on the disk and then averaged for a final estimate. The assumption was made that the disks represented perfect circles so sapwood area could be calculated as the area of an annulus.

The sap velocity (v_s) measurements made at the three radial depths in the instrumented trees were used to estimate Q, assuming change in v_s with increasing sapwood depth. The v_s radial profile, while sampled at multiple depths, was not well constrained in the inner portion of the sapwood approaching the heartwood. The probe featured an innermost radial sensor depth of 30 mm; all of the instrumented

trees had sapwood exceeding this depth (Table 4.5). Therefore, we estimate Q using different assumptions for the sampled and non-sampled sapwood in the instrumented trees.

Table 4.5: Dimensions of the instrumented lodgepole pine in the SFP including diameter at breast height (DBH), bark depth (D_b), and sapwood depth (D_s).

Tree	DBH (cm)	D_b (cm)	D_s (cm)
LP1	32.0	0.7	8.4
LP2	35.5	0.8	7.8
LP3	19.0	0.3	5.2
LP4	34.0	0.5	7.6
LP5	10.3	0.1	4.0
LP6	17.8	0.2	5.1
LP7	23.5	0.4	5.5
LP8	24.1	0.3	4.9

For the sapwood captured by the three radial depth measurements, we use the weighted average approach of Hatton et al. (1990). This portion of sapwood area was divided into three annuli separated by the midpoints between the three v_s measurement depths (Figure 4.10). Volumetric sap flow for the annuli sapwood fraction (Q_1) (cm^3 h^{-1}), was calculated by

$$Q_1 = \sum_{j=1}^{3} A_j v_{s_j}, \tag{4.28}$$

where A is the cross-sectional area (cm^2) and v_s is the sap velocity measurement (cm hr^{-1}), both for annulus j.

(a) (b)

Figure 4.9: (a) Tree disks taken at the sap flow sensor location for the eight lodgepole pine trees. (b) Disk taken from LP1 with red arrow pointing at the color distinction used to differentiate between heartwood and sapwood.

Volumetric sap flow for the sapwood not sampled by the probe (Q_2) was calculated with Equation 4.29 modified from Link et al. (2014):

$$\begin{aligned} Q_2 &= \int_{r_{inner}}^{r_{outer}} 2\pi r v_s(r) dr \\ &= 2\pi v_s \int_{r_{inner}}^{r_{outer}} r f_p(r) dr, \end{aligned} \tag{4.29}$$

where r is the radial position on the cross section of the tree (not including bark), r_{inner} (cm) is the radial position of the heartwood-sapwood boundary, r_{outer} (cm) is the radial position of the innermost annulus bounding the sapwood not sampled by the probe, $v_s(r)$ is the v_s as a function of radial position in the sapwood (cm h^{-1}), v_s is the sap velocity given by the innermost measurement point (cm h^{-1}), and $f_p(r)$ is a linear function between 0 and 1 describing the radial profile of v_s between the innermost v_s measurement point and heartwood (dimensionless). The value of r_{inner}

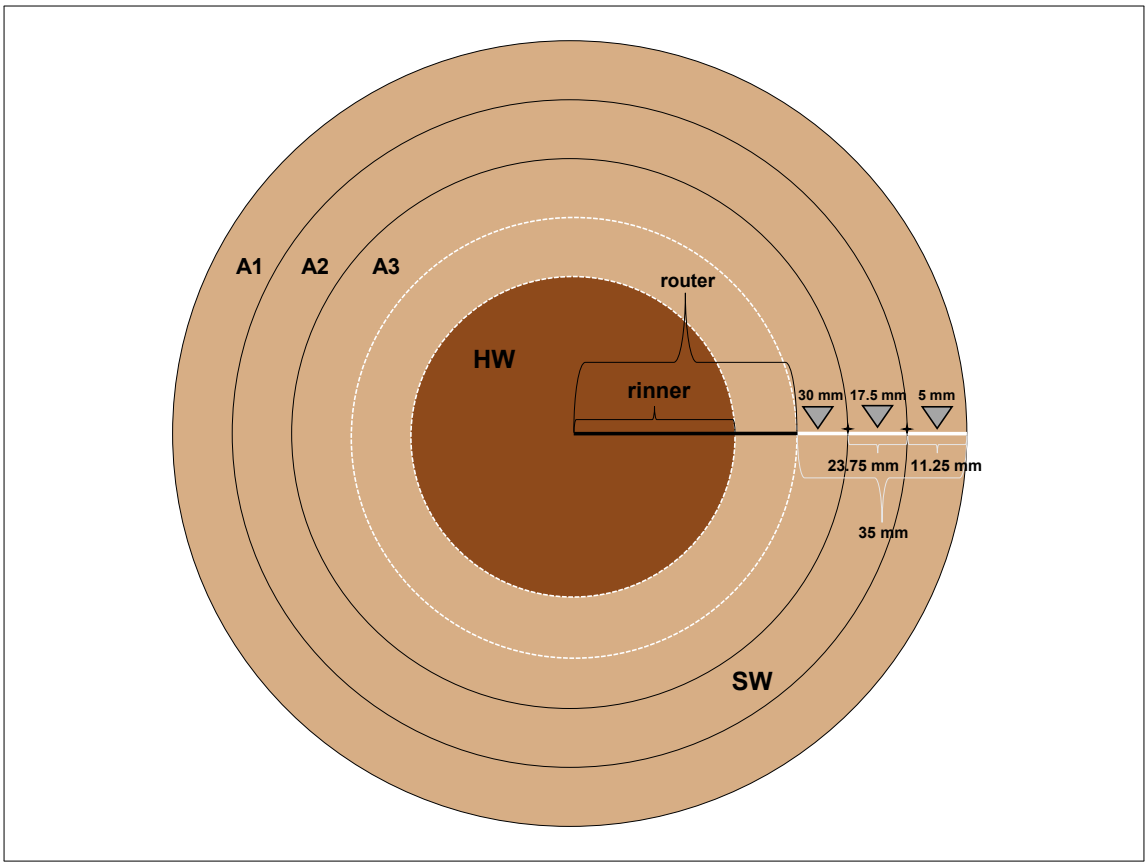

Figure 4.10: Schematic for sap flow estimation in *instrumented* trees. The light brown area represents sapwood and the dark brown area represents heartwood. The horizontal white line represents the 35 mm radial probe depth, while the triangle tips point to the three sap velocity (v_s) measurement radial depths on the probe. The annuli labeled A1, A2, and A3 demarcated by the solid black lines are the sapwood areas sampled by these measurement points. The annulus bound by the white dashed lines is the sapwood area not sampled by the probe, which Q_2 was approximated by Equation 4.29.

was calculated by

$$r_{inner} = DBH/2 - D_b - D_s, \tag{4.30}$$

where DBH is tree diameter at breast height (cm), D_b is bark depth (cm), and D_s is sapwood depth (cm). The value of r_{outer} was calculated by

$$r_{outer} = DBH/2 - D_b - D_a, \tag{4.31}$$

where D_a (cm) is the depth of the innermost annulus bounding the sapwood not sampled by the probe. For most of the instrumented trees, D_a was taken as 3.5 cm; however, for LP6 where the 17.5 mm and 30 mm measurements were discarded due to severe misalignment, D_a was taken as 1.125 cm (Figure 4.10).

The v_s radial profile was approximated following the approach used by Link et al. (2014) with $v_s(r) = v_s f_p(r)$. The profile is assumed to decline linearly with depth, based on observations in the literature that v_s is lower in the inner sapwood compared to the outer sapwood in conifers such as lodgepole pine (Berdanier et al., 2016; Ford et al., 2004; Mark and Crews, 1973). As was completed by Link et al. (2014), we employ three simple variants of a v_s profile given by

$$\begin{aligned} f_{p,1}(r) &= 1, \\ f_{p,2}(r) &= 1 + \frac{0.5}{r_{outer} - r_{inner}}(r - r_{outer}), \text{ and} \\ f_{p,3}(r) &= 1 + \frac{1}{r_{outer} - r_{inner}}(r - r_{outer}), \end{aligned} \tag{4.32}$$

where $f_{p,1}(r)$ retains constant v_s across the sapwood, $f_{p,2}(r)$ decreases v_s linearly to $0.5v_s$ at the heartwood-sapwood boundary, and $f_{p,3}(r)$ decreases v_s linearly to zero at the heartwood-sapwood boundary. The use of three profiles enabled the construction of a range of possible Q estimates for the instrumented lodgepole pine. The final

approximation of Q for each instrumented tree was calculated as the sum of Q_1 (Equation 4.28) and Q_2 (Equation 4.29).

4.7.2 Plot and meadow landscape sap flow

Sap velocity (v_s) measurements made in the eight instrumented trees were extrapolated to the SFP and other plots of the same dimension throughout the larger meadow. We extrapolated v_s measurements to the 10 random plots that were part of the tree survey (Section 4.5). The decision to scale measurements on a per plot basis rather than over the full areal extent of the meadow was predicated on uncertainty regarding the extent of lodgepole pine that would be removed from RCM during restoration.

Plot sap flow (Q_p) (cm^3 h^{-1}) was estimated by summing individual tree Q for all non-instrumented lodgepole pine (i) in a given plot:

$$Q_p = 2\pi\bar{v}_s \sum_{i=1}^{N} \int_{r_{inner,i}}^{r_{outer,i}} r f_p(r) dr, \tag{4.33}$$

where $\bar{v}_s$ is average sap velocity from the instrumented lodgepole pine in the SFP (cm h^{-1}), $r_{inner,i}$ is the radial position of the heartwood-sapwood boundary (cm), and $r_{outer,i}$ is the radial position of the bark-sapwood boundary (cm). The $\bar{v}_s$ term is the average sap velocity from instrumented trees calculated from active depth measurements, as discussed in Section 4.6.1. Equation 4.33 was calculated three times for each plot using the same v_s profiles given by Equation 4.32 for $f_p(r)$. Plot transpiration (T_p) (mm h^{-1}) was calculated from Q_p on the basis of plot ground area (625 m^2) by

$$T_p = c * Q_p, \tag{4.34}$$

where c is a conversion factor of (1/6.25 x 10^6 cm^2) (10 mm/cm).

The primary assumption made by Equation 4.33 is that $\bar{v}_s$ in non-instrumented trees declines linearly from $\bar{v}_s$ at the bark-sapwood boundary (e.g., Pausch et al., 2000; Link et al., 2014). We acknowledge that this assumption has potential inaccuracy associated with it, but it was our best attempt to capture radial variation in v_s across the sapwood without a known profile for lodgepole pine at RCM.

Lastly, the calibrated MJS model was used to inform transpiration estimates in plots (625 m^2) associated with soil moisture set-ups RCSM2b (SFP), RCSM1, RCSM3, and RCSM5. Equation 4.34 was manipulated to include normalized average sap velocity ($\bar{v}_{s,n}$) (dimensionless) predicted with the ML estimates determined for the calibrated MJS model from $DREAM_{(ZS)}$:

$$T_p = 2\pi c \bar{v}_{s,max} * \bar{v}_{s,n} \sum_{i=1}^{N} \int_{r_{inner,i}}^{r_{outer,i}} r f_p(r) dr, \tag{4.35}$$

where $\bar{v}_{s,max}$ is maximum $\bar{v}_s$ (cm h^{-1}). This maximum value is assumed to be 14.33 cm h^{-1} from Table 4.3. Writing Equation 4.35 for a single tree i and factoring out the $\bar{v}_{s,n}$ term results in the α term in Equation 4.15:

$$\alpha = 2\pi c \bar{v}_{s,max} \int_{r_{inner}}^{r_{outer}} r f_p(r) dr. \tag{4.36}$$

Thus transpiration is equal to the product of $\bar{v}_{s,n}$ and α.

Transpiration scaling informed by the calibrated MJS model was performed for the four plots between April 7 to August 16, 2020 (2020 partial growing season). Volumetric soil water content input data for this period were provided by the respective soil moisture set-up in each plot, while climate input data were given by the climate station in the SFP for all plots. Model informed plot transpiration estimates were compared to simple-scaling estimates informed by Equations 4.33 and 4.34.

4.8 MODIS ET Estimates

The simple scaling lodgepole pine transpiration estimates were compared with evapotranspiration (ET) estimates from the moderate resolution imaging spectroradiometer (MODIS) Global Terrestrial ET Product. We used the MOD16A2GF (gap-filled) Version 6 ET product, which is described in Running et al. (2019b). The product is a 8-day composite dataset produced at 500 m pixel resolution. ET is calculated under logic of the Penman-Monteith (PM) equation, informed by daily meteorological inputs along with MODIS remotely sensed data products such as leaf area index, albedo, and land cover (Running et al., 2019b).

MOD16A2GF product data were retrieved at RCM for the 8-day composites reflecting the calendar years 2019 through 2020 via the AppEEARS application (AppEEARS Team, 2020; Running et al., 2019a). Five and three 500 m pixels overlapped the eastern and western strata respectively (Appendix Figure B.2). A weighted average ET value was calculated for all of RCM and the two strata individually in Environmental Systems Research Institute's ArcMap 10.8 by determining the percentage of each pixel within each meadow area. The sap flow derived transpiration estimates were summed over 8-day windows to match the MODIS product. Our goal in comparing lodgepole pine transpiration estimates to the MODIS product was to verify the magnitude of our estimates and compare the timing of ET or transpiration between the methods.

CHAPTER 5: RESULTS

5.1 Environmental Conditions

Hydrometeorological conditions monitored at RCM concurrent with SFP measurements are displayed in Figure 5.1 and 5.2. The presented time series are extended beyond the period of the SFP measurement campaign, to capture conditions for both the 2019 and 2020 growing seasons (April through August annually). The extended period allows a full comparison between the two growing seasons, which is relevant to the comparison of sap flow measurements between monitored years.

Average daily air temperature ranged between a minimum of -7.94 °C in December 2019 and a maximum value of 21.01 °C in August 2020 (Figure 5.1a). The timing of the maximum and minimum daily averages aligned with monthly temperature averages; August 2020 was the warmest (17.55 °C), while December 2019 was the coldest (-1.02 °C). The temperature cycle monitored during the study aligned with the historic pattern for the region, which reports peak monthly temperature normals in July and August and lows in December and January. The annual cycle of vapor pressure deficit (VPD) followed that of temperature, with peaks in August 2019 and July 2020 (Figure 5.1b). Maximum average daily solar radiation occurred in late June in both years, corresponding with the summer solstice. The lowest average daily solar radiation values were measured on days with high cloud cover, often corresponding with precipitation events (Figure 5.1c). Overall, climate and energy conditions were similar between the 2019 and 2020 growing seasons (Table 5.1).

A total of 1102 mm of precipitation fell during the 2019 water year (WY) (October through September annually) overlapping with the beginning of SFP measurement, while 512 mm fell during the 2020 WY encapsulating the rest of SFP monitoring.

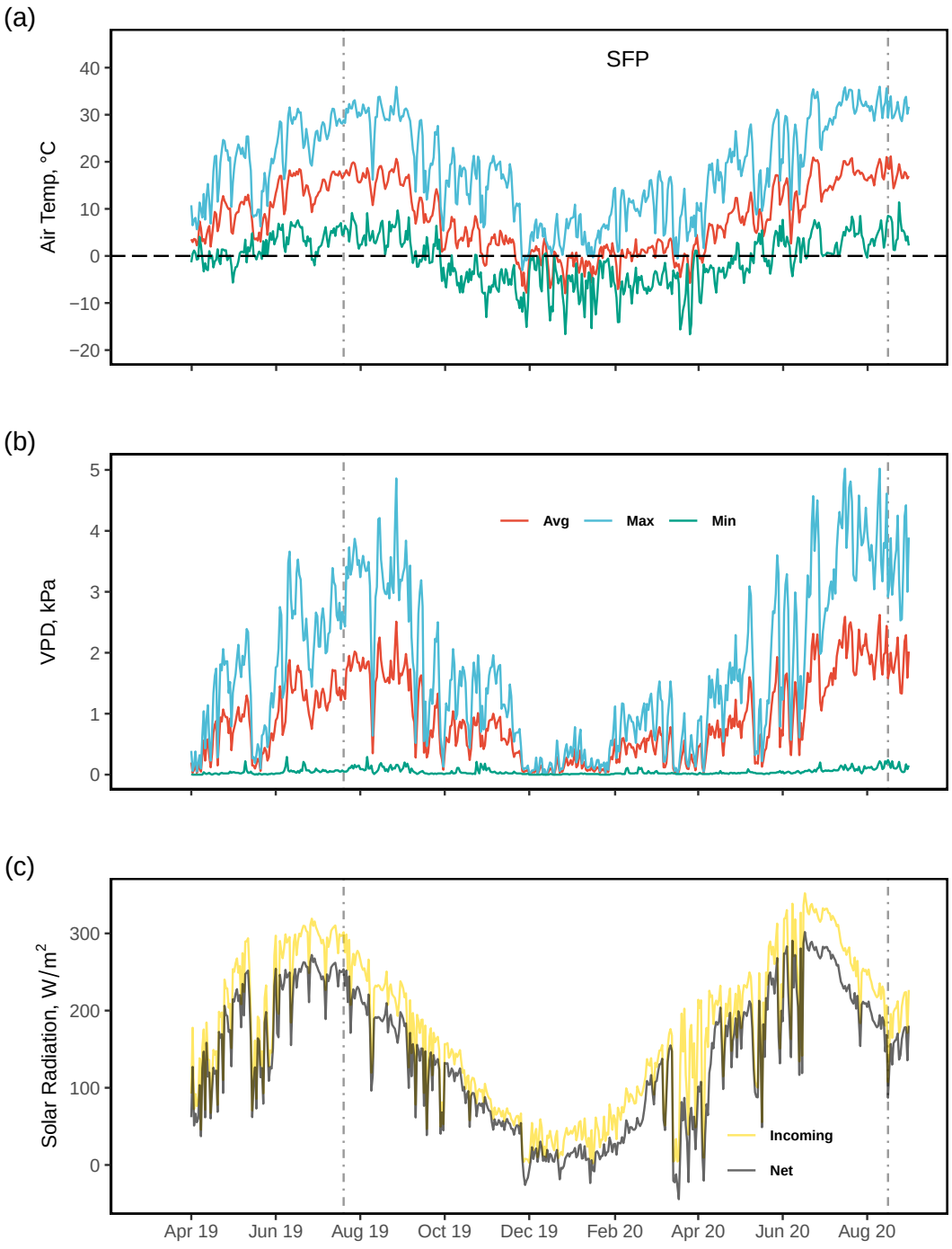

Figure 5.1: Meteorological conditions at RCM for the full 2019 and 2020 growing seasons, encompassing the SFP campaign (dashed vertical lines). From the Control Meadow climate station (Apr. 1, 2019 - Sep. 3, 2019) and RCM climate station (Sep. 4, 2019 - Aug. 31, 2020): (a) daily average, maximum, and minimum air temperature; (b) daily average, maximum, and minimum VPD; and (c) daily average incoming and net solar radiation.

Table 5.1: Climate data for the two years (2019 and 2020) overlapped by the SFP campaign at RCM. Total precipitation (P) is presented for the growing season (GS) period corresponding with each year, along with fall and winter for 2019 and spring and summer for 2020. Averages and standard deviations for other climate variables are provided for the same periods in each year.

	2019		
Measurement	**GS**	**Fall (SON)**	**Winter (DJF)**
Total P (mm)	152	75	243
Avg. Air Temp (°C)	13.5 (9.1)	5.1 (9.2)	-0.6 (5.2)
Avg. VPD (kPa)	0.9 (1.0)	0.5 (0.6)	0.1 (0.2)
Avg. Solar Rad (m W^{-2})	240.7 (397.7)	110.1 (232.2)	53.8 (123.4)
	2020		
Measurement	**GS**	**Spring (MAM)**	**Summer (JJA)**
Total P (mm)	137	188	41
Avg. Air Temp (°C)	12.8 (10.3)	5.2 (8.5)	16.1 (10.1)
Avg. VPD (kPa)	1.0 (1.1)	0.4 (0.6)	1.3 (1.3)
Avg. Solar Rad (m W^{-2})	236.7 (384.1)	170.5 (319.8)	261.2 (403.3)

Most of the precipitation in both years fell as snow, so the majority of reported yearly totals are snow water equivalents. The 2019 WY featured higher precipitation compared to the sum of monthly precipitation normals for Chester during a WY (873 mm), while the 2020 WY featured less. Winter 2019 supplied 243 mm of precipitation to the 2020 WY total (Table 5.1). February 2020 was especially dry providing only a trace amount ($<$ 1 mm) of precipitation, compared to a February precipitation normal value of 135 mm (Figure 5.2a). The majority of the precipitation in the 2020 WY occurred between December 2019 and May 2020, which is characteristic for the region based on the monthly precipitation normals (Figure 5.2a). Solar radiation measurements from the climate station suggest that the snowpack at the SFP melted by April 6 of the 2020 WY. No negative net solar radiation values were recorded after this date (Figure 5.1c and 5.2a). The 2020 growing season provided 137 mm of precipitation, which is slightly less than the sum of monthly normals for the growing season months (140 mm). In contrast, the 2019 growing season featured slightly higher than average precipitation compared to monthly normals (Table 5.1). Relevant to the MJS model validation period is the 2021 WY precipitation (540.6 mm), which was a comparable dry year to the 2020 WY. A total of 34.9 mm of precipitation fell during the 2021 growing season.

Soil moisture conditions monitored in RCM show heterogeneity among measurements taken in different parts of the meadow (Figure 5.2b and 5.2c). Volumetric soil water content (θ_v) monitored at the SFP by RCSM2b ranged between 17% and 36%, with an overall average of 25% (Figure 5.2b and Table 5.2). Temporal trends in SFP soil moisture measurements were similar to measurements for the upper soil profile (0-30 cm depth) in the northeast portion of the meadow by RCSM1 (Figure 5.2b and Table 5.2). Soil moisture was lower on average at these two set-ups compared to RCSM3 and RCSM5, as these latter instruments were situated in close proximity to Rock Creek watercourse. Further, RCSM3 and RCSM5 had θ_v measurements

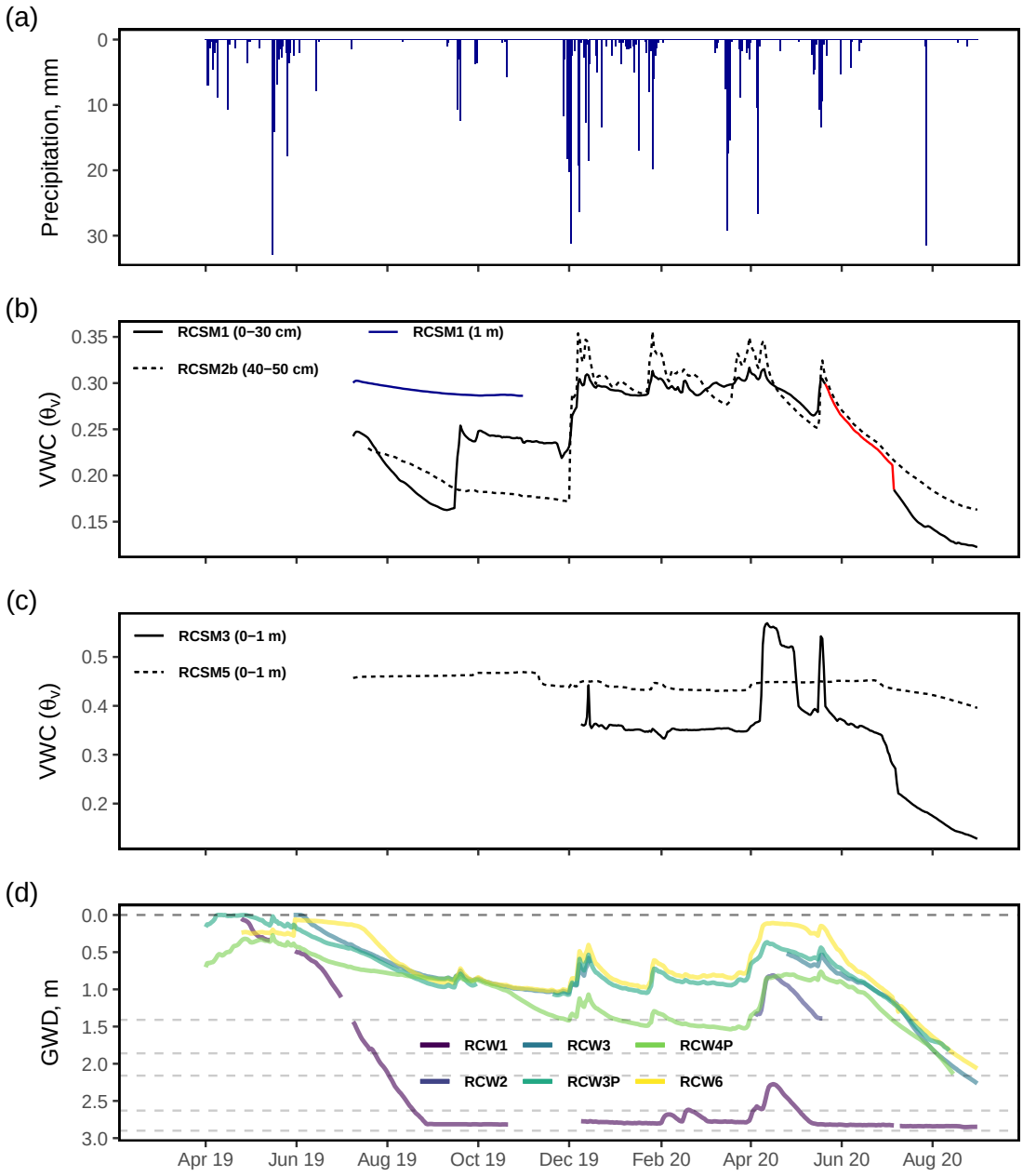

Figure 5.2: Hydrological conditions at RCM for the full 2019 and 2020 growing seasons, encompassing the SFP campaign. (a) Daily total precipitation from the Chester NOAA Station. (b) Average daily volumetric soil water content (θ_v) for RCSM1 and RCSM2b shallow profiles, with a red line denoting infilled data for RCSM1. (c) Average daily θ_v for RCSM3 and RCSM5 1 m profiles. (d) Daily average groundwater depth (GWD) for wells. The lighter dashed lines represent the depth of each well from the surface- data is not displayed once GWD exceeds the well depth and for periods of instrument failure.

taken to a 1 m depth, which captured fluctuations in the groundwater table that are closer to the ground surface in this part of RCM (Figure 5.2c). RCSM5 exhibited the highest θ_v during the SFP campaign compared to all other measurement locations, with 45% average θ_v and limited θ_v fluctuation or decline over the course of the 2020 growing season.

Table 5.2: Average volumetric soil water content (θ_v) for RCM profiles RCSM2b, RCSM1, RCSM2, and RCSM5 for 2 to 5 month periods and the entire SFP campaign. Parenthetical values represent one standard deviation. Periods were selected to showcase variability in θ_v conditions over the SFP campaign.

	Avg. θ_v			
Period (mm/dd/yy)	**RCSM2b**	**RCSM1**	**RCSM3**	**RCSM5**
07/09/19 - 08/31/19	0.22 (0.01)†	0.21 (0.03)	–	0.46 (0.00)
09/01/19 - 11/30/19	0.18 (0.01)	0.23 (0.02)	–	0.46 (0.01)
12/01/19 - 04/30/20	0.31 (0.02)	0.30 (0.01)	0.38 (0.07)†	0.44 (0.01)
05/01/19 - 06/30/20	0.26 (0.02)	0.26 (0.02)	0.38 (0.04)	0.45 (0.00)
07/01/20 - 08/31/20	0.19 (0.02)	0.15 (0.03)	0.18 (0.04)	0.42 (0.01)
Sap flow plot campaign				
07/21/19 - 08/16/20	0.25 (0.06)	0.25 (0.05)	0.35 (0.09)†	0.45 (0.01)

†30-minute θ_v data incomplete for respective period

RCSM2b, RCSM1, and RCSM3 exhibited distinct seasonal fluctuations associated with periods of snowmelt, precipitation events, and growing season soil drying. Growing season θ_v decline in 2020 began in late May for RCSM1 and RCSM2b, while instruments in the wetter part of the meadow showed decline in late June. Figure 5.2b also shows the limited amount of θ_v data collected at RCSM1 for the 1 m depth due to sensor failure. The limited data shows little decline in θ_v in the late 2019 growing season at this depth. Although θ_v data is not present for the entire 2019 growing season due to instrument installation in early July 2019, late growing season

θ_v at RCM was lower in 2020. This likely reflects the difference in total precipitation between the 2019 and 2020 WYs, especially spring and summer rainfall events post snowmelt. For example, average θ_v at RCSM2b for July and August 2020 was 19 $\pm$ 1% compared to 22 $\pm$ 2% for these same months in 2019. This observation of late growing season θ_v is consistent for RCSM1 and RCSM5 (Table 5.2).

Groundwater depth (GWD) measurements indicate the water table was within 1 m of the soil surface for the entire 2019 growing season (0.45 m average GWD) for wells situated in proximity to Rock Creek watercourse (RCW3, RCW3P, RCW4P, and RCW6) (Figure 5.2d). In contrast, the GWD dropped below 1 m in these wells during mid-June 2020 (1.23 m GWD for the 2020 growing season), once again indicating low precipitation and snowmelt in the 2020 WY. The average GWD for these wells during the SFP measurement period reflects the conditions of both growing seasons, with an average depth of 0.97 m.

RCW1 describes the GWD conditions in the eastern portion of the meadow for the 2019 growing season, as RCW2 was installed in the SFP in September 2019. RCW2 is also a shallow well, installed at a 1.41 m depth. During the 2019 growing season, the water table was within 1 m of the ground surface at RCW1 until the end of June (1.47 m average GWD). The GWD was below 2 m at this well for the entirety of the 2020 growing season (2.82 m average GWD) (Figure 5.2d). Average GWD for RCW1 during the SFP measurement period was 2.71 m. Water was present in RCW2 between April 4, 2020 and May 19, 2020 corresponding with the universal maximum rise in the water table measured in all other wells during this year (Figure 5.2d). Water was closest to the ground surface in this well at a depth of 0.81 m on April 15, 2020. Despite the shallowness of RCW2 and similar elevation of RCW2 and RCW1, the data suggests the water table was higher overall during the 2020 growing season at RCW2 compared to RCW1.

5.2 Tree Survey

A total of 1312 trees were surveyed within 14 sample plots in RCM (10 selected with STRS, 4 plots surrounding soil moisture monitoring sites). The majority of surveyed trees were lodgepole pine, 1188 total. The 124 trees surveyed that were not lodgepole pine consisted of 74 white fir (*Abies concolor*), 40 Jeffrey pine (*Pinus jeffreyi*), and 10 aspen (*Populus tremuloides*). All aspen trees were found in the west stratum adjacent to the Rock Creek watercourse.

Table 5.3 provides population and sub-population mean estimates of stem density, basal area, and sapwood basal area calculated from the 10 random plots (5 per stratum). The west stratum featured a higher average lodgepole pine count per hectare compared to the east stratum. Lodgepole pine with a DBH between 2.5 and 10 cm comprised the majority of stem density in both strata; however, a higher number of lodgepole pine greater than 10 cm DBH were found west of the access road. The combination of higher counts of lodgepole pine and trees greater than 10 cm DBH in the west stratum compared to the east results in greater lodgepole pine basal area and sapwood basal area estimates for the western sub-population (Table 5.3).

The lodgepole pine DBH distribution for the random plots separated by strata is shown in Figure 5.3a and 5.3c. Figure 5.3e shows the entire distribution from all random plots. The presented histograms highlight the positive skewness of the lodgepole pine toward smaller DBH size classes for both sub-populations, suggesting that the encroachment of RCM by lodgepole pine is a current and ongoing process. Histograms are also provided displaying the lodgepole pine DBH distribution for the non-random plots to facilitate a comparison with the distributions generated from the random sample plots (Figure 5.3b and 5.3d). For example, the DBH distribution of surveyed lodgepole pine in the non-random, western plots featured a lower proportion of trees between 2.5 and 10 cm DBH (37% of total count) compared to the western

Table 5.3: Sub-population (strata) and population (RCM) estimates of stem density, basal area, and sapwood (SW) basal area derived from the tree survey conducted at RCM via stratified random sampling. Parenthetical values represent one standard error for the parameter estimate. LP = lodgepole pine.

	E. Stratum	**W. Stratum**	**RCM**
Area (ha)	21.125	22.440	43.565
No. Random Plots	5	5	10
Stem Density (ha^{-1})			
LP All DBH	1616.00 (513.25)	1641.60 (427.31)	1629.19 (291.43)
LP DBH >10 cm	275.20 (32.16)	691.20 (201.65)	489.48 (92.58)
LP DBH 2.5 - 10 cm	1340.80 (495.57)	950.40 (293.92)	1139.71 (248.78)
Other tree species	112.00 (60.08)	115.20 (44.22)	113.65 (32.42)
All tree species	1728.00 (493.49)	1756.80 (411.68)	1742.84 (280.46)
Basal Area (m^2 ha^{-1})			
LP	15.73 (1.21)	30.56 (6.27)	23.37 (2.89)
Other tree species	6.61 (3.11)	5.77 (2.38)	6.17 (1.70)
All tree species	22.34 (3.58)	36.33 (6.16)	29.54 (3.18)
SW Basal Area* (m^2 ha^{-1})	10.77 (0.84)	20.90 (4.01)	15.99 (1.86)

*estimated using regression equations for lodgepole pine sapwood and bark depth vs. DBH

stratum random plots (58% of total count). The lodgepole pine DBH distribution in the eastern, non-random plots was less dissimilar to that produced by the eastern stratum random plots. In the non-random plots, 79% of the counted trees were between 2.5 and 10 cm DBH compared to 83% in the random plots.

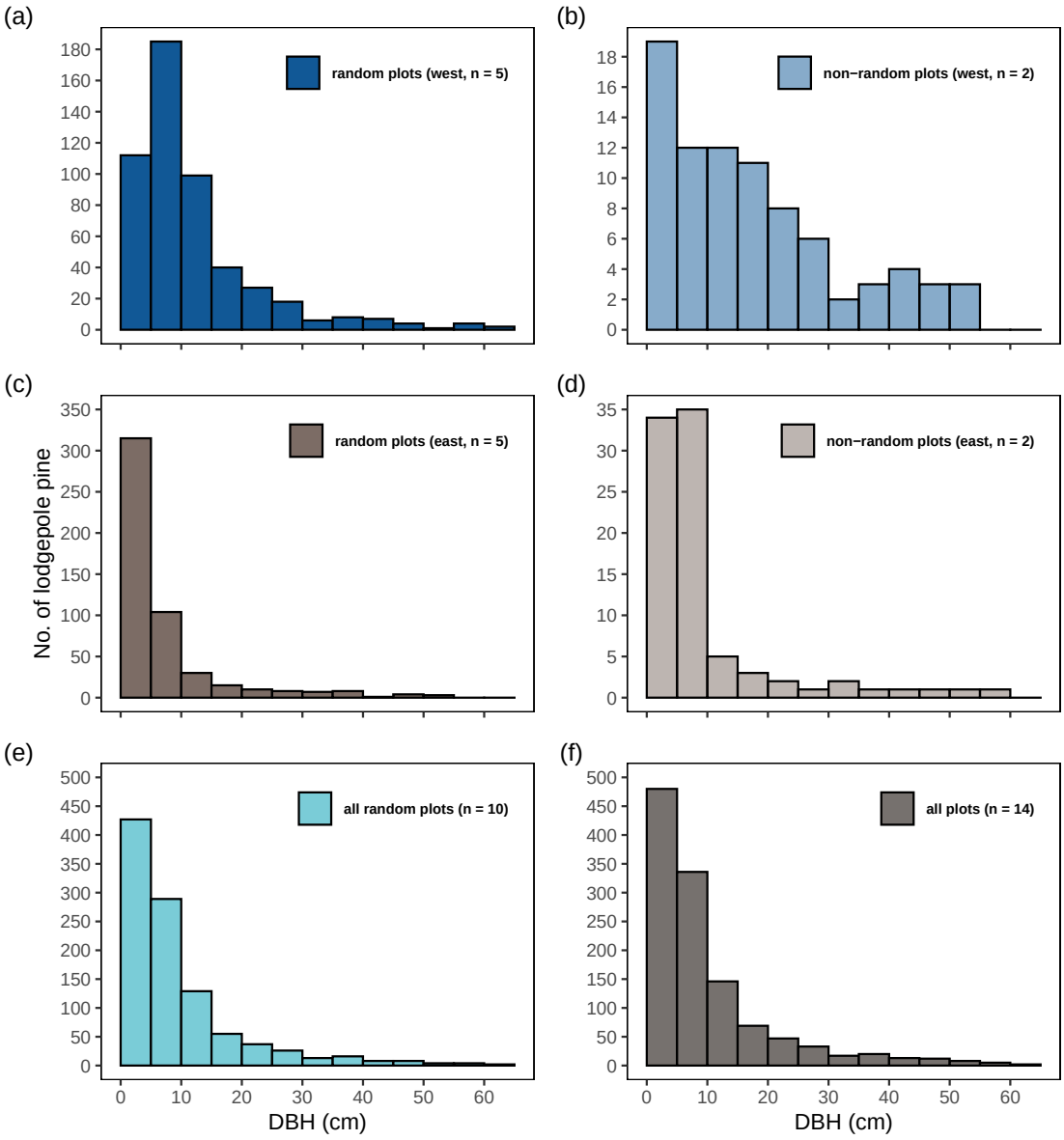

Figure 5.3: Histograms of measured DBH for lodgepole pine measured in 14 sample plots at RCM: (a) in the 5 *random* sample plots in the west stratum; (b) in the 2 *non-random* plots encompassing soil moisture set-ups RCSM3 and RCSM5 in the west stratum; (c) in the 5 *random* sample plots in the east stratum; (d) in the 2 *non-random* plots in the east stratum (SFP and plot encompassing RCSM1); (e) in all 10 *random* sample plots; and (f) in all surveyed plots. Note the differences in vertical scale used for each grouping.

5.3 Sap Velocity Measurements

The lodgepole pine average sap velocity ($\bar{v}_s$) showed seasonal patterns throughout the SFP monitoring period (Figure 5.4). On close inspection and as shown in Figure 5.5, sap velocity followed a diurnal pattern (maximum during the day and minimum at night) with near midday peaks at the beginning of the campaign in late July and early August 2019 coinciding with high daily VPD, solar radiation, and air temperatures. The diurnal pattern remained until late November 2019, with the magnitude of daytime $\bar{v}_s$ measurements and peaks generally diminishing up to this point in agreement with the decreasing magnitude of meteorological variables (Figure 5.4 and 5.5b). For the remainder of the monitored fall, winter, and early spring seasons, the diurnal pattern in $\bar{v}_s$ was absent or less distinct, with measurements hovering around 0 cm h^{-1} during both night and day. The pronounced diurnal pattern in $\bar{v}_s$ returned in early April 2020, with the daytime $\bar{v}_s$ amount increasing into the summer until a peak in late June (Figure 5.4, 5.5c, and 5.5d). The peak $\bar{v}_s$ in late June 2020 was lower compared to the beginning of the monitoring campaign, despite similar meteorological conditions.

Table 5.4 quantifies the general trends, described above, of lodgepole pine average-daytime and nighttime $\bar{v}_s$ on a seasonal basis. Average-daytime $\bar{v}_s$ was highest in the summer of 2019 (11.54 $\pm$ 1.89 cm h^{-1}) compared to all other monitored seasons, with a maximum daytime-average of 15.47 cm h^{-1} on July 24, 2019. The summer 2019 average-daytime $\bar{v}_s$ was greater than that of summer 2020 (6.05 $\pm$ 1.73 cm h^{-1}), which experienced a maximum daytime-average of 9.22 cm h^{-1} on June 23, 2020. From April 1 to August 16, 2020 (2020 partial growing season), the average-daytime $\bar{v}_s$ was 5.11 $\pm$ 2.15 cm h^{-1}. Both summers showed appreciable amounts of nighttime $\bar{v}_s$ compared to the other seasons. Negative/reverse $\bar{v}_s$ was measured most often in the winter months during both night and day, but occurred mostly during nights in

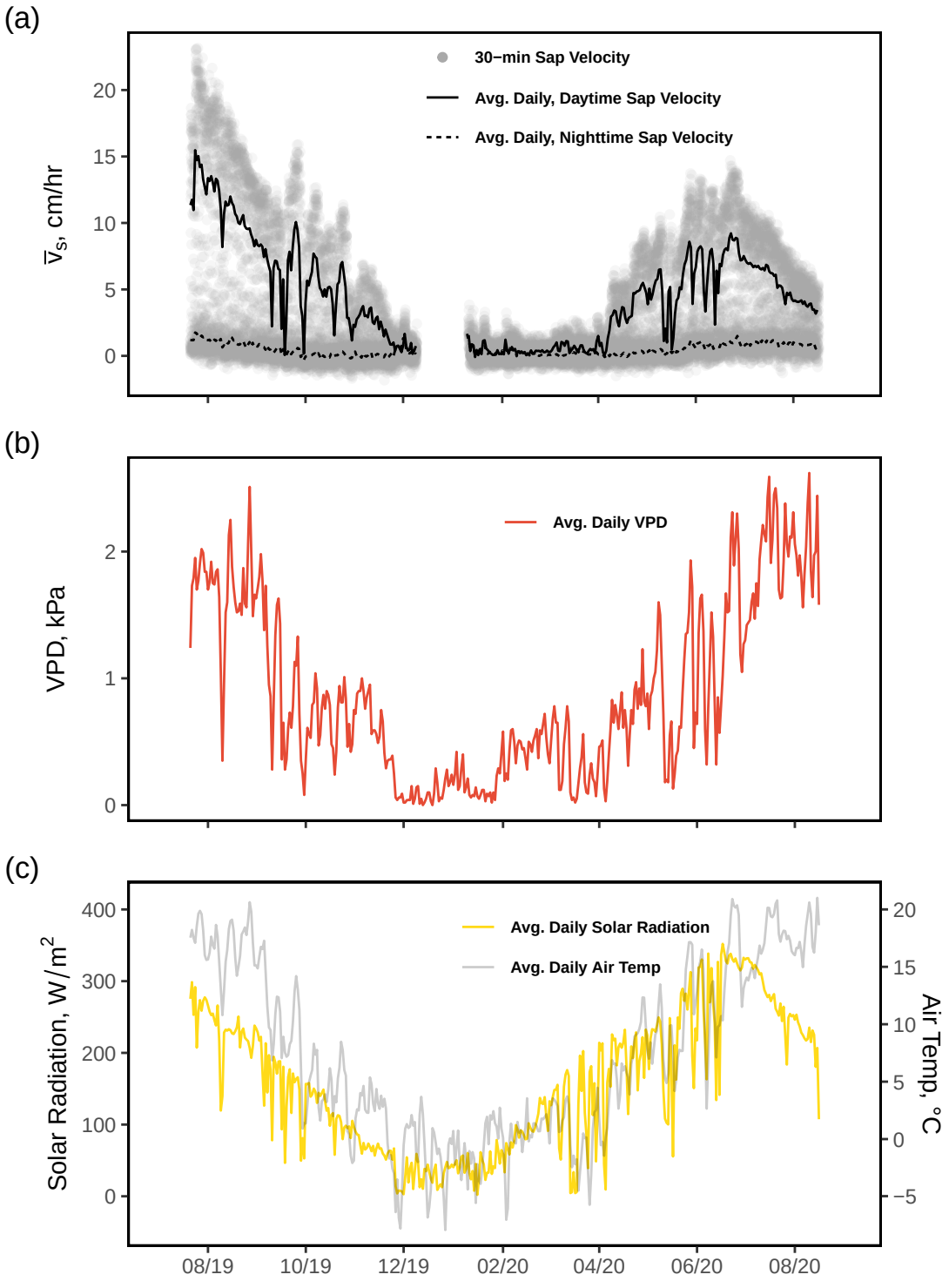

Figure 5.4: (a) 30-minute lodgepole pine average sap velocity ($\bar{v}_s$) and average daily daytime and nighttime $\bar{v}_s$; (b) average daily VPD; and (c) average daily incoming solar radiation and air temperature. (a-c) Display data for the SFP monitoring period of July 21, 2019 through August 16, 2020.

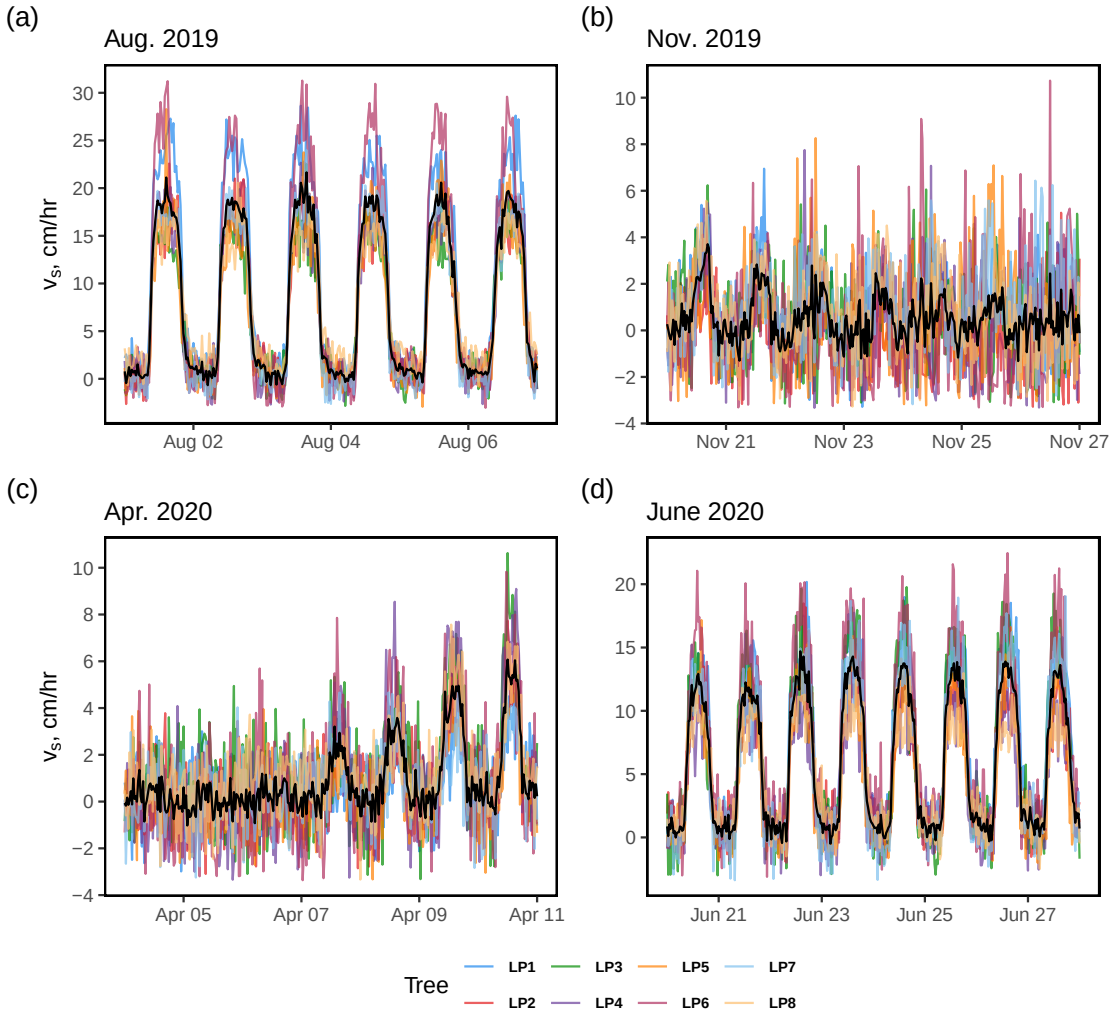

Figure 5.5: Example 30-minute sap velocity (v_s) data from the eight instrumented lodgepole pine collected during the SFP monitoring period. The solid black line represents average sap velocity ($\bar{v}_s$). Note the differences in vertical scale used for each period.

all other seasons throughout the campaign (Figure 5.4a and Table 5.4). Sap velocity measurements collected during winter, however, were the noisiest data relative to measurements from other seasons over the campaign.

Table 5.4: Daytime and nighttime lodgepole pine average sap velocity ($\bar{v}_s$) summary statistics for the SFP measurement campaign separated by season: Summer (JJA), Fall (SON), Winter (DJF), and Spring (MAM).

	Daytime $\bar{v}_s$, cm h^{-1}			
Season	**mean**	**std**	**max**	**min**
Summer 2019†	11.54	1.89	15.47	8.19
Fall 2019	4.44	2.59	10.07	0.07
Winter 2019†	0.43	0.36	1.66	-0.09
Spring 2020	2.80	2.32	8.59	0.08
Summer 2020†	6.05	1.73	9.22	2.35
	Nighttime $\bar{v}_s$, cm h^{-1}			
Season	**mean**	**std**	**max**	**min**
Summer 2019†	1.10	0.28	1.76	0.60
Fall 2019	0.19	0.28	0.89	-0.30
Winter 2019†	0.35	0.34	1.66	-0.03
Spring 2020	0.24	0.23	1.19	-0.16
Summer 2020†	0.92	0.20	1.50	0.46

†30-minute $\bar{v}_s$ data incomplete for season

5.4 MJS Model Calibration

Approximately 16000 simulations of the generalized likelihood (GL) function in DREAM$_{(ZS)}$ were needed to calibrate the MJS model and achieve convergence according to the R-diagnostic of Gelman and Rubin (1992) (Appendix Figure F.1).

This indicates that the 50000 simulations were more than sufficient in exploring the parameter space for the model. The parameter posterior distributions obtained from calibration are shown in Figure 5.6. Every unique combination of parameters from the distributions represents a reasonable MJS model to predict lodgepole pine normalized average sap velocity ($\bar{v}_{s,n}$) in the SFP for the monitored partial growing season. Each model parameter was well identified by DREAM$_{(\mathrm{ZS})}$ within its assumed uniform prior distribution range.

The mean and maximum likelihood parameter estimates (ML) from the posterior distributions are provided in Table 5.5. This includes both parameters from the MJS model and parameters from the GL function error model used for the total uncertainty assessment. The ML parameter estimates are the modes of the posterior distributions shown in Figure 5.6. Also included are the standard deviation and 95% confidence intervals derived from the distributions.

The degree of parameter independence in the prediction of $\bar{v}_{s,n}$ is shown in Table 5.6 with a matrix of correlation coefficients between the MJS model parameters. In our analysis, the parameter pair of g_{bcmax}/α and D_0 co-varied the most out of all other pairs with a correlation coefficient of -0.94. The heavy correlation between g_{bcmax}/α and D_0 is consistent with the work of Oren et al. (1999) and Link et al. (2014). There was also high correlation between T_0 and k_a. These are the two parameters contained in the air temperature stress function from Wang et al. (2020), suggesting over-parameterization of this function. All other parameters in the model were moderately or minimally correlated. Moderate correlation exists between k_a (parameter in the air temperature stress function) and each of D_0 and g_{bcmax}/α (parameters of the VPD stress function). The moderate correlation between these parameters respective of the air temperature and VPD stress functions is likely consequence of the known exponential relationship between VPD and air temperature.

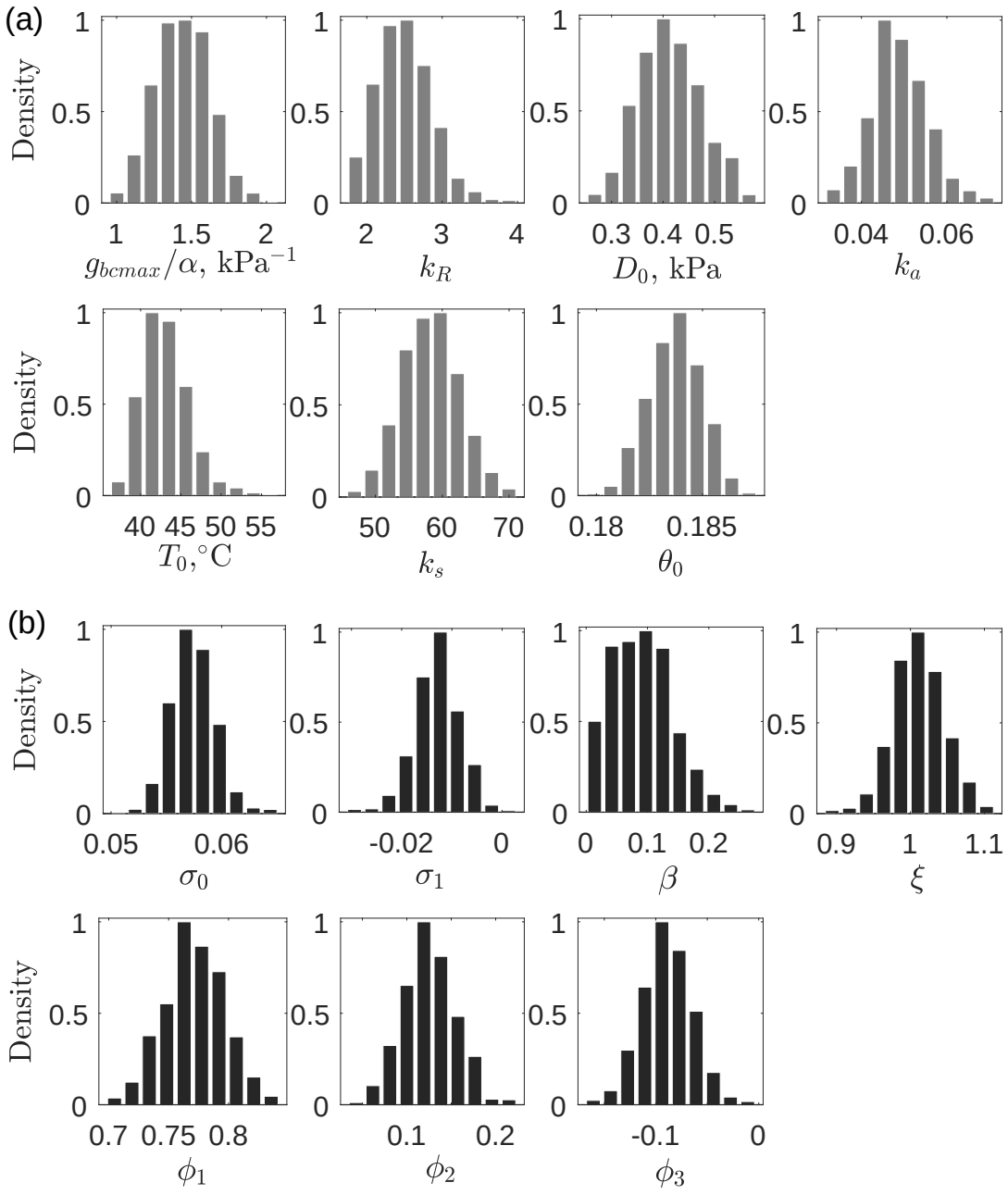

Figure 5.6: Posterior distributions for (a) MJS model parameters and (b) GL function error model parameters.

Table 5.5: Maximum likelihood (ML), mean, standard deviation, lower 95% C.I., and upper 95% C.I. parameter estimates derived from parameter posterior distributions. Parameters are separated into MJS model ($\text{PARM}_{(\theta)}$) and GL function error model ($\text{PARM}_{(\varphi)}$) parameters.

	MJS Model				
$\text{PARM}_{(\theta)}$	ML	mean	std	Lower 95% C.I.	Upper 95% C.I.
g_{bcmax}/α (kPa^{-1})	2.675	2.501	0.365	1.877	3.294
k_R	1.441	1.439	0.180	1.093	1.793
D_0 (kPa)	0.372	0.413	0.061	0.301	0.536
k_a	0.053	0.049	0.007	0.036	0.063
T_0 (°C)	41.880	43.102	2.897	38.370	49.894
k_s	57.914	58.241	4.315	50.009	67.144
θ_0	0.184	0.184	0.001	0.181	0.186
	GL Error Model				
$\text{PARM}_{(\varphi)}$	ML	mean	std	Lower 95% C.I.	Upper 95% C.I.
σ_0	0.056	0.057	0.002	0.054	0.062
σ_1	-0.009	-0.013	0.005	-0.022	-0.005
β	0.068	0.091	0.050	0.008	0.200
ξ	1.022	1.011	0.035	0.941	1.081
ϕ_1	0.774	0.771	0.025	0.723	0.820
ϕ_2	0.120	0.125	0.029	0.067	0.180
ϕ_3	-0.085	-0.089	0.025	-0.138	-0.042

Table 5.6: Matrix of correlation coefficients (co-variation) for MJS model parameters ($\text{PARM}_{(\theta)}$).

	DREAM$_{(ZS)}$ Posterior Correlation Coefficients						
PARM$_{(\theta)}$	g_{bcmax}/α	k_R	D_0	k_a	T_0	k_s	θ_0
g_{bcmax}/α	1.00	-0.16	**-0.94**	0.47	0.09	-0.06	0.09
k_R	-0.16	1.00	0.08	-0.07	-0.17	0.20	-0.03
D_0	**-0.94**	0.08	1.00	-0.64	0.17	-0.01	-0.01
k_a	0.47	-0.07	-0.64	1.00	**-0.78**	0.00	0.06
T_0	0.09	-0.17	0.17	**-0.78**	1.00	-0.06	0.06
k_s	-0.06	0.20	-0.01	0.00	-0.06	1.00	0.09
θ_0	0.09	-0.03	-0.01	0.06	0.06	0.09	1.00

The ML parameter estimates provided well-defined functional dependencies to describe the relationships between $\bar{v}_{s,n}$ and environmental drivers. Figure 5.7 shows the non-limited functional dependencies (solid lines) that represent the prediction of $\bar{v}_{s,n}$ for a given stress function when all other stress functions are fixed at a value of 1 (indicating that $\bar{v}_{s,n}$ is non-limited by all other functions). Included in Figure 5.7a-d are additional functional dependencies (dotted and dashed lines) representing how the non-limited curves for each stress function are adjusted with change in other environmental drivers contained in the MJS model. For example, Figure 5.7c shows how the prediction of $\bar{v}_{s,n}$ from the air temperature function responds to different cases of θ_v. The air temperature function would be adjusted further depending on values of incoming solar radiation and VPD, but these effects were excluded from the plot for simplicity.

The identified MJS model ML parameter estimates and resulting functional dependencies suggest varying degrees of sensitivity of lodgepole pine $\bar{v}_{s,n}$ to environmental drivers during the 2020 partial growing season. Lodgepole pine's $\bar{v}_{s,n}$ response to

incoming solar radiation is captured by the shape parameter k_R, which describes the curvature of the assumed asymptotic relationship between $\bar{v}_{s,n}$ and solar radiation. The ML estimate of k_R is very low within it's assumed uniform prior distribution range. Accordingly, the solar radiation functional dependency (f_R) shows that saturation toward $\bar{v}_{s,n} = 1$ occurred at approximately 100 W m^{-2} (Figure 5.7a). In other words, $\bar{v}_{s,n}$ rapidly increases over low values of solar radiation and fails to increase further at high values of solar radiation.

The functional relationships between $\bar{v}_{s,n}$ and each of VPD, air temperature, and θ_v are tightly coupled to the observed data (Figure 5.7b-c). Average sap velocity gradually increased with increasing VPD, with an evident plateauing effect at high VPD values (Figure 5.7b). This relationship is controlled by the parameters D_0 and g_{bcmax}/α. It appears, however, that the plateauing effect at high VPD values is over-exaggerated when other environmental drivers are conducive to non-stressed/limited $\bar{v}_{s,n}$ (e.g., $\theta_v > 0.35$, Figure 5.7b). The non-limited VPD functional dependency (f_D) does not reach $\bar{v}_{s,n} = 1$ over a realistic domain of VPD values (Figure 5.7b). The sigmoidal air temperature functional dependency (f_{T_a}) shows the greatest rate of $\bar{v}_{s,n}$ increase between approximately 0 and 25 °C, with leveling toward maximum $\bar{v}_{s,n}$ after approximately 30 °C. The upper threshold of 41.88 °C is represented by the T_0 parameter, after which $\bar{v}_{s,n}$ is assumed to decrease due to temperature stress. Lastly, the fitted sigmoidal θ_v functional dependency (f_{θ_v}) results in a decline of $\bar{v}_{s,n}$ due to soil moisture centered around the θ_0 parameter of 0.184. The θ_v function dictates little $\bar{v}_{s,n}$ limitation when θ_v is greater than 0.25 (Figure 5.7d). The parameter k_s controls the rate of decline in f_{θ_v} with decreasing θ_v values that are perceived as limiting to $\bar{v}_{s,n}$.

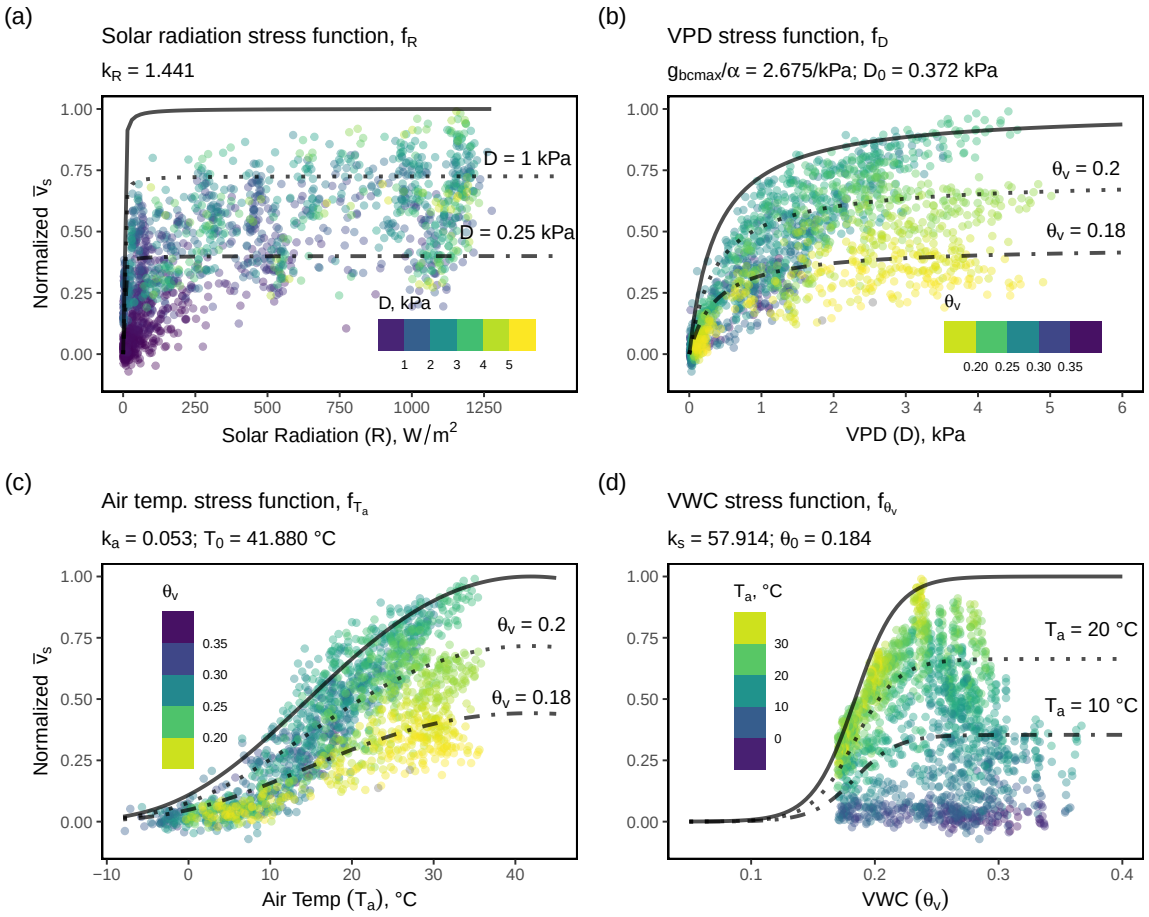

Figure 5.7: Hourly normalized average sap velocity ($\bar{v}_{s,n}$) response to environmental drivers for the *calibration* period. The functional dependencies under non-limiting conditions prescribed by the MJS model ML parameter estimates for each driver are shown by the solid lines, while examples of limiting conditions are indicated by dotted and dashed lines: (a) $\bar{v}_{s,n}$ vs. solar radiation with different cases of VPD; (b) $\bar{v}_{s,n}$ vs. VPD with different cases of θ_v; (c) $\bar{v}_{s,n}$ vs. air temperature with different cases of θ_v; and (d) $\bar{v}_{s,n}$ vs. θ_v with different cases of air temperature.

5.5 MJS Model Performance and Validation

The performance of the MJS model ML parameter estimates for the calibration and validation periods is shown in Table 5.7. As expected, the variation in the observed data was better explained by the model during the calibration period compared to the validation period. The RMSE of 0.087 for calibration equates to an average sap velocity of 1.25 cm h^{-1} after removing the normalization constant ($\bar{v}_{s,max}$ = 14.33 cm hr^{-1}). The ML parameter estimates had an average tendency to under-predict $\bar{v}_{s,n}$, with negative PBIAS for both periods. Negative PBIAS was worse/more extreme for the calibration period compared to validation, which was a counterintuitive result. We discuss this further in Section 6.3.

Table 5.7: Model efficiency criteria for the calibration and validation periods.

Period	RMSE	PBIAS (%)
Calibration	0.0874	-6.579
Validation	0.1233	-2.873

A further evaluation of fit quality for the calibration and validation periods is provided by Figure 5.8. We observed a strong linear relationship between observed and predicted values for the calibration period, with a slope of linear regression close to 1 (Figure 5.8a). The linear fit for the validation is also strong (slope = 0.9), but features greater scatter around the SLR line, corresponding with the larger RMSE computed for this period relative to calibration (Figure 5.8b). The linear regressions coupled with 1:1 lines illuminate the negative PBIAS for both periods. The SLR regression line intersects and dips below the 1:1 line at an approximate observed $\bar{v}_{s,n}$ value of 0.18 for the calibration period and 0.33 for validation, highlighting the tendency of the MJS model to under-predict high $\bar{v}_{s,n}$ values.

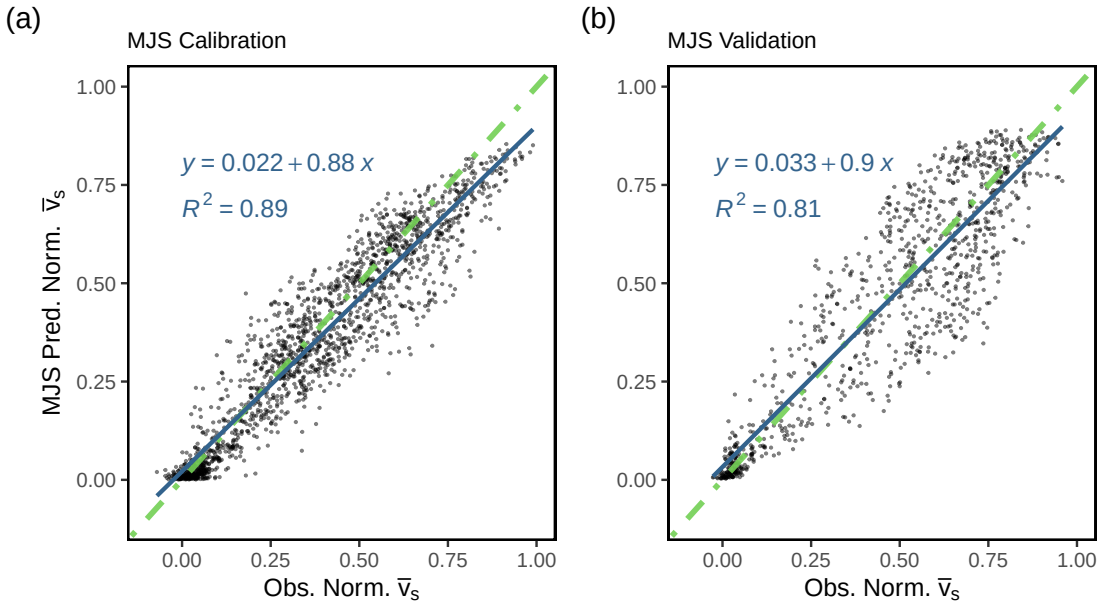

Figure 5.8: MJS predicted vs. observed normalized average sap velocity ($\bar{v}_{s,n}$) for the (a) calibration and (b) validation periods including 1:1 line (dashed-green), SLR regression line (blue), regression equation, and R^2 value.

Figure 5.9 provides a qualitative point of comparison for the $\bar{v}_{s,n}$ environmental driver response between the calibration and validation periods. Notably, the functional dependencies informed by the ML parameter estimates (from calibration) for incoming solar radiation, VPD, and air temperature were similarly coupled to observations of $\bar{v}_{s,n}$ for the validation period (Figure 5.9a-c). The similar RMSE and closeness to the 1:1 line for calibration and validation provides quantitative evidence that $\bar{v}_{s,n}$ responded similarly to climatic environmental drivers between the 2020 and 2021 growing seasons (Figure 5.8). Figure 5.9d reveals that we were unable to evaluate the validation performance under the full range of soil moisture conditions perceived as limiting by the calibration period. We only recorded θ_v values at the validation site between approximately 23% and 30%, due to the Dixie Fire destroying the sap flow set-up in early August 2021.

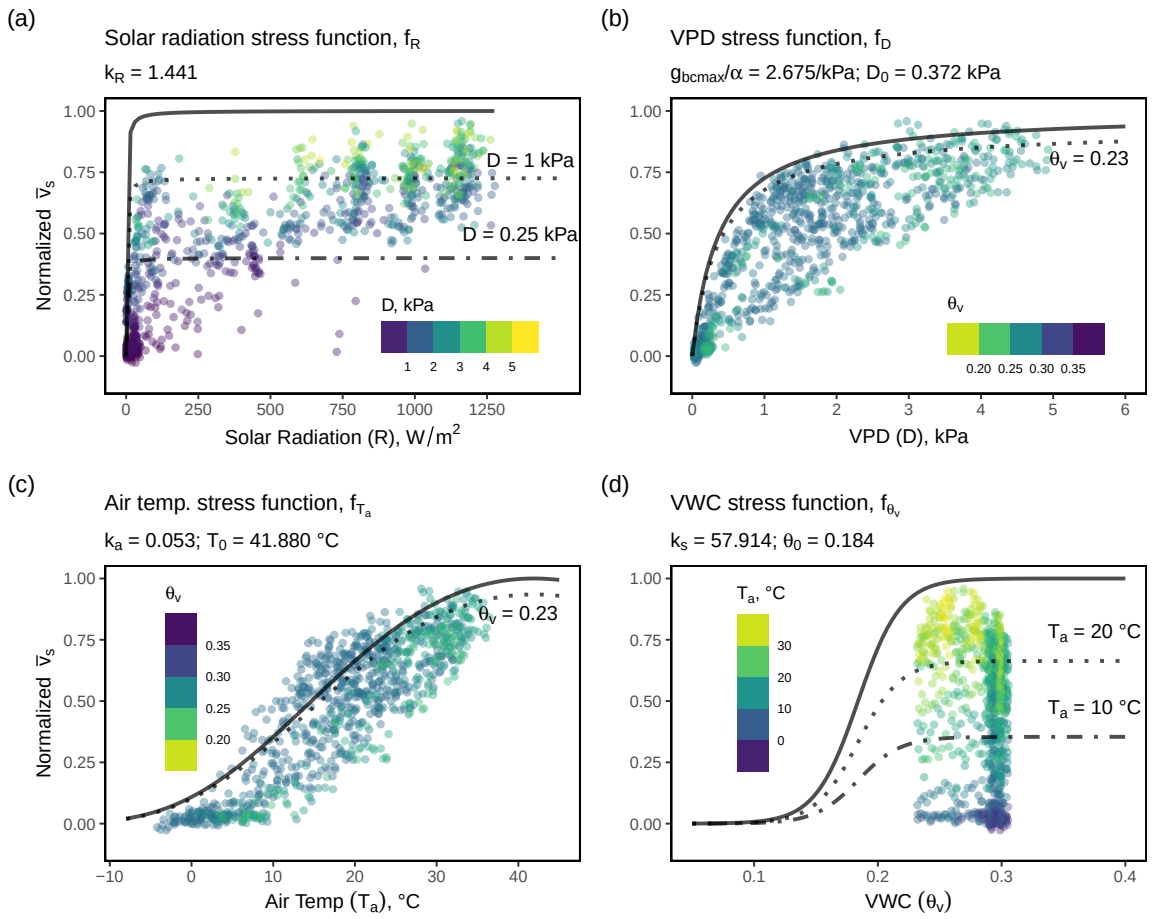

Figure 5.9: Hourly normalized average sap velocity ($\bar{v}_{s,n}$) response to environmental drivers for the *validation* period. The functional dependencies under non-limiting conditions prescribed by the MJS model ML estimates for each driver are shown by the solid lines, while examples of limiting conditions are indicated by dotted and dashed lines: (a) $\bar{v}_{s,n}$ vs. solar radiation with different cases of VPD; (b) $\bar{v}_{s,n}$ vs. VPD with a different case of θ_v; (c) $\bar{v}_{s,n}$ vs. air temperature with a different case of θ_v; and (d) $\bar{v}_{s,n}$ vs. θ_v with different cases of air temperature.

The parameter uncertainty associated with model predictions for the calibration and validation periods is presented in Figure 5.10. The 95% confidence parameter uncertainty band was determined using the last 7502 MJS model parameter sets identified by DREAM$_{(ZS)}$. Expanding on Figure 5.8, our parameter uncertainty interval communicates the timing of the model's tendency to under-predict $\bar{v}_{s,n}$. Under-prediction was most common around midday peaks, as this time of day corresponds with observations of high sap flow. The inset graphs in Figure 5.10 emphasize that the parameter uncertainty bands, let alone the ML parameter estimates, frequently fail to envelop midday $\bar{v}_{s,n}$ observations.

Figure 5.11 shows a 95% total predictive uncertainty confidence interval for the calibration and validation periods. Similar to the parameter uncertainty, the total predictive uncertainty was determined with the last 7502 DREAM$_{(ZS)}$ model simulations, but using the GL function error model parameter posterior distributions and the algorithm of Schoups and Vrugt (2010). Our predictive uncertainty bands envelop very close to the theoretically expected 95% of total $\bar{v}_{s,n}$ observations for the calibration period. The interval envelops a comparable 81.8% of total observations from the validation period. Contrasting the parameter uncertainty interval displayed in Figure 5.9 with Figure 5.11, reveals that the parameter uncertainty is minimal relative to the total predictive uncertainty for both calibration and validation. Accordingly, almost all of the midday $\bar{v}_{s,n}$ observations are captured in the total uncertainty band for both periods.

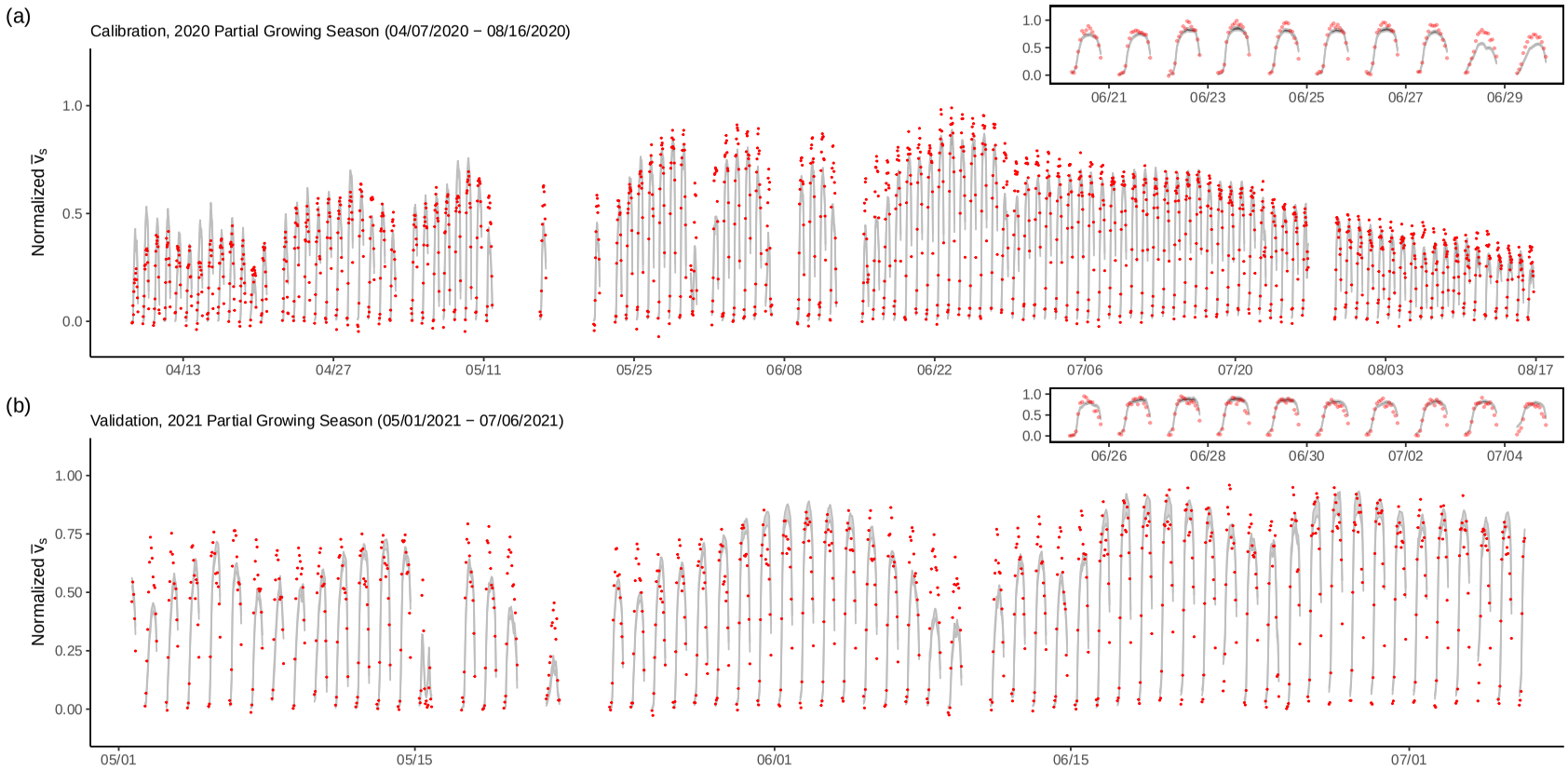

Figure 5.10: 95% *parameter* uncertainty confidence interval and normalized average sap velocity ($\bar{v}_{s,n}$) observations (red points) for (a) calibration and (b) validation periods. Gaps in the time series represent observation data that was removed from the analysis due to precipitation or it being nighttime. Insets show close-up of 10 days of $\bar{v}_{s,n}$ observations and corresponding 95% confidence parameter uncertainty interval for each period.

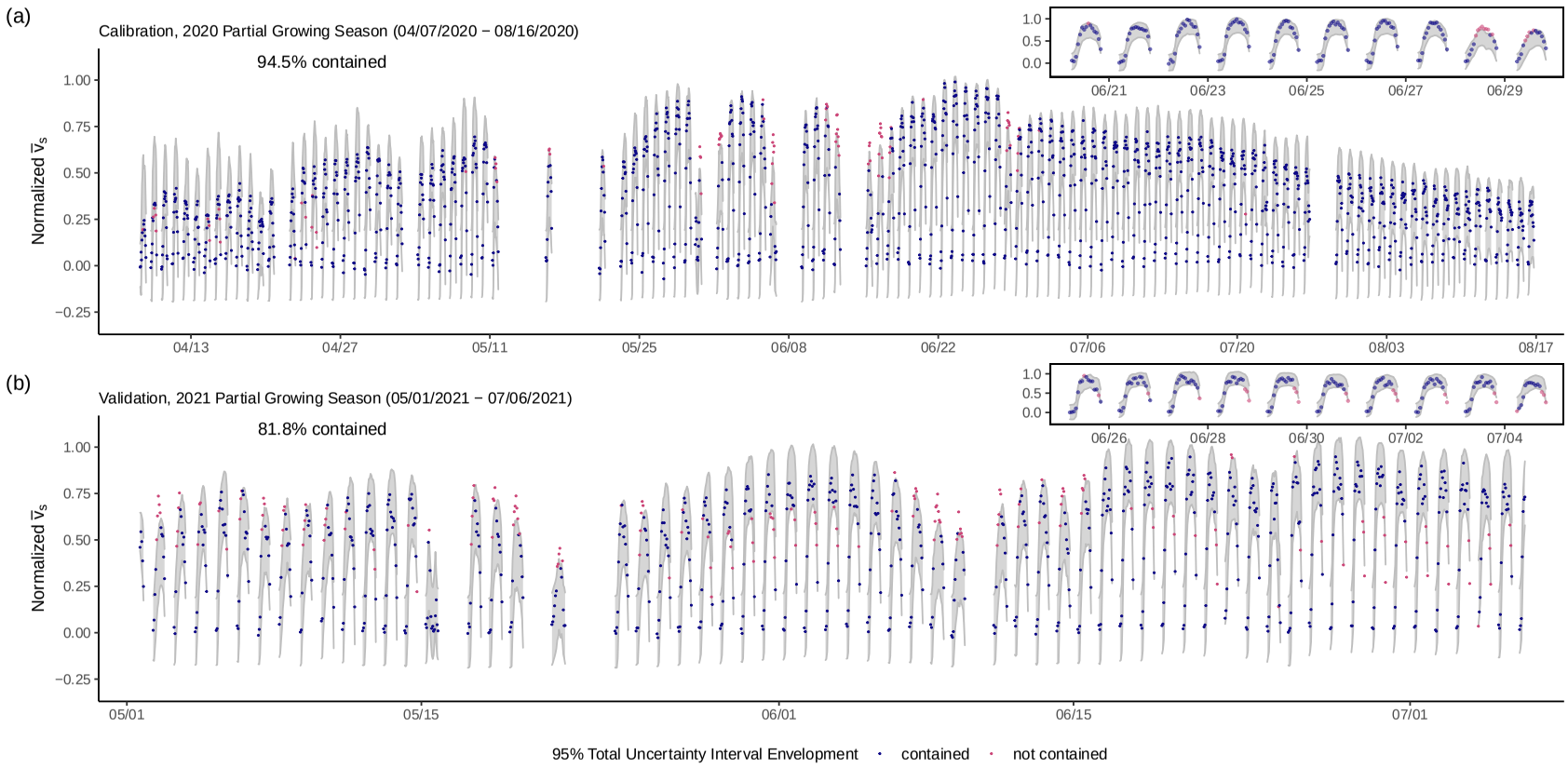

Figure 5.11: 95% *total* predictive uncertainty confidence interval and normalized average sap velocity ($\bar{v}_{s,n}$) observations (blue and red points) for (a) calibration and (b) validation periods. Gaps in the time series represent observation data that was removed from the analysis due to precipitation or it being nighttime. Insets show close-up of 10 days of $\bar{v}_{s,n}$ observations and corresponding 95% confidence total uncertainty interval for each period.

5.6 Volumetric Sap Flow and Transpiration Estimates

5.6.1 Sap flow plot estimates

The sap velocity (v_s) measurements from the eight lodgepole pine in the SFP were used to estimate volumetric sap flow (Q) for each instrumented tree. Figure 5.12 displays daily Q estimates from four of the instrumented trees, produced by the $f_{p,1}(r)$ and $f_{p,3}(r)$ sap velocity radial profiles. The four trees shown in Figure 5.12 were chosen because they showcase the variability of Q among the trees due to tree size and within tree Q variability due to the assumed radial profile. The $f_{p,1}(r)$ and $f_{p,3}(r)$ radial profiles provide an upper and lower Q estimate respectively.

Given the scaling approach implemented, the estimated daily Q for each instrumented tree was a function of measured v_s and sapwood depth (D_s). Estimates ranged between a maximum total Q given by LP1 and minimum Q given by LP5 (Figure 5.12a and 5.12c). The daily Q estimates produced by the largest (LP1) and smallest (LP5) trees in terms of D_s differed by approximately one order of magnitude over the course of the campaign. Additionally, there is little difference in the Q estimates produced by the two shown profiles for LP5 because the sap flow probe sampled most of the sapwood depth for this small tree. The time series for LP4 and LP6 represent intermediate daily Q values produced by trees with D_s between that of LP1 and LP5 (Figure 5.12b and 5.12d). Although similar to LP1 in terms of D_s, LP4 produced slightly over half of the total Q of LP1 for the monitoring campaign (8.42 x 10^6 cm^3 versus 1.21 x 10^7 cm^3 given by $f_{p,3}(r)$) (Figure 5.12b). The discrepancy is largely due to differences in measured v_s between these trees. Figure E.2 provides daily Q for the other four instrumented lodgepole pine, further highlighting the between tree Q variability.

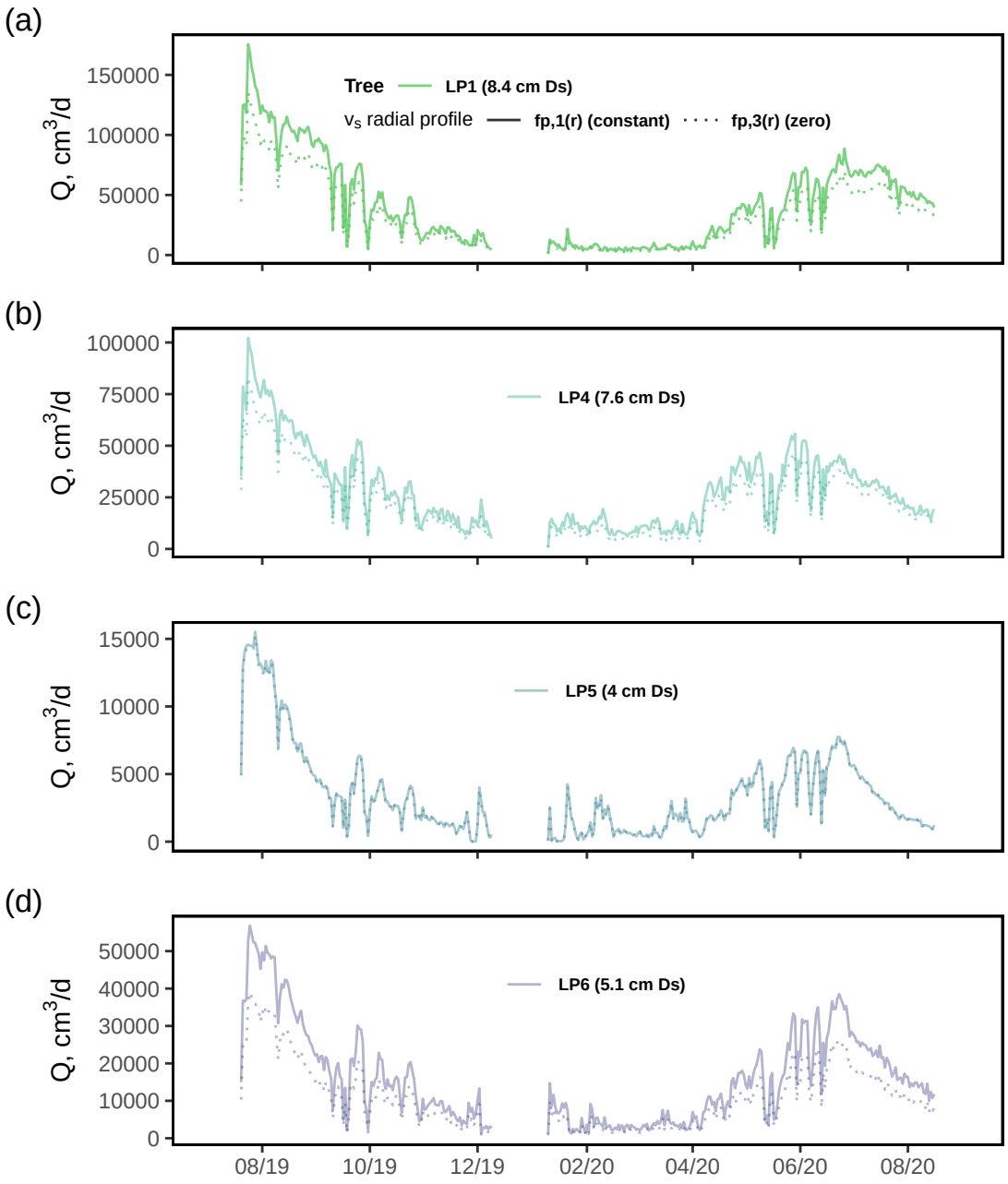

Figure 5.12: Daily volumetric sap flow (Q) estimates for LP1, LP4, LP5, and LP6 given by the $f_{p,1}$ and $f_{p,3}$ sap velocity radial profiles over the SFP monitoring period. Note the differences in vertical scale used for the 4 trees.

The daily transpiration estimates for the SFP over the monitoring period are presented in Figure 5.13. The daily transpiration quantity represents the sum of the Q estimated for the eight instrumented lodgepole pine and Q estimated for non-instrumented lodgepole pine converted to depth. Daily transpiration ranged from a maximum of 1.27 mm/d - 1.73 mm/d in late July 2019 to a minimum of 0.001 - 0.01 mm/d in early January 2020, with the bounds for these estimates given by $f_{p,3}(r)$ and $f_{p,1}(r)$ respectively. The peak daily transpiration for the 2020 partial growing season was estimated between 0.68 and 0.93 mm/d and occurred in late June. Total transpiration for the monitoring period was computed between 116.62 mm and 160.19 mm. Table 5.8 further summarizes the transpiration estimates for the SFP by season and radial profile.

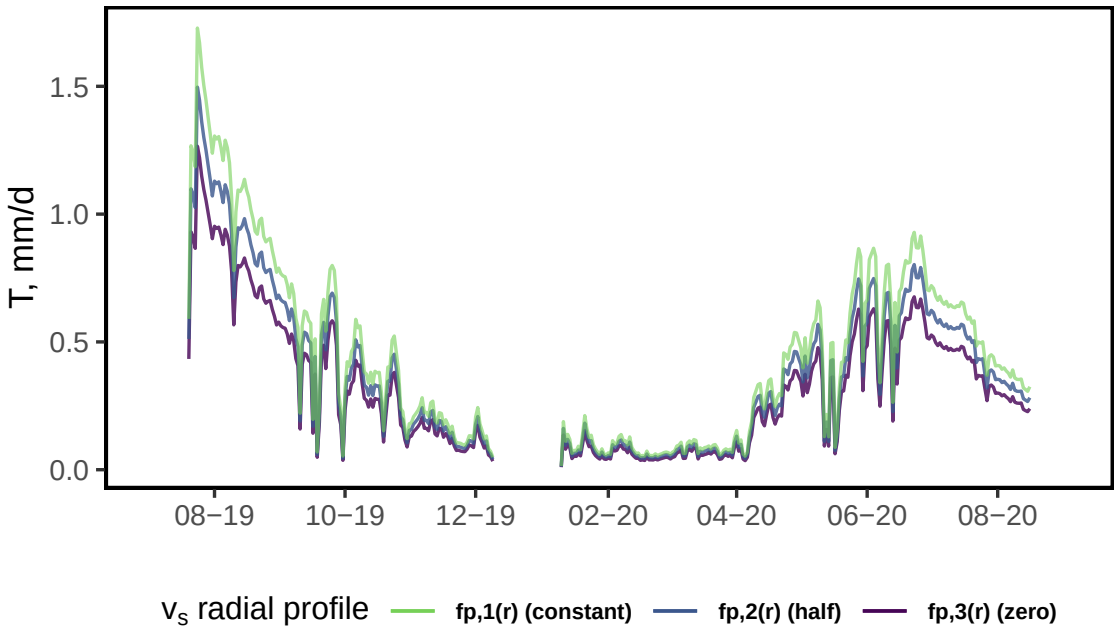

Figure 5.13: Daily transpiration (T) estimates for the SFP over the monitoring period by sap velocity radial profile.

Table 5.8: Seasonal *SFP* transpiration (T) total and mean daily transpiration estimates by sap velocity radial profile. Parenthetical values represent one standard deviation of the mean. GS = growing season.

	Total T, mm			Avg. Daily T, mm/d		
Season	$f_{p,1}(r)$	$f_{p,2}(r)$	$f_{p,3}(r)$	$f_{p,1}(r)$	$f_{p,2}(r)$	$f_{p,3}(r)$
Summer 2019†	47.77	41.32	34.87	1.14 (0.24)	0.98 (0.21)	0.83 (0.17)
Fall 2019	33.51	28.95	24.41	0.37 (0.21)	0.32 (0.18)	0.27 (0.16)
Winter 2019†	5.77	4.91	4.07	0.10 (0.05)	0.08 (0.04)	0.07 (0.01)
Spring 2020	26.82	23.09	19.38	0.29 (0.22)	0.25 (0.19)	0.21 (0.16)
Summer 2020†	45.73	39.59	33.46	0.59 (0.18)	0.51 (0.16)	0.43 (0.13)
Partial GS 2020†	69.89	60.41	50.95	0.51 (0.21)	0.44 (0.19)	0.37 (0.16)

†T estimate incomplete for season

5.6.2 RCM estimates

The methodology to estimate lodgepole pine transpiration in the SFP was extended to the 10 random plots of the same dimension located in the eastern and western strata at RCM. The time series of daily average transpiration by strata and v_s radial profile are pictured in Figure 5.14. The difference in estimated daily transpiration between the west and east strata is explained by the lodgepole pine stem counts and estimated sapwood depths, used in the simple scaling approach. Table 5.9 summarizes the seasonal transpiration totals determined by strata.

The estimates presented in Table 5.9 allow comparison of transpiration between the two demarcated regions in RCM, as well as a comparison of transpiration estimated for eastern stratum plots with that estimated for the SFP. A larger amount of total transpiration was estimated on a per plot basis in the western stratum compared to the east, due to the higher lodgepole pine density and higher counts of trees

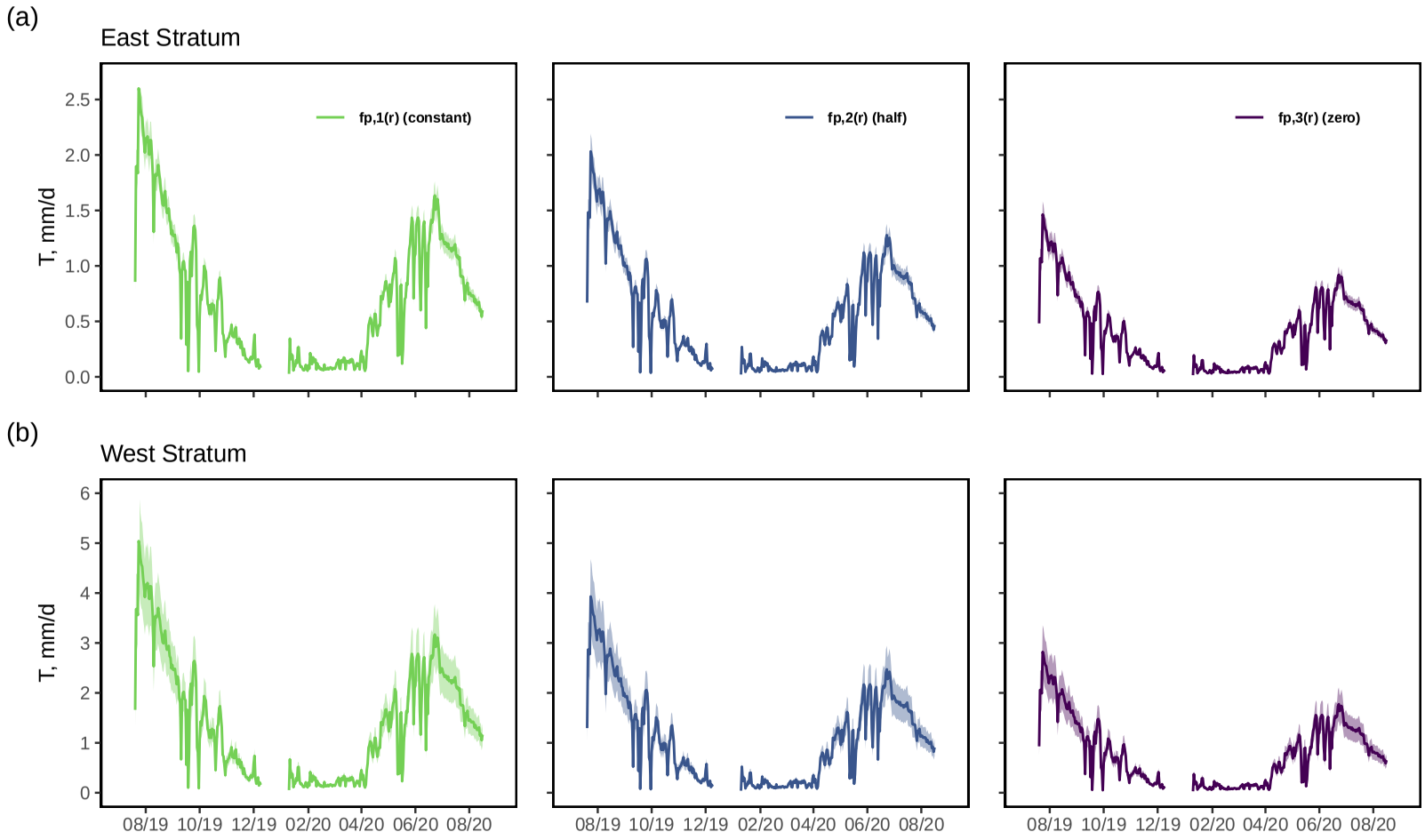

Figure 5.14: Daily average transpiration (T) estimated for the random plots in the east and west strata by sap velocity radial profile. The ribbons around lines represent ± 1 standard error of the daily mean. Note the differences in vertical scale used for each stratum.

Table 5.9: Seasonal *stratum* mean transpiration (T) total estimates by sap velocity radial profile. Italicized values represent one standard error of the mean. GS = growing season.

Season	Total T, mm (***East***)			Total T, mm (***West***)		
	$f_{p,1}(r)$	$f_{p,2}(r)$	$f_{p,3}(r)$	$f_{p,1}(r)$	$f_{p,2}(r)$	$f_{p,3}(r)$
Summer 2019†	78.05	60.99	43.93	151.28	117.98	84.67
	6.10	*4.82*	*3.54*	*29.03*	*22.54*	*16.05*
Fall 2019	55.83	43.62	31.42	108.22	84.39	60.57
	4.37	*3.45*	*2.53*	*20.76*	*16.12*	*11.48*
Winter 2019†	7.09	5.54	3.99	13.74	10.72	7.69
	0.55	*0.44*	*0.32*	*2.64*	*2.05*	*1.46*
Spring 2020	42.79	33.43	24.08	82.94	64.68	46.42
	3.35	*2.64*	*1.94*	*15.91*	*12.35*	*8.80*
Summer 2020†	81.45	63.65	45.84	157.89	123.13	88.37
	6.37	*5.03*	*3.69*	*30.30*	*23.52*	*16.75*
Partial GS 2020†	120.50	94.16	67.82	233.58	182.15	130.73
	9.43	*7.44*	*5.46*	*44.82*	*34.79*	*24.78*

†T estimate incomplete for season

with large DBH (Table 5.3; Figure 5.3). Average total transpiration for random plots in the eastern strata was estimated between 149.74 ± 12.06 mm and 266.05 ± 20.81 mm, given by $f_{p,3}(r)$ and $f_{p,1}(r)$ respectively for the monitoring period. Average total transpiration for the random plots in the western stratum close to doubled that for the east, with estimates between 288.64 ± 54.71 mm and 515.72 ± 98.96 mm. The transpiration total estimated for the SFP alone (116.62 - 160.19 mm), was noticeably less than the average per plot estimate for the eastern stratum. Both the upper and lower total transpiration estimate for the SFP given by $f_{p,1}(r)$ and $f_{p,3}(r)$ were outside the range of values encapsulated by one standard error of these respective estimates for the eastern stratum.

We used our average per plot transpiration estimates for the two strata to estimate transpiration for RCM as a whole. This statistic was calculated in the framework of the STRS design employed in this study. Average total transpiration for RCM was estimated between 220.57 ± 25.28 mm and 393.39 ± 45.65 mm, given by $f_{p,3}(r)$ and $f_{p,1}(r)$ respectively for the entire monitoring period. Table 5.10 summarizes total transpiration for the meadow by season.

Lastly, we compared our lodgepole pine transpiration estimates based on average sap velocity ($\bar{v}_s$) measurements and the tree survey to MODIS derived evapotranspiration (ET) (MOD16A2GF product). Figure 5.15 facilitates a comparison of seasonal timing between lodgepole pine transpiration and MODIS ET estimates. The timing of peak MODIS ET and sap flow based transpiration was similar in the 2019 growing season. MODIS ET peaked during the 8-day period of July 12 through 19. The highest 8-day transpiration from the 2019 growing season was July 28 through August 4; however, this sum was very similar to the preceding composite given for July 20 through 27 that summed one less day due to the SFP campaign beginning on July 21, 2019. Transpiration for the 2019 growing season decline began in early August, matching the general trend of the MODIS estimates. The timing of peak MODIS ET

Table 5.10: Seasonal *RCM* transpiration (T) estimates by sap velocity radial profile. Parenthetical values represent one standard error of the mean. GS = growing season.

	Total T, mm		
Season	$f_{p,1}(r)$	$f_{p,2}(r)$	$f_{p,3}(r)$
Summer 2019†	115.77 (13.43)	90.34 (10.43)	64.91 (7.44)
Fall 2019	82.81 (9.61)	64.62 (7.46)	46.43 (5.32)
Winter 2019†	10.51 (1.22)	8.21 (0.95)	5.90 (0.68)
Spring 2020	63.47 (7.36)	49.53 (5.72)	35.59 (4.08)
Summer 2020†	120.82 (14.02)	94.28 (10.89)	67.75 (7.76)
Partial GS 2020†	178.75 (20.74)	139.49 (16.11)	100.22 (11.49)

†T estimate incomplete for season

during the 2020 growing season was more dissimilar to peak lodgepole pine transpiration. Lodgepole pine transpiration peaked for the 8-day period of June 17 through 24, while the largest MODIS ET composite was May 24 through 31. The MODIS estimates perceive a discrepancy in peak ET between 2019 and 2020, similar to what was seen between years in our transpiration estimates.

Figure 5.16 plots the difference (residuals) between the 8-day MODIS ET composites and the lodgepole pine transpiration estimates for the sap velocity radial profiles. Residuals given for each profile and estimation area are for the most part positive values. The east stratum shows the greatest positive residuals out of the three estimation areas. Each of RCM, the east stratum, and the west stratum featured positive residuals that gradually increased in magnitude over the course of winter 2020 into the spring before decreasing toward 0 in the summer. A similar trend is present in 2019 between summer and fall. Large negative residuals are observed for the west stratum in late July and early August 2019, especially for $f_{p,1}(r)$ and $f_{p,2}(r)$. Negative

residuals are also seen for RCM and the east stratum in these months, albeit not as extreme.

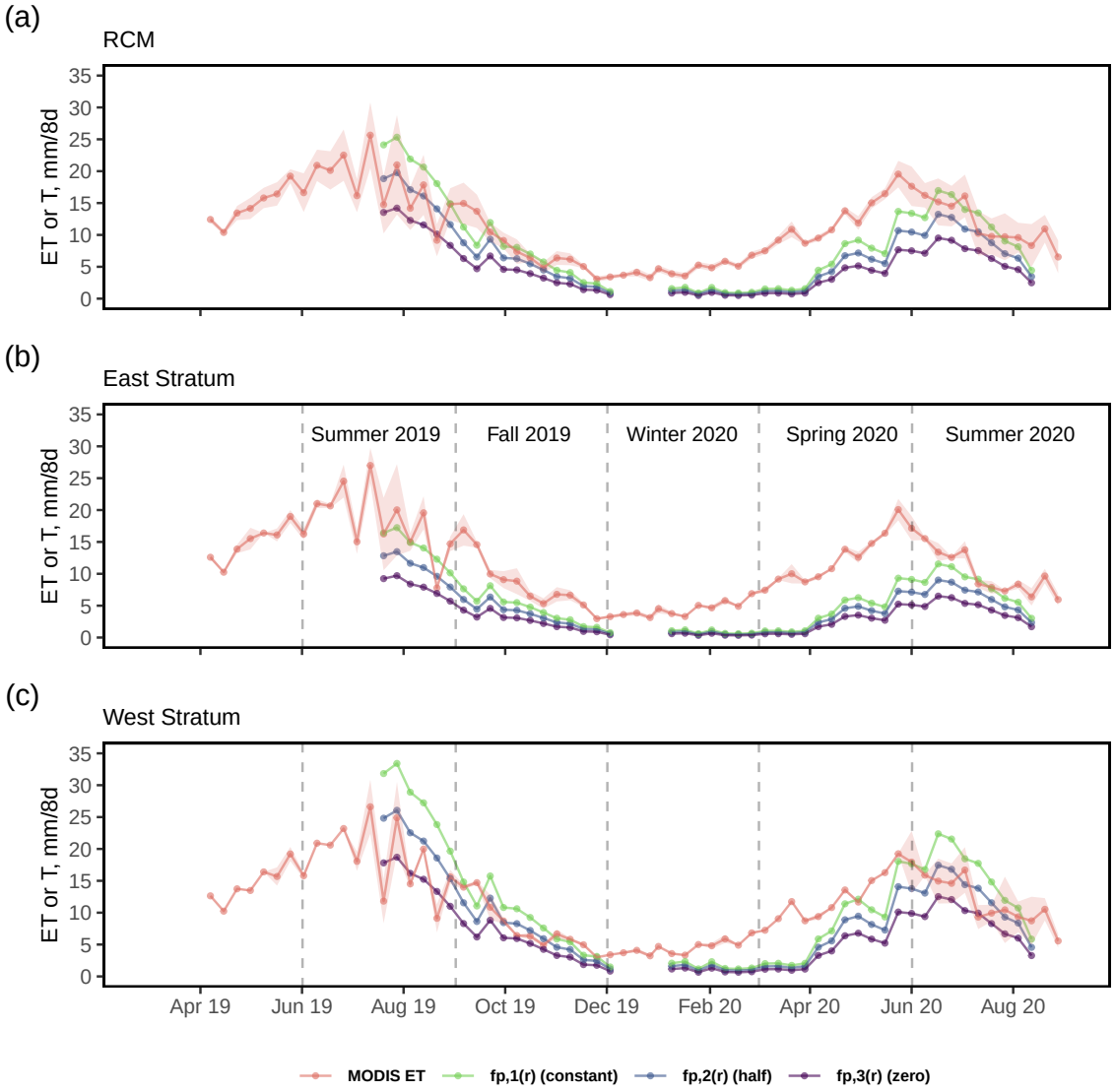

Figure 5.15: Time series of 8-day composite MODIS ET estimates compared with 8-day composite lodgepole pine transpiration (T) estimates by sap velocity radial profile for (a) RCM, (b) east stratum, and (c) west stratum. Ribbons represent ± 1 standard deviation of the MODIS ET 8-day composite, weighted mean.

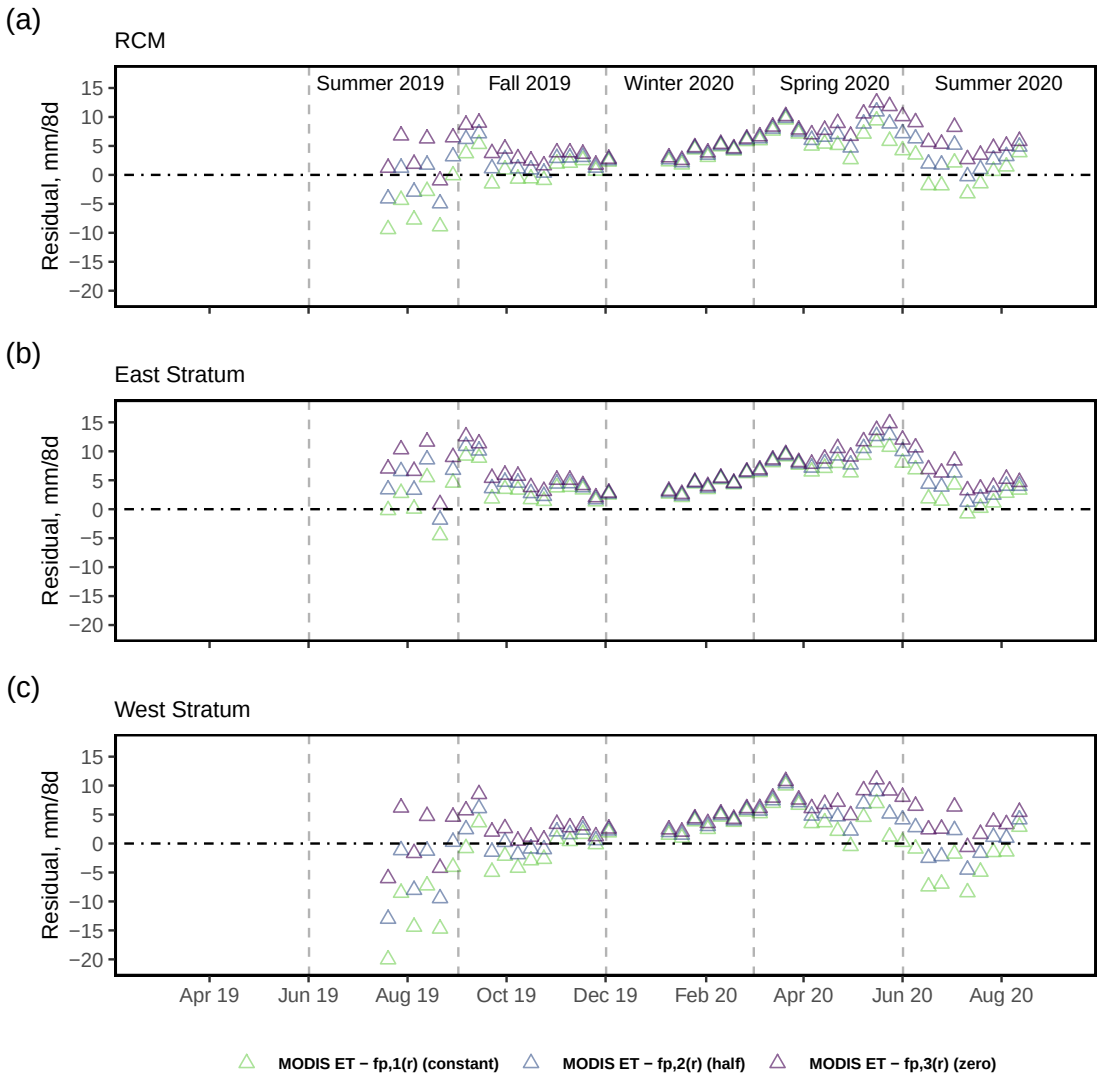

Figure 5.16: Time series of residuals between 8-day composite MODIS ET estimates and 8-day composite lodgepole pine transpiration (T) estimates by sap velocity radial profile for (a) RCM, (b) east stratum, and (c) west stratum.

5.6.3 MJS informed plots

The calibrated MJS model was used to estimate lodgepole pine transpiration for the 25 m x 25 m plots containing soil moisture instruments as shown in Table 5.11 and Figure 5.17. As a reminder, simple scaling transpiration estimates refers to those derived from average sap velocity measurements in the SFP and tree survey results in a given plot. Lodgepole pine transpiration estimates informed by the MJS model were most similar to those produced by the simple scaling for the SFP out of all plots. Simple scaling estimates were slightly greater than MJS estimates for the SFP due to behavior of the model to, on average, under-predict observed sap velocity. Furthermore, the MJS model does not consider nighttime transpiration.

Table 5.11: Comparison of lodgepole pine transpiration totals in soil moisture containing plots informed by the calibrated MJS model and simple scaling for the period of April 7 through August 16, 2020.

	Total T, mm (MJS)			Total T, mm (Simple)		
Plot	$f_{p,1}(r)$	$f_{p,2}(r)$	$f_{p,3}(r)$	$f_{p,1}(r)$	$f_{p,2}(r)$	$f_{p,3}(r)$
SFP (RCSM2b)	65.23	56.67	48.13	69.34	59.94	50.56
RCSM1	58.31	44.98	31.65	90.03	69.45	48.87
RCSM3	70.91	55.53	40.15	85.59	67.02	48.46
RCSM5	320.27	248.10	175.93	303.92	235.43	166.95

MJS model informed lodgepole pine transpiration estimates differed more noticeably from those produced by simple scaling in plots RCSM1, RCSM3, and RCSM5. RCSM1 featured the most extreme differences in estimated transpiration. RCSM1 volumetric soil water content (θ_v) dipped below 18.4% (ML θ_0 parameter estimate) on July 6, 2020 and continued to diminish into the growing season leading to low predictions of sap velocity by the model and consequently low transpiration estimates (Figure 5.17b). Similarly, θ_v dropped below 18.4% in RCSM3 on July 27 leading to

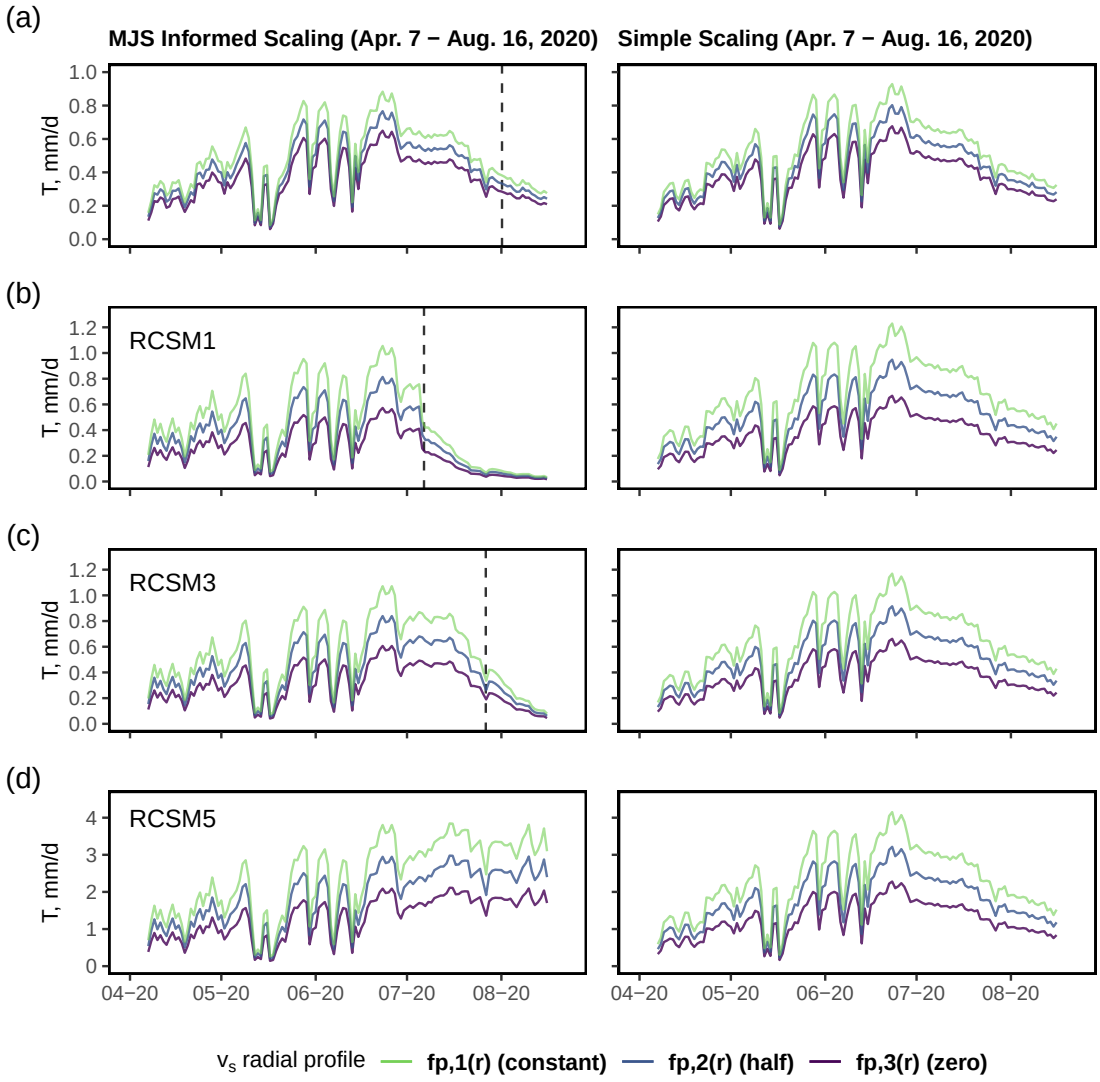

Figure 5.17: Comparison of daily transpiration (T) estimates informed by calibrated MJS model (1st column) and simple scaling (2nd column) for soil moisture set-up containing plots: (a) SFP (RCSM2b), (b) RCSM1, (c) RCSM3, and (d) RCSM5. Vertical dashed lines mark when θ_v dropped below 0.184 during the time period shown in a given plot. Note the differences in vertical scale used for a-d.

low and steadily declining transpiration estimates following this date (Figure 5.17c). The soil moisture limitation perceived by the calibrated MJS model led to smaller transpiration estimates in both RCSM1 and RCSM3 compared to the simple scaling (Table 5.11). RCSM5 was the only plot to feature transpiration estimates greater than those generated by simple scaling. RCSM5 θ_v hovered around 40% for the entire 2020 growing season. The MJS estimates for RCSM5 did not decline into August as opposed to simple scaling estimates because the model assumed θ_v was non-limited.

CHAPTER 6: DISCUSSION

6.1 Qualitative Assessment of Sap Velocity Measurements

Sap velocity (v_s) measurements were collected in the same eight lodgepole pine in the sap flow plot (SFP) for an approximate 1-year period, overlapping partially with the 2019 and 2020 growing seasons. The lodgepole pine v_s measurements followed a distinct diurnal pattern indicative of transpiration during each growing season. The pattern was also present for data collected during fall 2019 (September through November), corresponding with decreases in soil moisture and available energy.

The diurnal pattern in the v_s data was absent or sporadic for late fall 2019, winter 2019, and early spring 2020 corresponding with low daily solar radiation, air temperature, and vapor pressure deficit (VPD) (Figure 5.4 and 5.5). Each of these seasonal periods are indicative of energy/climatic limiting conditions for transpiration. Winter of 2019 featured the lowest sap velocities out of any other season during the SFP campaign, with a mean daytime lodgepole pine average sap velocity ($\bar{v}_s$) of 0.43 $\pm$ 0.36 cm h^{-1} (Table 5.4). The magnitude of $\bar{v}_s$ for late fall 2019 and early spring 2020 was similar to the monitored winter. Past studies, focused on sub-alpine Sierra Nevada ET, have suggested a low air temperature threshold of 5 °C for conifer water use during winter (Cooper et al., 2020; Goulden et al., 2012). Although RCM is at a lower elevation than sub-alpine, our low sap velocities are qualitatively consistent with this literature. Average daytime air temperatures at RCM during periods during late fall 2019, winter 2019, and early spring 2020 hovered around 5 °C on most days. Further, the disappearance of the $\bar{v}_s$ diurnal pattern in late November 2019 was coincident with decreases in air temperature below this threshold (Figure 5.4 and 5.5a). The return of the diurnal pattern in early April 2020 coincided with increases

in air temperature above the 5 °C threshold and the inferred snow pack disappearance at the SFP from net solar radiation measurements (Figure 5.1c, 5.4, and 5.5c).

We observed differences in the lodgepole pine $\bar{v}_s$ measurements between the two partial growing seasons enveloped by the SFP monitoring period (Figure 5.4). The inter-growing season variability in $\bar{v}_s$ is likely attributable to soil water differences between years due to differences in precipitation, as other climatic and energy conditions were similar (Table 5.1). The 2019 WY had greater precipitation than an average year, while the 2020 WY had lower precipitation than average. The annual precipitation differences were reflected in volumetric soil water content (θ_v) and groundwater depth (GWD) between years at RCM (Figure 5.2; Table 5.2). Depth to groundwater at RCW2, representative of the GWD conditions at the SFP, was only within 1 m of the ground surface for a brief period in April 2020. Conversely, the 2019 growing season GWD conditions in eastern RCM given by RCW1 show water within 1 m of the soil surface until early July. The deeper groundwater in 2020 may have influenced the amount of soil water in the vadose zone available for tree use and contributed to earlier soil drying in the 2020 growing season relative to the 2019 growing season.

This study does not allow any definite conclusions to be made as to why we observed such a considerable difference in the $\bar{v}_s$ between years. Peak $\bar{v}_s$ corresponded with near identical θ_v at 45 cm soil depth between 2019 and 2020, 22.5% versus 23.6% respectively. The enhancement in $\bar{v}_s$ in 2019 compared to 2020 suggests that the lodgepole pine in the SFP accessed more abundant soil water located deeper in the soil profile, which was available later into the growing season due to sufficient winter precipitation. Similar observations have been noted for other conifer species during the growing season with antecedent dry and wet winters (Brito et al., 2015; Liu and Biondi, 2020). This speculation would be better substantiated had we measured θ_v deeper in the soil profile. We did, however, conduct a three-dimensional electrical resistivity tomography (ERT) survey over the SFP in July 2020 and July 2021, pro-

viding evidence that the lodgepole pine in the plot accessed soil water deeper than 45 cm. The survey images are shown in Appendix G. The survey from 2020 (pre lodgepole pine removal) showed patches of high resistivity up to 3 m in depth overlapping with instrumented trees, suggesting soil water uptake from this depth (Figure G.1a, G.2a, and G.3a). As a precise rooting depth is not known, there is the possibility that the areas of high resistivity deeper in the soil profile were the result of moisture depletion due to capillary action. Regardless, the depth of high resistivity measurements suggest the lodgepole pine influenced deeper soil water by some mechanism, especially with surveys taking place in the late growing season. The 2021 ERT survey indicative of post lodgepole pine removal provided corroborating evidence, as resistivity was lower in these same patches compared to 2020 (Figure G.1b, G.2b, and G.3b). As previously stated, 2020 and 2021 were comparable dry years.

Our $\bar{v}_s$ measurements in fall 2019 qualitatively suggest that precipitation events that supplement shallow soil moisture augment lodgepole pine transpiration. For example, we observed an increase in $\bar{v}_s$ in late September 2019 following a steady decrease in $\bar{v}_s$ throughout August 2019 (Figure 5.4a). This spike was preceded by several days with rainfall (26.1 mm) and an increase in θ_v at a 0-30 cm soil depth at RCSM1 (Figure 5.2a and 5.2b). There was no θ_v increase associated with this rainfall at the SFP given by RCSM2b, but sensors were positioned deeper compared to RCSM1. Late July 2020 featured a substantial rainfall event (32.5 mm) registered by the NOAA Chester station, but this was unaccompanied by any noticeable increase in $\bar{v}_s$ at the SFP. There is evidence to suggest, however, that this rainfall did not occur at RCM or was lesser in amount, as none of the soil moisture instruments registered an increase in θ_v during this time (Figure 5.2b-c).

6.2 Water Use Response to Drivers During the Dry Growing Season

The calibrated MJS model highlights the sensitivity of lodgepole pine transpiration to energy, atmospheric evaporative demand, and soil water during the 2020 growing season, part of a dry year. Similar to other studies on conifers, fluctuations in solar radiation, VPD, and air temperature appear to modulate the diurnal variability in lodgepole pine $\bar{v}_s$, while soil moisture appears to regulate these relationships in the late growing season (e.g., Link et al., 2014; Looker et al., 2018; Oren et al., 1998a; Pataki et al., 2000). We note that we only monitored and modeled shallow soil moisture, but feel the depth was representative given it was a dry year. Lodgepole pine reached near-maximum transpiration when VPD was above 3.5 kPa and air temperature was greater than 30 °C, when 45 cm θ_v exceeded a threshold of approximately 0.23. The effect of declining θ_v on the relationship between $\bar{v}_{s,n}$ and each of VPD and air temperature is apparent in Figure 5.7b-d.

Lodgepole pine $\bar{v}_{s,n}$ decline in the 2020 growing season corresponded with an approximate decrease in θ_v from 0.23 to 0.17 between late June and mid-August. Shallow soil moisture was not greatly supplemented by rainfall during this period (Figure 5.2a-b). The soil moisture parameter, θ_0, prescribes that the $\bar{v}_{s,n}$ decline is centered on a θ_v value of 0.184. The range of θ_v coincident with $\bar{v}_{s,n}$ decline and θ_0 parameter estimate is comparable to the results of other studies that assessed conifer sap flux density/sap velocity/stomatal conductance response to declining soil moisture. For example, Oren et al. (1998a) found declines in *Pinus taeda* stomatal conductance at a θ_v threshold of 0.22 in a clay loam soil. Pataki et al. (2000) observed a decline in *Pinus contorta ssp. latifolia* sap flux density when soil moisture declined from 0.35 to 0.24 at 0-45 cm depth in an inceptisol during the late growing season of a drought year. We acknowledge, however, that differences in soil properties between sites likely impart variation in tree water use response to soil water conditions. The

SFP in this study featured a sandy loam soil textural class, which typically has field capacity between 0.16 and 0.22, and a wilting point of 0.073 θ_v (Dunne and Leopold, 1998). Our observations of $\bar{v}_{s,n}$ decline and θ_0 model parameter fall within these field capacity bounds, but this might be expected because conifers have been shown to be conservative with water use, especially in drought years (e.g., Royce and Barbour, 2001). The other soil moisture function parameter, k_s, describes the rate of $\bar{v}_{s,n}$ decline under limiting θ_v conditions. Because we did not have observations of $\theta_v <$ 0.17 at the SFP, the decline rate parameter for our site is not well constrained for θ_v < 0.17.

The analysis performed in the present study does not allow us to determine the relative strength of the solar radiation, VPD, air temperature, and θ_v functions in predicting normalized average sap velocity ($\bar{v}_{s,n}$) over the duration of the 2020 partial growing season. A potential approach to disentangle the effects of environmental drivers on $\bar{v}_{s,n}$ with time is to examine the MJS model sensitivity coefficients. Sensitivity coefficients, in the context of the MJS model used in this study, are the derivatives of model-predicted $\bar{v}_{s,n}$ with respect to model parameters. These coefficients would allow determination of the model parameters having the strongest influence on the prediction of $\bar{v}_{s,n}$ at a given time step. The sensitivity coefficient analysis would have been useful in the early growing season for the calibration period, as to assess what climatic variables were most important in predicting $\bar{v}_{s,n}$ when soil moisture was non-limiting. Computation of sensitivity coefficients, however, were outside the scope of the present work.

6.3 Model Performance Using DREAM$_{(ZS)}$ and the GL Function

Several studies have empirically parameterized a MJS model to predict conifer sap velocity/sap flux density or transpiration. Some works have used a MCMC approach

(e.g., Link et al., 2014; Wang et al., 2016, 2020), while others have used optimization routines such as the genetic algorithm and quasi-Newton gradient descent method (e.g., Guyot et al., 2017; Whitley et al., 2013). This present study detailed use of the DREAM$_{(ZS)}$ MCMC algorithm and a generalized likelihood (GL) function in an attempt to avoid severe violations of residual autocorrelation, non-normality, and heteroscedasticity. The approach also allowed an uncertainty assessment for the calibration and validation periods, which is useful when discussing model limitations and generalities. Uncertainty analysis and residual violations are typically not thoroughly addressed in empirical MJS parameterizations (Ford et al., 2005).

DREAM$_{(ZS)}$ and the GL function identified all MJS model parameters within their assumed uniform prior ranges for the calibration period (Figure 5.6a). We integrated various MJS model errors (e.g., errors associated with inputs/forcing data, observations, parameters, and model structural inadequacies) using the GL function that accounts for residual non-normality, autocorrelation, and heteroscedasticity. Similar to the MJS model parameters, the error model parameters were well identified by DREAM$_{(ZS)}$ within their assumed uniform prior distributions (Figure 5.6b).

We produced several diagnostics plots to aid with a discussion of the performance of GL-DREAM$_{(ZS)}$ regarding MJS model error residual non-normality, autocorrelation, and heteroscedasticity (Appendix Figure F.2). The residual error for the calibration period showed a relatively normal distribution with parameterizations of the kurtosis (β) and skewness (ξ) close to 0 and 1 respectively (Table 5.5, Figure 5.6b, and Figure F.2c). Figure F.2d shows the residual autocorrelation plot, which indicates that the calibration period residuals still exhibit statistically significant dependence at higher time lags. The temporal autocorrelation was substantially lessened compared to when we parameterized the model using a formal likelihood function assuming temporally independent and normally distributed residuals (results not shown). Given the short 1-hour observation interval used in the MJS model for this study,

the difficulty of removing residual autocorrelation completely is understandable. A more complex error correlation model is likely needed, but this was not rigorously explored. Regarding residual heteroscedasticity, the plot of residuals versus predicted values indicates the calibration model errors have similar variance/spread (Figure F.2b). Interestingly, the posterior distribution of the slope parameter (σ_0) governing residual heteroscedasticity showed the greatest density for values less than 0. We expected that σ_0 would converge to a value greater than 0 because we were modeling a mean estimate of sap velocity from the instrumented trees; error standard deviations would be expected to increase as a function of $\bar{v}_{s,n}$ due to greater variability between trees at higher sap flows. Conversely, low $\bar{v}_{s,n}$ (i.e., morning or evening sap flow) would correspond with decreased error standard deviations. Our σ_0 parameterization dictated the opposite.

The ML parameter estimates were able to closely replicate the observations of lodgepole pine $\bar{v}_{s,n}$ for the calibration period (RMSE = 0.0874). The model fit was poorer for the validation period (RMSE = 0.1233), but still closely replicated the $\bar{v}_{s,n}$ observations. This result was somewhat surprising, as the validation data were different both spatially and temporally from the calibration data. Ignoring the magnitude of $\bar{v}_s$, the response of $\bar{v}_{s,n}$ to meteorological drivers at the validation site was similar to calibration. High/maximum values of $\bar{v}_{s,n}$ corresponded with comparable values of air temperature, VPD, and θ_v to calibration. The response of $\bar{v}_{s,n}$ to decreasing θ_v into the late growing season is uncertain, but we might expect a different response given the difference in soil properties between calibration and validation sites (e.g., sandy loam versus loam textural classes and differences in soil organic matter content). The shortened validation period also may have impacted the data normalization based on the average of the 99.5th percentile sap velocity values from each tree. It is possible that the validation period failed to capture maximum sap velocity for the entire growing season, as data were not retrievable after July 6th. A lower normalization

constant would result in artificially high $\bar{v}_{s,n}$ values and likely poorer model performance. This might also explain the less severe, negative PBIAS for the validation period compared to calibration.

The model tended to under-predict observations of lodgepole pine $\bar{v}_{s,n}$ for both the calibration and validation periods, as indicated by the negative PBIAS (Table 5.7). Under-predictions were especially prevalent for mid-day $\bar{v}_{s,n}$ observations, corresponding with daily peaks (Figure 5.8 and 5.10). This concurs with other studies using a similar MJS adaptation (e.g., Wang et al., 2016, 2020). These studies attribute the underestimation to model structural deficiencies. For example, Wang et al. (2020) pointed out the failure of MJS models to simulate the full range of sap flow observations due to the inability of the environmental stress functions to equal 1 at the same time. One apparent structural deficiency in our model was the VPD stress function that did not reach maximum $\bar{v}_{s,n}$ over the observed domain of VPD values (Figure 5.7b).

Lastly, the parameter and total predictive uncertainty intervals generated for the calibration and validation periods provides insight as to why including an uncertainty analysis in a MJS model context is beneficial. As communicated in Figure 5.10 and 5.11, parameter uncertainty was small relative to total predictive uncertainty. This result suggests that consideration of parameter uncertainty alone in MJS models is insufficient. Undoubtedly, MJS models feature a myriad of uncertainties stemming primarily from a coarse-grained understanding of the relationship between environmental stressors and the tree physiology controlling water use. There is also incomplete knowledge of the spatial and temporal variability of the environmental input data and tree sap flow response. Our total uncertainty assessment is an attempt to account for such uncertainties and to combat the simplifications made by the MJS model in representing lodgepole pine water use. The total uncertainty intervals for the calibration and validation periods seem reasonable, as they enveloped close to

the theoretically expected 95% of total $\bar{v}_{s,n}$ observations (Figure 5.11). The 81.8% bracketing of total validation observations is noteworthy because the validation data differed in space and time from calibration. What is more, the total uncertainty envelopes captured the majority of midday $\bar{v}_{s,n}$ observations for both periods that were systematically underestimated by our model formulation. Together, the aforementioned results indicate the potential of an uncertainty assessment based on MCMC, Bayesian statistics, and a generalized likelihood function for MJS models.

6.4 Assessment of Lodgepole Pine Transpiration Estimates

6.4.1 Simple scaling

The stratified random sampling (STRS) design employed by this study allowed estimation of lodgepole pine transpiration on a per plot basis for two partitions of the meadow. This was an important consideration for two main reasons. First, the eastern and western regions of RCM differed in their lodgepole pine stem density and sapwood basal area (Table 5.3). The number of trees and sapwood area per plot were the exclusive spatial covariates in the simple scaling approach, so it was important to show how this difference factored into the transpiration estimates for the two strata. Second, we were limited with sap flow equipment. Given our inability to instrument trees in western RCM for the main study period (pre-meadow restoration, coincident with SFP measurements), we acknowledge that the per-plot transpiration estimates for this region are likely less accurate relative to eastern RCM. The STRS design provided the utility of being able to separate our higher confidence transpiration estimate for eastern RCM from that of western RCM. This was preferable compared to providing solely an unnuanced estimate for the entire meadow.

We believe the eastern stratum per-plot lodgepole pine transpiration estimates are more accurate than the western stratum estimates by considering the literature

about transpiration heterogeneity. Many studies cite inter-tree variation in sap flow measurements as a major source of transpiration spatial and temporal variation, with modulators including micro-meteorology, stand structure, topography, and soil moisture conditions (e.g., Adelman et al., 2008; Berry et al., 2017; Looker et al., 2018; Kumagai et al., 2005a; Loranty et al., 2008; Moore et al., 2004; Tromp-van Meerveld and McDonnell, 2006). The potential of soil moisture and v_s spatial autocorrelation is worthy of consideration at RCM because of the discrepancy in soil water between meadow sections, especially in the late growing seasons when we observed earlier soil drying in eastern RCM compared to western RCM (Figure 5.2). Ideally v_s would have been measured in multiple plots in both meadow sections per the recommendations of existing sap flow scaling logic research (Kume et al., 2010; Mackay et al., 2010). Given measurements were only made in the SFP, we cannot definitively rule in or out the potential for spatial and temporal variability in lodgepole pine v_s both inter and intra-strata. We figure higher accuracy in the eastern stratum per-plot lodgepole pine transpiration estimate by nature of the SFP's location in this meadow region. This implies greater homogeneity between the $\bar{v}_s$ derived in the SFP and actual $\bar{v}_s$ in the eastern stratum random plots, relative to the same parameter estimate comparison made for the SFP and western plots.

The results of the comparison between simple scaling transpiration and MODIS ET suggest that our lodgepole pine transpiration estimates are of a reasonable magnitude. Namely the 8-day transpiration composites generated by the three v_s radial profiles for the eastern stratum were generally lower than their MODIS ET counterparts for the entirety of the campaign (Figure 5.15 and 5.16). This result is expected because the sap flow derived estimate is only for lodgepole pine transpiration. The estimate neglects transpiration from other tree and plant species in the meadow, as well as the soil and canopy evaporation ET partitions considered by the MOD16A2 algorithm (Running et al., 2019b). The 8-day composite residuals were closest to

zero for the eastern stratum during fall 2019 and late summer 2020 (Figure 5.16b). This similarity is likely explained by the dry soils and lack of wet canopy surface during these periods. In contrast, larger positive residuals correspond with the winter and spring months when soil and canopy evaporation is expected to comprise a substantial amount of the upward water flux. Consideration of soil evaporation likely explains the discrepancy in the observed timing in peak MODIS ET and sap flow derived lodgepole pine transpiration during the 2020 growing season. The onset of θ_v and GWD decline in the meadow, indicating increased soil evaporation processes, corresponded temporally with the largest MODIS ET composite for May 24 through 31, 2020 (Figure 5.2 and 5.15).

Contrary to the expectation that lodgepole pine transpiration would be consistently lower than MODIS ET, we calculated negative 8-day composite residuals for the western stratum (Figure 5.16c). The negative residuals occurred during late summer 2019, fall 2019, and summer 2020, and were especially pronounced for the $f_{p,1}(r)$ transpiration estimate. On one hand, this disagreement might be due to inaccuracy in the lodgepole pine transpiration estimate for the western stratum, consequence of its derivation from sap flow measurements made in eastern RCM. However, the transpiration estimates computed from the $f_{p,2}(r)$ and $f_{p,3}(r)$ radial profiles were more comparable to the MODIS ET (i.e., less negative residuals than $f_{p,1}(r)$). We would expect lodgepole pine transpiration to comprise a larger proportion of the ET flux in western RCM relative to eastern RCM given the high density and sapwood area of lodgepole pine trees, coupled with more ample soil water in this meadow region (Figure 5.2; Table 5.2 and 5.3). This emphasizes that the $f_{p,1}(r)$ radial profile likely overestimates lodgepole pine transpiration in assuming a constant sap velocity across the sapwood radial profile. Past research has shown evidence that conifers, including lodgepole pine, generally exhibit a decrease in v_s magnitude with sapwood depth (Berdanier et al., 2016; Ford et al., 2004; Mark and Crews, 1973).

On the other hand, the MODIS ET composites for the meadow strata may be inaccurate due to product pixel coarseness and/or limitations of the MOD16A2 algorithm for our study area. Figure 5.16 suggests the former, as the MODIS ET composites are similar among the east stratum, west stratum, and RCM. Notably, the MOD16A2 estimates are slightly larger for the eastern stratum compared to the western stratum, whereas we would expect the opposite to be true. This similarity is due to the MOD16A2 pixel spatial distribution and size. Unfortunately, the pixels overlapping RCM are not independent for the two stratum and also capture adjacent forested areas outside the meadow boundary (Figure B.2). Regarding the accuracy of the MODIS estimate, past studies have compared MODIS ET product estimates to ET informed by flux tower measurements in similar environments to RCM (Jepsen et al., 2021; Vinukollu et al., 2011). Jepsen et al. (2021) found that monthly flux tower measurements in the southern Sierra Nevada (CA, USA) were consistently underestimated by the MOD16A2 ET product. Comparisons were carried out for wet and dry years at lower (1160 m), middle (2015 m), and upper (2700 m) elevation sites dominated by conifer species, including lodgepole pine at the upper site. The work attributed large underestimations of warm-season ET to the MOD16A2 algorithm imposing an over-excessive VPD limitation on canopy conductance for the study site; the algorithm accounts for water stress on transpiration using VPD (Running et al., 2019b). The findings of Jepsen et al. (2021) suggest that the MODIS ET estimate for our study site may be lower than the true ET, especially for the growing season months in the western stratum.

Further putting our simple scaling lodgepole pine transpiration estimates into context is a comparison to transpiration estimates made for lodgepole pine/other conifers in other studies. We feel our eastern stratum transpiration estimates are best juxtaposed with growing season sap flow observations made in forested environments under comparable hydrologic conditions. One example is Pataki et al. (2000), who

estimated an average transpiration rate of 2.7 ± 0.6 mm/d for pine-fir dominated plots (including *Pinus contorta ssp. latifolia*) during a dry growing season in the Medicine Bow Mountains (WY, USA). Our eastern stratum transpiration estimates for summer 2020 provide a good point of comparison because they are part of a monitored dry growing season, aligning with the June to August time period analyzed in the referenced study. We estimated average daily lodgepole pine transpiration for eastern plots between 0.60 ± 0.08 and 1.06 ± 0.14 mm/d given by $f_{p,3}(r)$ and $f_{p,1}(r)$ respectively (Figure 5.14a and Table E.1). Two reasons related to sap flow scaling may explain why our estimates are on the lower end. First, our estimates do not sum transpiration from non-lodgepole pine tree species, which comprised on average 6.5% of the total stem density and 29.6% of the total basal area per hectare in the eastern stratum (Table 5.3). Secondly, our eastern stratum lodgepole pine sapwood area to ground area ratio (i.e., sapwood basal area) of 10.77 ± 0.84 cm^2 m^{-2} is much lower than the 48.8 ± 15 cm^2 m^{-2} reported for pine-fir plots by Pataki et al. (2000). We note that the higher standard error in the per plot estimates of Pataki et al. (2000) is consequence of the small plot size used in their study. In another work conducted by Spittlehouse (2002) at Upper Penticton Creek (British Columbia, Canada), old growth lodgepole pine transpiration was estimated by sap flow between 1 and 1.5 mm/d during mid-summer. The transpiration rate decreased to 0.5 mm/d in late August and September when soil moisture dropped below -0.5 MPa in a sandy loam soil. These values are similar in magnitude to the eastern stratum estimates given by $f_{p,1}(r)$ and $f_{p,2}(r)$ during summer 2020, that dropped significantly with decreases in θ_v deeper into the growing season (Figure 5.14a). As previously stated (Section 3.4), eastern RCM featured soil with a sandy loam textural class. We compare the upper end estimates given by $f_{p,1}(r)$ and $f_{p,2}(r)$ because Spittlehouse (2002) did not account for sap flow decline with sapwood depth in their scaling approach.

Lastly, we contrast our simple scaling lodgepole pine transpiration estimates made for RCM (strata aggregate mean) to ET estimates for similarly degraded mountain meadow environments. Hammersmark et al. (2008) estimated the annual ET in a channel-incised meadow (near Redding, CA, USA) between 530 and 419 mm using a MIKE SHE hydrologic modeling system. Although the primary degradation mechanism for this meadow was not conifer encroachment, the meadow featured pine and ash forest that was factored into the ET computation. Our lodgepole pine transpiration for RCM over the approximate 1-year monitoring period was estimated between 220.57 $\pm$ 25.28 mm and 393.39 $\pm$ 45.65 mm, given by $f_{p,3}(r)$ and $f_{p,1}(r)$ respectively. In a more comparable study, Surfleet et al. (2020) estimated soil ET for Marian Meadow (near Chester, CA, USA) prior to restoration by lodgepole pine removal. Marian Meadow and RCM had comparable basal areas prior to restoration, 25.04 versus 29.54 m^2 ha^{-1} respectively. Soil ET was estimated as 285 and 268 mm for two pre-restoration water years at Marian Meadow, with the first estimate derived from a dry water year. Both rates are bracketed by our upper and lower lodgepole pine transpiration estimates for RCM. As previously discussed, we reason that the lodgepole pine transpiration would be on the lower end of this range, given knowledge about the v_s radial profile for this tree species.

6.4.2 MJS informed scaling

The results of the MJS informed scaling and comparison to the simple scaling approach highlight some of the benefits and limitations of using the calibrated model to estimate lodgepole pine transpiration at RCM. The inclusion of θ_v as another covariate is the clear benefit of our employed model scaling, at least in principle. Soil moisture conditions were spatially and temporally variable throughout RCM during the 2020 growing season, as measured by the four instrument set-ups (Figure 5.2a-b). The benefit of including θ_v in a scaling approach compared to the simple scaling is

apparent for the RCSM5 plot estimate. RCSM5 showed ample soil moisture into the late growing season, so that soil moisture conditions were perceived as unlimited to lodgepole pine transpiration by the model (Figure 5.2b and 5.17d). The MJS model validation for $\bar{v}_{s,n}$ data in western RCM supports this, as observations of high $\bar{v}_{s,n}$ were maintained with observations of high θ_v (Figure 5.9d). Therefore, the simple scaling logic likely produces an inaccurately low transpiration for the late-growing season in the RCSM5 plot.

In contrast to RCSM5, the RCSM1 and RCSM3 set-ups recorded θ_v values commensurate with lodgepole pine transpiration soil moisture limitation perceived by the calibrated model during the growing season. This contributed to lower predicted transpiration in these plots compared to the simple scaling, especially after θ_v dropped below 18.4% (Figure 5.17b-c). The rate of decline in predicted transpiration was especially steep after this threshold. This observation illuminates the poor constraining of the k_s parameter in our calibrated model; both RCSM1 and RCSM3 recorded θ_v values lower than what was observed in the SFP during the calibration period. We would have higher confidence in the predicted transpiration in plots RCSM1 and RCSM3 had the MJS model been calibrated using the full range of θ_v observations in all soil moisture monitored plots. Also, as discussed previously, our MJS model validation exercise was limited because we did not record any θ_v values coincident with the v_s decline observed during model calibration. This has greater bearing on the MJS derived transpiration estimates in RCSM3, as this plot was located in western RCM. There is uncertainty, therefore, if the lodgepole pine in this plot would respond consistently with the SFP to declines in θ_v. Overall, these results emphasize the need to calibrate the model for a longer period of time and a deficiency created by model calibration at one meadow location.

Apart from the aforementioned limitations associated with the soil moisture stress function, there are several other model deficiencies that limit the MJS informed scaling

at RCM. Firstly, the approach requires knowledge about average maximum sap velocity for lodgepole pine. Our model formulation used the average of the 99.5th percentile v_s values from the instrumented SFP trees, but other studies using a MJS scheme also rely on an observed maximum $\bar{v}_s$ or transpiration rate for a given tree species (e.g., Link et al., 2014; Wang et al., 2020). Others allow this maximum to be parameterized in the model (e.g., Guyot et al., 2017; Wang et al., 2016; Whitley et al., 2009, 2013). In the model-based scaling, it is assumed that the derived maximum $\bar{v}_s$ is spatially universal for RCM during the 2020 growing season. This is an unlikely assumption, especially for extrapolation to western RCM given the soil moisture discrepancy in this meadow region. Secondly, the MJS model used in this study is not able to simulate nocturnal sap velocity, as is the case with most MJS models (Wang et al., 2020). Our data show nocturnal v_s was present during the 2020 growing season (Table 5.4).

Finally, the comparison between the MJS informed and simple scaling lodgepole pine transpiration estimates for the SFP suggest the model-based scaling approach in this study has potential application in a mountain meadow site water balance (Figure 5.17a). Given the evaluated time period in this study, we limit the suggestion to growing seasons. The simple scaling based transpiration estimates derived from the $f_{p,1}(r)$, $f_{p,2}(r)$, and $f_{p,3}(r)$ radial profiles were only under-estimated by 6.11%, 5.61%, and 4.92% respectively by the model (Table 5.11). The magnitude of underestimation is comparable with the results of Wang et al. (2016), who found similar underestimation for an hourly MJS model based transpiration estimate. Our suggestion based on the SFP's MJS informed estimate, however, implies that a site water balance would be best constructed if the model were calibrated using sap flow data from multiple locales within a given site. In light of the limitations discussed above, the model calibration need consider the full range of measured θ_v, intra-meadow variation in

maximum $\bar{v}_s$, and magnitude of nocturnal sap flow, all in context of the evaluated time period.

6.5 Additional Limitations and Uncertainties

6.5.1 Sap flow measurement limitations

There are several limitations in the sap flow measurements in this study that warrant discussion: (1) tree wound response, (2) assumptions about sapwood traits, (3) chosen sizes/number of instrumented trees, and (4) treatment of sap velocity (v_s) as proportional to transpiration. Each of these limitations contributes potential uncertainty to the meadow transpiration estimates.

During the SFP campaign, the sap flow probes were not re-installed, which risks artificially low heat velocity (v_h) measurements due to the tree wounding response (Barrett et al., 1995). We corrected our v_h measurements over the course of the campaign using two sets of the published wound correction coefficients from Burgess et al. (2001); it appeared the wounding process was dynamic over time, with wounding worsening between summer/fall 2019 and spring 2020. Because we measured the wound diameter at the end of the campaign (average wound of 2.4 $\pm$ 0.3 mm), we have higher confidence in the wound correction applied to the later data collected between April 1 and August 16, 2020. There is higher uncertainty in the wound correction applied between July 2019 and April 1, 2020, which was based off a 1.9 mm wound diameter according to the anatomical investigations by Barrett et al. (1995). Overall, heat pulse based sap flow methods, such as the heat ratio method (HRM) in this study, lack a robust methodology to dynamically correct against tree wound response errors, as opposed to some thermal dissipation based methods (Peters et al., 2018).

We made assumptions about lodgepole pine sapwood traits including sapwood moisture content (m_c), sapwood depth (D_s), and the radial profile of sap velocity (v_s) that introduce uncertainty into our transpiration estimates. In converting our corrected heat velocity (v_c) measurements to v_s, we assumed that m_c was constant throughout the measurement period; however, there is evidence this parameter is seasonably variable in lodgepole pine (Markstrom and Hann, 1972). We used an average m_c from measurements made in a dry season (August 2020) and wet season (May 2021), so that the parameter would represent an intermediate value. Looking at Equation 4.2, this assumption might result in slight underestimation of v_s during the wet season and a slight overestimation during the dry season. Sapwood moisture content was also used in the calculation of thermal diffusivity (α), alongside other parameters related to fresh sapwood that would also vary seasonally given their relation to sapwood water content (Equation 4.6-4.8). With regards to D_s, using a regression-based D_s estimate to integrate v_s across the sapwood can cause significant error (Kumagai et al., 2005b; Looker et al., 2016). This is a possibility in this study because the singularly sampled sapwood cores that inform our relationship neglect D_s variability around the tree bole. This potential error is not factored into our transpiration estimates. Lastly, of the aforementioned sapwood trait assumptions, the uncertainty surrounding the assumed v_s radial profile is the only one we attempt to quantify through our $f_{p,1}(r)$, $f_{p,2}(r)$, and $f_{p,3}(r)$ profiles.

The size of instrumented trees (10-40 cm) were chosen in the SFP to span a wide range of DBH, as is the approach in many studies (Oren et al., 1998b). The number of selected larger DBH trees was disproportionate to the number of smaller DBH trees when considering the diameter distribution was positively skewed in the meadow, especially for the eastern stratum plots (Figure 5.3). Studies on sap flow scaling have advocated that the selection of instrumented trees consider not just the range of tree size in an area of interest, but also the distribution (i.e., DBH spatial arrangement

and moments) (e.g., Köstner et al., 1998; Kumagai et al., 2008; Mackay et al., 2010; Tromp-van Meerveld and McDonnell, 2006). Our lack of v_s measurements in small trees (DBH $<$ 10 cm) might mean that the derived average sap velocity ($\bar{v}_s$) was not completely representative of the trees contained in RCM; however, there was limitation from the start with only eight available sap flow probes. At the same time, we did not perceive any relationship between DBH and magnitude of v_s as documented in some studies (e.g., Berry et al., 2017; Jung et al., 2011; Kume et al., 2010; Meinzer et al., 2005). The highest magnitude (active depth) measurements collected in each tree showed strong positive correlation with each other throughout the SFP campaign (Appendix Figure E.3). It is possible that some kind of relationship between v_s and DBH exists for the lodgepole pine at RCM, but thorough exploration of this is limited by the sample size.

The number of available probes also restricted careful consideration for azimuthal variation in v_s around the tree bole with our probe installation (Shinohara et al., 2013; Tateishi et al., 2008; Tsuruta et al., 2010). We chose to allocate our available probes between trees, as to capture inter-tree variations in v_s. A study by Shinohara et al. (2013) suggested inter-tree variation was more important in minimizing sap flow scaling error relative to azimuthal variation.

Finally, by treating v_s as proportional to transpiration we neglect potential temporal heterogeneity in the assumed v_s radial profile and changes in water storage between the probe location and canopy. Ford et al. (2004) found non-constant radial profiles in *Pinus* spp. trees for sub-daily time frames, which suggests our assumption of a temporally constant profile for lodgepole pine is a simplification. Neglecting the contribution of water storage, including sap flow lags along the tree height, likely also introduces error to our transpiration estimates (Čermák et al., 2007; Kumagai et al., 2009; Loustau et al., 1996; Waring and Running, 1978). The error associated with this assumption, however, can be less extreme for daily estimations of transpiration

compared to sub-diurnal estimations in certain tree types that have small amounts of daily stem water change. For example, Waring and Running (1978) showed less than 5% daily water storage change in Douglas-fir. Moreover, previous results for conifer trees have evidenced that stored water typically comprises $< 30\%$ of daily transpiration, including large trees (Phillips et al., 2003). It has also been shown in sap flow scaling applications that water storage error is negligible if inter-tree v_s variability is low (Loustau et al., 1996).

6.5.2 Other environmental measurements/data limitations

In addition to the limitations in sap flow measurements for this study, there were limitations associated with soil moisture and climate data. The volumetric soil water content (θ_v) input data for the MJS model was based off the average from two time domain reflectometry (TDR) sensors at 45 cm depth. We acknowledge that these point measurements imperfectly represent the available water to the instrumented SFP lodgepole pine. Overall, the location of the lodgepole pine roots in the SFP were uncertain, but our results from the ERT surveys suggest tree induced soil water depletion between 0 and 3 m depth (Figure G.1, G.2, and G.3). Whether the tree roots depleted water from these depths directly or via an induced upward water potential gradient is uncertain. Prior sap flow studies on *Pinus contorta ssp. latifolia* have assumed or stated shallow rooting, < 1 m (Pataki et al., 2000; Spittlehouse, 2002). The calibrated model may have performed better had we included deeper θ_v data, especially because the model was calibrated during a dry growing season with an antecedent dry winter. Guyot et al. (2017) showed evidence supporting this for a subtropical coastal conifer forest (South-East Queensland, Australia) that featured a shallow unconfined aquifer system. Apart from model analyses, inclusion of deeper θ_v data would have allowed us to comment further on the discrepancy in observed $\bar{v}_s$ between the 2019 and 2020 partial growing seasons.

The climate data used in this study was retrieved from one climate station located in the SFP. The station provided the meteorologic input data for MJS model calibration; however, using data from the same location to preform model validation and the model informed transpiration scaling neglects potential heterogeneous meteorology in the meadow. Still, the MJS model validation showed comparable responses to climate drivers relative to calibration, suggesting that severe micro-meteorology was not present at the validation site (Figure 5.8 and 5.9a-c).

6.6 Improvements and Future Work

The primary limitation surrounding lodgepole pine transpiration estimation in this study was the lack of sap flow measurement in the western portion of RCM. This required extrapolation of $\bar{v}_s$ from the SFP in order to complete both simple scaling and MJS model informed lodgepole pine transpiration estimation. The structural bias would have been mitigated in this study had we used a multiple sap flow plot design, as to capture a more representative tree size distribution and potential $\bar{v}_s$ heterogeneity between meadow strata. Using multiple probes per tree, as opposed to one per tree, would also contribute to a more robust $\bar{v}_s$ estimate in individual plots. In addition to more sap flow measurements (i.e., plots), inclusion of spatially corresponding micro-meteorological and soil moisture measurements would allow multiple MJS model calibrations and an assessment of the intra-meadow variation in lodgepole pine $\bar{v}_s$ response to model environmental drivers. The multi-plot approach would mold well into the STRS design implemented in this study and extend uncertainty assessments surrounding transpiration estimates beyond the variability we presently assess (i.e., variability associated with stem density, sapwood area, and three variants of a $\bar{v}_s$ radial profile). More work could also be done to reflect the error in sapwood

traits in estimating transpiration as per the recommendations of other authors (e.g., Looker et al., 2016).

Future work is also recommended to focus on the continued use of $\text{DREAM}_{(\text{ZS})}$ and the GL function in parameterizing MJS models and assessing model parameter and total uncertainty. As shown in the results of this study, the GL function approach has potential in a MJS model context, especially for uncertainty assessments. Some questions still remain, however, surrounding the GL error model implemented in this work. Namely, there was difficulty in completely removing residual autocorrelation given the high temporal resolution of our response variable. We also obtained residual heteroscedasticity parameters within the error model that were non-conducive to increasing error in $\bar{v}_s$ with increasing $\bar{v}_s$ magnitude. More work could be done to investigate and potentially resolve these components of the error model, perhaps by using different representations for the non-constant variance and correlated error components. Future work could also propagate parameter and total uncertainty into MJS informed transpiration estimates and explore the use of this methodology to parameterize models at different temporal scales (Wang et al., 2016). Regarding the latter, it would be useful to calibrate a MJS model using data collected during a wet growing season with an antecedent wet winter, as to compare parameter values to those from the dry growing season in this study.

CHAPTER 7: CONCLUSION

The replacement of mountain meadow vegetation by conifer forest is a well documented phenomenon contributing to meadow degradation in the western USA. Although past research has focused on conifer removal as a restoration technique, there has been little work done to assess conifer water use in these environments in a pre-restoration state. The results of this study contribute information about *Pinus contorta ssp. murrayana*, lodgepole pine, transpiration in a mountain meadow environment. As meadows in the southern Cascades and the Sierra Nevada are commonly encroached by this conifer species, this work contributes valuable knowledge about the water consumption and environmental drivers of lodgepole pine transpiration, particularly in dry growing seasons. Knowledge of lodgepole pine water consumption is useful to meadow restoration efforts where the common objective is the recovery of herbaceous meadow vegetation that rely on ample soil water availability. Information about the environmental drivers of water use during dry growing seasons is important because of the expected changes in climate that will favor these conditions in the future. In addition, the applied sap flow scaling and modeling methods in this study contribute information about transpiration quantification techniques in mountain meadows and similar environments.

The primary goal of this study was to estimate lodgepole pine transpiration in Rock Creek Meadow (RCM) for an approximate 1-year period intersecting the 2019 and 2020 partial meadow growing seasons. In recognition of the spatial heterogeneity of the lodgepole pine at the meadow and other environmental factors that can potentially influence transpiration, we employed a stratified random sampling (STRS) design in a simple, bottom-up sap flow scaling approach. The sampling and scaling approach allowed separate per-plot total and daily average transpiration estimates for

the eastern stratum, western stratum, and RCM (i.e., meadow population estimate). Average total transpiration for random plots in the eastern stratum (drier, less vegetated portion of meadow) was estimated by the simple scaling approach between 149.74 ± 12.06 and 266.05 ± 20.81 mm for the monitoring period (mid-July 2019 to mid-August 2020). The lower end of this estimation was produced assuming that the radial profile of sap velocity (v_s) declined linearly across tree sapwood to zero at the heartwood-sapwood boundary ($f_{p,1}(r)$), while the upper end assumed constant v_s across tree sapwood ($f_{p,3}(r)$). The eastern RCM per-plot estimate for the 2020 partial growing season (April to mid-August 2020) was given as 67.82 ± 5.46 and 120.50 ± 9.43 mm by the same two radial profiles. The random plots in the western stratum (wetter, more vegetated portion of meadow) approximately doubled the eastern stratum estimate for these periods, between 288.64 ± 54.71 mm and 515.72 ± 98.96 mm for the entire campaign and between 130.73 ± 24.78 and 233.58 ± 44.82 mm for the 2020 partial growing season. Lastly, average total transpiration for the entire meadow was estimated between 220.57 ± 25.28 and 393.39 ± 45.65 mm for the campaign and between 100.22 ± 11.49 and 178.75 ± 20.74 mm for the 2020 partial growing season. Provided the previously discussed limitations imposed by our scaling approach and the location of sap flow measurement in eastern RCM, we are most confident in the eastern stratum transpiration estimates. Furthermore, we expect that the true lodgepole pine transpiration is on the lower end of the v_s radial profile intervals because of the evidence of a sap flow radial gradient in lodgepole pine trees (Berdanier et al., 2016; Ford et al., 2004; Mark and Crews, 1973).

Although we are most confident in the eastern stratum transpiration estimates, the analysis comparing lodgepole pine transpiration estimates to moderate resolution imaging spectroradiometer (MODIS) derived evapotranspiration (ET) (MOD16A2GF product) revealed that the magnitude and timing of the estimated transpiration for each meadow partition is reasonable. The comparisons revealed mainly positive resid-

uals between MODIS ET and lodgepole pine transpiration, with the magnitude residuals increasing seasonally during periods when tree transpiration would comprise a low percentage of the ET flux (e.g, winter and early spring). Some negative residuals were produced in the comparison for western RCM, especially during the late growing seasons, suggesting disagreement with the MODIS product and potential inaccuracy in the estimated transpiration for this region. At the same time, we acknowledge the potential deficiencies in the MOD16A2 product for estimating ET at locations like RCM (Vinukollu et al., 2011; Jepsen et al., 2021).

The second half of the goal for this study was to investigate environmental drivers of lodgepole pine transpiration for a dry growing season. To do so, a modified Jarvis-Stewart (MJS) model was calibrated and validated to hourly normalized average sap velocity ($\bar{v}_{s,n}$) data collected in two different parts of the meadow during the 2020 and 2021 partial growing seasons. Both the 2020 and 2021 growing seasons were dry, with antecedent winters witnessing below average precipitation. The model was calibrated using a variation of the DiffeRential Evolution Adaptive Metropolis (DREAM) algorithm known as DREAM$_{(ZS)}$ and a generalized likelihood (GL) function in an attempt to heed error residual assumptions and complete a thorough uncertainty assessment. To the author's knowledge this is the first attempt to parameterize a MJS model using DREAM$_{(ZS)}$ and a GL function.

Model calibration showed good agreement between observed and predicted $\bar{v}_{s,n}$ using the maximum likelihood parameter estimates (ML) (RMSE = 0.0874, 1.25 cm h^{-1} after removing normalization constant), but also featured negative PBIAS. The results of these model performance metrics are comparable with other works employing a MJS model. The diurnal variation in incoming solar radiation, air temperature, and VPD modulated lodgepole pine $\bar{v}_{s,n}$ early in the growing season, until a perceived soil moisture limitation corresponding with approximate decreases in volumetric soil water content (θ_v) from 0.23 and 0.17 at 45 cm soil depth between late June and mid-

August. Near-maximum $\bar{v}_{s,n}$ corresponded with VPD > 3.5 kPa and air temperature > 30°C, when 45 cm θ_v exceeded the 0.23 threshold. Comparable model performance was achieved for the validation period using the ML parameter estimates gathered in calibration (RMSE = 0.1233, 2.05 cm h^{-1} after removing normalization constant) and negative PBIAS. High $\bar{v}_{s,n}$ at the validation site corresponded with similar air temperature, VPD, and θ_v conditions observed for calibration. The similar model performance between calibration and validation suggests that the lodgepole pine in the two meadow regions respond similarly to meteorological drivers during dry growing seasons; however, the soil moisture response cannot be compared because the range of θ_v associated with $\bar{v}_{s,n}$ decline was not observed during the validation period.

Overall, the modeling analysis suggests that future warmer and drier growing seasons in this region may present more occurrences of limited lodgepole pine water consumption, especially in the late growing season. This study, however, was limited in a few aspects that prohibited rigorous exploration of certain hydrologic and climatic characteristics that may influence lodgepole pine transpiration in mountain meadows within the context of a changing climate. First, the analysis in our study did not allow us to decipher the relative effects of model parameters (i.e., environmental drivers) on predicted sap flow over the course of the growing season. A sensitivity coefficient analysis would allow this. This would be especially useful toward disentangling the effects of climatic variables on tree water use in the early growing season when soil water is non-limiting, which is relevant with anticipated shifts in energy inputs with climate change. Second, no formal analysis was done to assess late growing season rainfall effects on lodgepole pine transpiration due to the lack of precipitation events in the late 2020 growing season. Outside of the modeled period, we observed several rainfall events that augmented shallow soil moisture and subsequently lodgepole pine transpiration in fall 2019. This warrants further investigation given increasingly variable precipitation with climate change in the western USA, including high intensity

summer rain events. Lastly, expanding beyond the scope of a single growing season, this study showed a dichotomy in the magnitude of lodgepole pine $\bar{v}_s$ between the 2019 and 2020 growing seasons, seemingly attributable to differences in winter precipitation between years. This observation invites more work focused on inter-annual variability in lodgepole pine transpiration, as inter-annual variation in precipitation is also expected with changing climate in this region.

The total predictive uncertainty 95% confidence interval determined from the GL error model bracketed close to theoretically expected 95% of total $\bar{v}_{s,n}$ observations for both calibration and validation periods. This was an encouraging result when considering the prevalent structural deficiencies of MJS models, especially a tendency for predicted values to underestimate observed values during times of high sap flow (i.e., midday). Overall, this first application of the GL function and total uncertainty assessment methodology shows potential for future use with MJS models, at least for the growing season period explored in this work.

Lastly, the calibrated MJS model was used to inform transpiration scaling for the 2020 partial growing season and compared to the simple scaling estimates in select plots. The comparisons revealed the potential utility the MJS scaling provides by including θ_v as another $\bar{v}_s$ covariate. We were limited in this exercise, however, by the poor constraining of the soil moisture function parameter in the model describing the decline rate of sap flow decline with limiting soil moisture conditions (k_s). The comparison for the SFP suggests the model-based approach has potential for application in a mountain meadow site water balance, at least for a growing season. As discussed, however, a implementation would need to ensure the calibrated model considers the the diversity of θ_v in the meadow and intra-meadow variation in maximum sap flow. Therefore, it is recommended that the model be calibrated over a sufficient time period and/or multiple locales within a study site.

The conclusions presented herein were based on the results of a two year study at Rock Creek Meadow. Subsequent work will integrate the lodgepole pine transpiration estimates derived from simple scaling into a pre-restoration water budget. Future work and research could include: (1) expansion of the sampling design to capture intra-meadow variability in lodgepole pine sap flow and response to environmental drivers, (2) further implementation of $\text{DREAM}_{(\text{ZS})}$ and a GL function to parameterize and quantify uncertainty in Jarvis-type transpiration (and stomatal conductance) models, and (3) additional evaluation of lodgepole pine sap flow and response to environmental drivers, during both dry and wet years.

REFERENCES

Adelman, J.D., Ewers, B.E., Mackay, D.S., 2008. Use of temporal patterns in vapor pressure deficit to explain spatial autocorrelation dynamics in tree transpiration. Tree Physiology 28, 647–658. doi: 10.1093/treephys/28.4.647.

Albano, C.M., McClure, M.L., Gross, S.E., Kitlasten, W., Soulard, C.E., Morton, C., Huntington, J., 2019. Spatial patterns of meadow sensitivities to interannual climate variability in the Sierra Nevada. Ecohydrology 12, e2128. doi: 10.1002/eco.2128.

Allen, R.G., Pereira, L.S., Raes, D., Smith, M., 1998. Crop Evapotranspiration-Guidelines for Computing Crop Water Requirements. FAO Irrigation and Drainage Paper 56. Food and Agriculture Organization of the United Nations. Rome, Italy.

Allen-Diaz, B.H., 1991. Water table and plant species relationships in Sierra Nevada meadows. American Midland Naturalist 126, 30–43. doi: 10.2307/2426147.

AppEEARS Team, 2020. Application for extracting and exploring analysis ready samples (AppEEARS). URL: https://lpdaacsvc.cr.usgs.gov/appeears. (accessed 11 June 2021).

Barrett, D., Hatton, T., Ash, J., Ball, M., 1995. Evaluation of the heat pulse velocity technique for measurement of sap flow in rainforest and eucalypt forest species of south-eastern Australia. Plant, Cell & Environment 18, 463–469. doi: 10.1111/j.1365-3040.1995.tb00381.x.

Becker, P., 1998. Limitations of a compensation heat pulse velocity system at low sap flow: implications for measurements at night and in shaded trees. Tree Physiology 18, 177–184. doi: 10.1093/treephys/18.3.177.

Becker, P., Edwards, W., 1999. Corrected heat capacity of wood for sap flow calculations. Tree Physiology 19, 767–768.

Berdanier, A.B., Miniat, C.F., Clark, J.S., 2016. Predictive models for radial sap flux variation in coniferous, diffuse-porous and ring-porous temperate trees. Tree Physiology 36, 932–941. doi: 10.1093/treephys/tpw027.

Berlow, E.L., D'Antonio, C.M., Reynolds, S.A., 2002. Shrub expansion in montane meadows: the interaction of local-scale disturbance and site aridity. Ecological Applications 12, 1103–1118. doi: 10.1890/1051-0761(2002)012[1103:SEIMMT]2.0.CO;2.

Berry, Z.C., Looker, N., Holwerda, F., Gómez Aguilar, L.R., Ortiz Colin, P., González Martínez, T., Asbjornsen, H., 2017. Why size matters: the interactive influences of tree diameter distribution and sap flow parameters on upscaled transpiration. Tree Physiology 38, 263–275. doi: 10.1093/treephys/tpx124.

Bochard, S., 2004. Soil Survey of Susanville Area, Parts of Lassen and Plumas Counties, California. Natural Resources Conservation Service, United States Department of Agriculture. Washington, DC, USA.

Bouguerra, A., Aït-Mokhtar, A., Amiri, O., Diop, M., 2001. Measurement of thermal conductivity, thermal diffusivity and heat capacity of highly porous building materials using transient plane source technique. International Communications in Heat and Mass Transfer 28, 1065–1078. doi: 10.1016/S0735-1933(01)00310-4.

Breshears, D.D., Ludwig, J.A., 2010. Near-ground solar radiation along the grassland–forest continuum: tall-tree canopy architecture imposes only muted trends and heterogeneity. Austral Ecology 35, 31–40. doi: 10.1111/j.1442-9993.2009.02009.x.

Brito, P., Lorenzo, J.R., González-Rodríguez, Á.M., Morales, D., Wieser, G., Jiménez, M.S., 2015. Canopy transpiration of a semi arid Pinus canariensis forest at a

treeline ecotone in two hydrologically contrasting years. Agricultural and Forest Meteorology 201, 120–127. doi: 10.1016/j.agrformet.2014.11.008.

Brooks, S.P., Gelman, A., 1998. General methods for monitoring convergence of iterative simulations. Journal of Computational and Graphical Statistics 7, 434–455.

Bryant, W., 2000. Fault number 21, Almanor fault zone. Quaternary Fault and Fold Database of the United States: U.S. Geological Survey Website. URL: https://earthquakes.usgs.gov/hazards/qfaults. (accessed 25 September 2020).

Burgess, S., Bleby, T., 2006. Redistribution of soil water by lateral roots mediated by stem tissues. Journal of Experimental Botany 57, 3283–3291. doi: 10.1093/jxb/erl085.

Burgess, S.S., Adams, M.A., Turner, N.C., Beverly, C.R., Ong, C.K., Khan, A.A., Bleby, T.M., 2001. An improved heat pulse method to measure low and reverse rates of sap flow in woody plants. Tree Physiology 21, 589–598. doi: 10.1093/treephys/21.9.589.

Castelli, R.M., Chambers, J.C., Tausch, R.J., 2000. Soil-plant relations along a soil-water gradient in Great Basin riparian meadows. Wetlands 20, 251–266. doi: 10.1672/0277-5212(2000)020[0251:SPRAAS]2.0.CO;2.

Čermák, J., Kučera, J., Bauerle, W.L., Phillips, N., Hinckley, T.M., 2007. Tree water storage and its diurnal dynamics related to sap flow and changes in stem volume in old-growth Douglas-fir trees. Tree Physiology 27, 181–198. doi: 10.1093/treephys/27.2.181.

Čermák, J., Kučera, J., Nadezhdina, N., 2004. Sap flow measurements with some thermodynamic methods, flow integration within trees and scaling up from sample trees to entire forest stands. Trees 18, 529–546.

Closs, R., 1958. The heat pulse method for measuring rate of sap flow in a plant stem. New Zealand Journal of Science 1, 281–288.

Cochran, P., 1972. Tolerance of lodgepole and ponderosa pine seeds and seedling to high water tables. Northwest Science 46, 322–331.

Cohen, Y., Fuchs, M., Green, G., 1981. Improvement of the heat pulse method for determining sap flow in trees. Plant, Cell & Environment 4, 391–397.

Cooper, A.E., Kirchner, J.W., Wolf, S., Lombardozzi, D.L., Sullivan, B.W., Tyler, S.W., Harpold, A.A., 2020. Snowmelt causes different limitations on transpiration in a Sierra Nevada conifer forest. Agricultural and Forest Meteorology 291, 108089. doi: 10.1016/j.agrformet.2020.108089.

Cooper, D.J., Lundquist, J.D., King, J., Flint, A., Flint, L., Wolf, E., Lott, F.C., Roche, J., 2006. Effects of the Tioga Road on Hydrologic Processes and Lodgepole Pine Invasion into Tuolumne Meadows, Yosemite National Park. Report prepared for Yosemite National Park.

Dailey, M.M., 2007. Meadow classification in the Willamette National Forest and conifer encroachment patterns in the Chucksney-Grasshopper meadow complex, western Cascade Range, Oregon. Master's thesis. Oregon State University. Corvallis, OR, USA.

Dang, Q.L., Margolis, H.A., Coyea, M.R., Sy, M., Collatz, G.J., 1997. Regulation of branch-level gas exchange of boreal trees: roles of shoot water potential and vapor pressure difference. Tree Physiology 17, 521–535. doi: 10.1093/treephys/17.8-9.521.

D'Antonio, C.M., Berlow, E.L., Haubensak, K.L., 2002. Invasive exotic plant species in Sierra Nevada ecosystems, in: Murphy, D.D., Stine, P.A. (Eds.), Proceedings of the Sierra Nevada Science Symposium; USDA Forest Service Gen. Tech. Rep.

PSW-GTR-193, USDA Forest Service Pacific Southwest Research Station, Kings Beach, CA, USA. pp. 175–184.

Dawson, T.E., Burgess, S.S., Tu, K.P., Oliveira, R.S., Santiago, L.S., Fisher, J.B., Simonin, K.A., Ambrose, A.R., 2007. Nighttime transpiration in woody plants from contrasting ecosystems. Tree Physiology 27, 561–575. doi: doi.org/10.1093/treephys/27.4.561.

Domec, J.C., Gartner, B.L., 2002. How do water transport and water storage differ in coniferous earlywood and latewood? Journal of Experimental Botany 53, 2369–2379. doi: doi.org/10.1093/jxb/erf100.

Dragoni, D., Caylor, K., Schmid, H., 2009. Decoupling structural and environmental determinants of sap velocity: Part II. Observational application. Agricultural and Forest Meteorology 149, 570–581. doi: 10.1016/j.agrformet.2008.10.010.

Dunlap, F., 1912. The Specific Heat of Wood. USDA Forest Service Bulletin 110. Washington, DC, USA.

Dunne, T., Leopold, L.B., 1998. Water in Environmental Planning. 15 ed., Freeman and Company Publishers, New York, NY, USA.

Dwire, K.A., Kauffman, J.B., Baham, J.E., 2006. Plant species distribution in relation to water-table depth and soil redox potential in montane riparian meadows. Wetlands 26, 131–146. doi: 10.1672/0277-5212(2006)26[131:PSDIRT]2.0.CO;2.

Dwire, K.A., Kauffman, J.B., Brookshire, E.J., Baham, J.E., 2004. Plant biomass and species composition along an environmental gradient in montane riparian meadows. Oecologia 139, 309–317. doi: 10.1007/s00442-004-1498-2.

Dyer, J.M., Moffett, K.E., 1999. Meadow invasion from high-elevation spruce-fir forest in south-central New Mexico. The Southwestern Naturalist 44, 444–456. doi: 10.2307/3672342.

Edwards, W., Warwick, N., 1984. Transpiration from a kiwifruit vine as estimated by the heat pulse technique and the Penman-Monteith equation. New Zealand Journal of Agricultural Research 27, 537–543. doi: 10.1080/00288233.1984.10418016.

Feddes, R.A., Kowalik, P., Kolinska-Malinka, K., Zaradny, H., 1976. Simulation of field water uptake by plants using a soil water dependent root extraction function. Journal of Hydrology 31, 13–26.

Fernández, E., 2017. Methods to estimate sap flow. ISHS Working Group on Sap Flow.

Fie, N., 2018. Hydrologic response from conifer removal and upslope forest harvest from an encroached montane meadow. Master's thesis. California Polytechnic State University. San Luis Obispo, CA, USA.

Fisher, J.B., Baldocchi, D.D., Misson, L., Dawson, T.E., Goldstein, A.H., 2007. What the towers don't see at night: nocturnal sap flow in trees and shrubs at two AmeriFlux sites in California. Tree Physiology 27, 597–610. doi: 10.1093/treephys/27.4.597.

Fites-Kaufman, J.A., Rundel, P., Stephenson, N., Weixelman, D.A., 2007. Montane and subalpine vegetation of the Sierra Nevada and Cascade ranges, in: Barbour, M., Keeler-Wolf, T., Schoenherr, A. (Eds.), Terrestrial Vegetation of California. University of California Press, Berkeley, CA, USA, pp. 456–501.

Ford, C.R., Goranson, C.E., Mitchell, R.J., Will, R.E., Teskey, R.O., 2005. Modeling canopy transpiration using time series analysis: a case study illustrating the effect

of soil moisture deficit on Pinus taeda. Agricultural and Forest Meteorology 130, 163–175. doi: 10.1016/j.agrformet.2005.03.004.

Ford, C.R., Hubbard, R.M., Kloeppel, B.D., Vose, J.M., 2007. A comparison of sap flux-based evapotranspiration estimates with catchment-scale water balance. Agricultural and Forest Meteorology 145, 176–185. doi: 10.1016/j.agrformet.2007.04.010.

Ford, C.R., McGuire, M.A., Mitchell, R.J., Teskey, R.O., 2004. Assessing variation in the radial profile of sap flux density in Pinus species and its effect on daily water use. Tree Physiology 24, 241–249. doi: 10.1093/treephys/24.3.241.

Forster, M.A., 2014. How significant is nocturnal sap flow? Tree Physiology 34, 757–765. doi: 10.1093/treephys/tpu051.

Forster, M.A., 2017. How reliable are heat pulse velocity methods for estimating tree transpiration? Forests 8, 350. doi: 10.3390/f8090350.

Gelman, A., Rubin, D.B., 1992. Inference from iterative simulation using multiple sequences. Statistical science 7, 457–472.

Goulden, M., Anderson, R., Bales, R., Kelly, A., Meadows, M., Winston, G., 2012. Evapotranspiration along an elevation gradient in California's Sierra Nevada. Journal of Geophysical Research: Biogeosciences 117. doi: 10.1029/2012JG002027.

Granier, A., Biron, P., Köstner, B., Gay, L., Najjar, G., 1996. Comparisons of xylem sap flow and water vapour flux at the stand level and derivation of canopy conductance for Scots pine. Theoretical and Applied Climatology 53, 115–122.

Green, S., Clothier, B., Jardine, B., 2003. Theory and practical application of heat pulse to measure sap flow. Agronomy Journal 95, 1371–1379. doi: 10.2134/agronj2003.1371.

Griffiths, R., Madritch, M., Swanson, A., 2005. Conifer invasion of forest meadows transforms soil characteristics in the Pacific Northwest. Forest Ecology and Management 208, 347–358. doi: 10.1016/j.foreco.2005.01.015.

Gross, S., Coppoletta, M., 2013. Historic Range of Variability for Meadows in the Sierra Nevada and South Cascades. Ecology Program Reports. USDA Forest Service Pacific Southwest Region. Davis, CA, USA.

Guyot, A., Fan, J., Oestergaard, K.T., Whitley, R., Gibbes, B., Arsac, M., Lockington, D.A., 2017. Soil-water content characterisation in a modified Jarvis-Stewart model: a case study of a conifer forest on a shallow unconfined aquifer. Journal of Hydrology 544, 242–253. doi: 10.1016/j.jhydrol.2016.11.041.

Hadley, K.S., 1999. Forest history and meadow invasion at the Rigdon Meadows archaeological site, western Cascades, Oregon. Physical Geography 20, 116–133.

Hammersmark, C.T., Dobrowski, S.Z., Rains, M.C., Mount, J.F., 2010. Simulated effects of stream restoration on the distribution of wet-meadow vegetation. Restoration Ecology 18, 882–893. doi: 10.1111/j.1526-100X.2009.00519.x.

Hammersmark, C.T., Rains, M.C., Mount, J.F., 2008. Quantifying the hydrological effects of stream restoration in a montane meadow, northern California, USA. River Research and Applications 24, 735–753. doi: 10.1002/rra.1077.

Hammersmark, C.T., Rains, M.C., Wickland, A.C., Mount, J.F., 2009. Vegetation and water-table relationships in a hydrologically restored riparian meadow. Wetlands 29, 785–797. doi: 10.1672/08-15.1.

Harpold, A.A., 2016. Diverging sensitivity of soil water stress to changing snowmelt timing in the western US. Advances in Water Resources 92, 116–129. doi: 10.1016/j.advwatres.2016.03.017.

Hatton, T., Catchpole, E., Vertessy, R., 1990. Integration of sapflow velocity to estimate plant water use. Tree Physiology 6, 201–209. doi: 10.1093/treephys/6.2.201.

Hatton, T.J., Moore, S.J., Reece, P.H., 1995. Estimating stand transpiration in a Eucalyptus populnea woodland with the heat pulse method: measurement errors and sampling strategies. Tree Physiology 15, 219–227. doi: 10.1093/treephys/15.4.219.

Hauptfeld, R., Kershner, J., Feifel, K., 2014. Sierra Nevada Ecosystem Vulnerability Assessment Technical Synthesis: Wet Meadows, in: Kershner, J. (Ed.), A Climate Change Vulnerability Assessment for Focal Resources of the Sierra Nevada. EcoAdapt, Bainbridge Island, WA. Version 1.0.

Helms, J.A., 1987. Invasion of Pinus contorta var. murrayana (Pinaceae) into mountain meadows at Yosemite National Park, California. Madrono 34, 91–97.

Hickman, J.C., 1976. Non-forest vegetation of the central western Cascade Mountains of Oregon. Northwest Science 50, 145–155.

Hill, B., Mitchell-Bruker, S., 2010. Comment on "A framework for understanding the hydroecology of impacted wet meadows in the Sierra Nevada and Cascade Ranges, California, USA": paper published in Hydrogeology Journal (2009) 17: 229–246, by Steven P. Loheide II, Richard S. Deitchman, David J. Cooper, Evan C. Wolf, Christopher T. Hammersmark, Jessica D. Lundquist. Hydrogeology Journal 18, 1741–1743. doi: 10.1007/s10040-010-0634-9.

Huber, B., 1932. Beobachtung und messung pflanzlicher saftstrome. Ber. deutsch. Bot. Ges. 50, 89–109.

Jarvis, P., 1976. The interpretation of the variations in leaf water potential and stomatal conductance found in canopies in the field. Philosophical Transactions of

the Royal Society of London. B, Biological Sciences 273, 593–610. doi: 10.1098/rstb.1976.0035.

Jepsen, S.M., Harmon, T.C., Guan, B., 2021. Analyzing the suitability of remotely sensed ET for calibrating a watershed model of a Mediterranean montane forest. Remote Sensing 13, 1258. doi: 10.3390/rs13071258.

Jung, E.Y., Otieno, D., Lee, B., Lim, J.H., Kang, S., Schmidt, M., Tenhunen, J., 2011. Up-scaling to stand transpiration of an Asian temperate mixed-deciduous forest from single tree sapflow measurements. Plant Ecology 212, 383–395. doi: 10.1007/s11258-010-9829-3.

Koch, P., 1987. Gross Characteristics of Lodgepole Pine Trees in North America. Technical Report INT-227. USDA Forest Service, Intermountain Research Station. Ogden, UT, USA.

Köstner, B., Granier, A., Cermák, J., 1998. Sapflow measurements in forest stands: methods and uncertainties. Annales des sciences forestières 55, 13–27. doi: 10.1051/forest:19980102.

Kumagai, T., Aoki, S., Nagasawa, H., Mabuchi, T., Kubota, K., Inoue, S., Utsumi, Y., Otsuki, K., 2005a. Effects of tree-to-tree and radial variations on sap flow estimates of transpiration in Japanese cedar. Agricultural and Forest Meteorology 135, 110–116. doi: 10.1016/j.agrformet.2005.11.007.

Kumagai, T., Aoki, S., Otsuki, K., Utsumi, Y., 2009. Impact of stem water storage on diurnal estimates of whole-tree transpiration and canopy conductance from sap flow measurements in japanese cedar and japanese cypress trees. Hydrological Processes: An International Journal 23, 2335–2344.

Kumagai, T., Nagasawa, H., Mabuchi, T., Ohsaki, S., Kubota, K., Kogi, K., Utsumi, Y., Koga, S., Otsuki, K., 2005b. Sources of error in estimating stand transpiration

using allometric relationships between stem diameter and sapwood area for Cryptomeria japonica and Chamaecyparis obtusa. Forest Ecology and Management 206, 191–195. doi: 10.1016/j.foreco.2004.10.066.

Kumagai, T., Tateishi, M., Shimizu, T., Otsuki, K., 2008. Transpiration and canopy conductance at two slope positions in a Japanese cedar forest watershed. Agricultural and Forest Meteorology 148, 1444–1455. doi: 10.1016/j.agrformet.2008.04.010.

Kume, T., Tsuruta, K., Komatsu, H., Kumagai, T., Higashi, N., Shinohara, Y., Otsuki, K., 2010. Effects of sample size on sap flux-based stand-scale transpiration estimates. Tree Physiology 30, 129–138. doi: 10.1093/treephys/tpp074.

Laloy, E., Vrugt, J.A., 2012. High-dimensional posterior exploration of hydrologic models using multiple-try DREAM (ZS) and high-performance computing. Water Resources Research 48. doi: 10.1029/2011WR010608.

Lang, N.L., Halpern, C.B., 2007. The soil seed bank of a montane meadow: consequences of conifer encroachment and implications for restoration. Botany 85, 557–569. doi: 10.1139/B07-051.

Larsen, E.K., Palau, J.L., Valiente, J.A., Chirino, E., Bellot, J., 2020. Long-term probe misalignment and proposed quality control using the heat pulse method for transpiration estimations. Hydrology and Earth System Sciences 24, 2755–2767. doi: 10.5194/hess-24-2755-2020.

Lesh, M.W., 2010. Evaluation of lodgepole pine tree removal on the storage potential of a shallow aquifer in a Sierra Nevada mountain meadow. Master's thesis. California State University Sacramento. Sacramento, CA, USA.

Lindquist, S., Wilcox, J., 2000. New concepts for meadow restoration in the northern Sierra Nevada. Feather River Coordinated Resource Management Group.

Link, P., Simonin, K., Maness, H., Oshun, J., Dawson, T., Fung, I., 2014. Species differences in the seasonality of evergreen tree transpiration in a Mediterranean climate: analysis of multiyear, half-hourly sap flow observations. Water Resources Research 50, 1869–1894. doi: 10.1002/2013WR014023.

Litvak, M.E., Schwinning, S., Heilman, J.L., 2010. Woody plant rooting depth and ecosystem function of savannas: a case study from the Edwards Plateau Karst, Texas, in: Hill, M., Hanan, N. (Eds.), Ecosystem Function in Global Savannas: Measurement and Modeling at Landscape to Global Scales. CRC Press, Boca Raton, FL, USA, pp. 117–134.

Liu, X., Biondi, F., 2020. Transpiration drivers of high-elevation five-needle pines (Pinus longaeva and Pinus flexilis) in sky-island ecosystems of the North American Great Basin. Science of The Total Environment 739, 139861. doi: 10.1016/j.scitotenv.2020.139861.

Lohammar, T., Larsson, S., Linder, S., Falk, S., 1980. FAST: Simulation models of gaseous exchange in Scots pine. Ecological Bulletins , 505–523.

Loheide, S.P., Butler Jr, J.J., Gorelick, S.M., 2005. Estimation of groundwater consumption by phreatophytes using diurnal water table fluctuations: a saturated-unsaturated flow assessment. Water Resources Research 41, 1–14. doi: 10.1029/2005WR003942.

Loheide, S.P., Deitchman, R.S., Cooper, D.J., Wolf, E.C., Hammersmark, C.T., Lundquist, J.D., 2009. A framework for understanding the hydroecology of impacted wet meadows in the Sierra Nevada and Cascade Ranges, California, USA. Hydrogeology Journal 17, 229–246. doi: 10.1007/s10040-008-0380-4.

Loheide, S.P., Gorelick, S.M., 2007. Riparian hydroecology: a coupled model of the observed interactions between groundwater flow and meadow vegetation patterning. Water Resources Research 43. doi: 10.1029/2006WR005233.

Loheide II, S.P., Gorelick, S.M., 2005. A local-scale, high-resolution evapotranspiration mapping algorithm (ETMA) with hydroecological applications at riparian meadow restoration sites. Remote Sensing of Environment 98, 182–200. doi: 10.1016/j.rse.2005.07.003.

Looker, N., Martin, J., Hoylman, Z., Jencso, K., Hu, J., 2018. Diurnal and seasonal coupling of conifer sap flow and vapour pressure deficit across topoclimatic gradients in a subalpine catchment. Ecohydrology 11, e1994. doi: 10.1002/eco.1994.

Looker, N., Martin, J., Jencso, K., Hu, J., 2016. Contribution of sapwood traits to uncertainty in conifer sap flow as estimated with the heat-ratio method. Agricultural and Forest Meteorology 223, 60–71. doi: 10.1016/j.agrformet.2016.03.014.

López-Bernal, Á., Testi, L., Villalobos, F.J., 2012. Using the compensated heat pulse method to monitor trends in stem water content in standing trees. Tree Physiology 32, 1420–1429. doi: 10.1093/treephys/tps101.

Loranty, M.M., Mackay, D.S., Ewers, B.E., Adelman, J.D., Kruger, E.L., 2008. Environmental drivers of spatial variation in whole-tree transpiration in an aspen-dominated upland-to-wetland forest gradient. Water Resources Research 44. doi: 10.1029/2007WR006272.

Lotan, J.E., Critchfield, W.B., 1990. Pinus contorta dougl. ex. loud. lodgepole pine, in: Burns, R.M., Honkala, B.H. (Eds.), Silvics of North America 1, Conifers. Washington, DC, USA. Agriculture Handbook 654, pp. 302–315.

Loustau, D., Berbigier, P., Roumagnac, P., Arruda-Pacheco, C., David, J., Ferreira, M., Pereira, J., Tavares, R., 1996. Transpiration of a 64-year-old maritime pine stand in portugal. Oecologia 107, 33–42.

Lowry, C.S., Loheide, S.P., Moore, C.E., Lundquist, J.D., 2011. Groundwater controls on vegetation composition and patterning in mountain meadows. Water Resources Research 47. doi: 10.1029/2010WR010086.

Lubetkin, K.C., Westerling, A.L., Kueppers, L.M., 2017. Climate and landscape drive the pace and pattern of conifer encroachment into subalpine meadows. Ecological Applications 27, 1876–1887. doi: 10.1002/eap.1574.

Lucas, R.G., 2016. Evapotranspiration and Groundwater Patterns in Montane Meadows of the Sierra Nevada, CA. Ph.D. thesis. UC Merced. Merced, CA, USA.

Macdonald, G., Gay, T., 1966. Geology of the southern Cascade Range, Modoc Plateau, and Great Basin Areas in Northeastern California, in: Mineral and Water Resources of California. United States Geologic Survey, California Division of Mines and Geology, and United States Bureau of Mines, San Francisco, CA, pp. 43–48.

Mackay, D.S., Ewers, B.E., Loranty, M.M., Kruger, E.L., 2010. On the representativeness of plot size and location for scaling transpiration from trees to a stand. Journal of Geophysical Research: Biogeosciences 115. doi: 10.1029/2009JG001092.

Mark, W.R., Crews, D.L., 1973. Heat-pulse velocity and bordered pit condition in living Engelmann spruce and lodgepole pine trees. Forest Science 19, 291–296.

Markstrom, D.C., Hann, R.A., 1972. Seasonal Variation in Wood Permeability and Stem Moisture Content of Three Rocky Mountain Softwoods. Reseach Note RM-212. USDA Forest Service, Rocky Mountain Forest and Range Research Station.

Marshall, D., 1958. Measurement of sap flow in conifers by heat transport. Plant Physiology 33, 385.

McDowell, N.G., White, S., Pockman, W.T., 2008. Transpiration and stomatal conductance across a steep climate gradient in the southern Rocky Mountains. Ecohydrology 1, 193–204. doi: 10.1002/eco.20.

Meinzer, F.C., Bond, B.J., Warren, J.M., Woodruff, D.R., 2005. Does water transport scale universally with tree size? Functional Ecology 19, 558–565. doi: 10.1111/j.1365-2435.2005.01017.x.

Menne, M.J., Durre, I., Vose, R.S., Gleason, B.E., Houston, T.G., 2012. An overview of the global historical climatology network-daily database. Journal of Atmospheric and Oceanic Technology 29, 897==910. doi: 10.1175/JTECH-D-11-00103.1.

Millar, C.I., Westfall, R.D., Delany, D.L., King, J.C., Graumlich, L.J., 2004. Response of subalpine conifers in the Sierra Nevada, California, USA, to 20th-century warming and decadal climate variability. Arctic, Antarctic, and Alpine Research 36, 181–200. doi: 10.1657/1523-0430(2004)036[0181:ROSCIT]2.0.CO;2.

Miller, E.A., Halpern, C.B., 1998. Effects of environment and grazing disturbance on tree establishment in meadows of the central Cascade Range, Oregon, USA. Journal of Vegetation Science 9, 265–282. doi: 10.2307/3237126.

Minore, D., 1970. Seedling growth of eight northwestern tree species over three water tables. Technical Report PNW-115. USDA Forest Service, Pacific Northwest Forest and Range Experiment Station. Portland, OR, USA.

Mitsch, W.J., Gosselink, J.G., 2000. The value of wetlands: importance of scale and landscape setting. Ecological Economics 35, 25–33. doi: 10.1016/S0921-8009(00)00165-8.

Moore, G.W., Barre, D.A., Owens, M.K., 2012. Does shrub removal increase groundwater recharge in southwestern Texas semiarid rangelands? Rangeland Ecology & Management 65, 1–10. doi: 10.2111/REM-D-11-00055.1.

Moore, G.W., Bond, B.J., Jones, J.A., Phillips, N., Meinzer, F.C., 2004. Structural and compositional controls on transpiration in 40-and 450-year-old riparian forests in western oregon, usa. Tree Physiology 24, 481–491. doi: 10.1093/treephys/24.5.481.

Moore, G.W., Heilman, J.L., 2011. Proposed principles governing how vegetation changes affect transpiration. Ecohydrology 4, 351–358. doi: 10.1002/eco.232.

Moore, M.M., Huffman, D.W., 2004. Tree encroachment on meadows of the north rim, Grand Canyon National Park, Arizona, USA. Arctic, Antarctic, and Alpine Research 36, 474–483. doi: 10.1657/1523-0430(2004)036[0474:TEOMOT]2.0.CO;2.

Mote, P.W., Li, S., Lettenmaier, D.P., Xiao, M., Engel, R., 2018. Dramatic declines in snowpack in the western US. npj Climate and Atmospheric Science 1, 1–6. doi: 10.1038/s41612-018-0012-1.

Musselman, K.N., Clark, M.P., Liu, C., Ikeda, K., Rasmussen, R., 2017. Slower snowmelt in a warmer world. Nature Climate Change 7, 214–219. doi: 10.1038/nclimate3225.

Nadezhdina, N., Steppe, K., De Pauw, D.J., Bequet, R., Čermak, J., Ceulemans, R., 2009. Stem-mediated hydraulic redistribution in large roots on opposing sides of a Douglas-fir tree following localized irrigation. New Phytologist 184, 932–943. doi: 10.1111/j.1469-8137.2009.03024.x.

Norman, S.P., Taylor, A.H., 2005. Pine forest expansion along a forest-meadow ecotone in northeastern California, USA. Forest Ecology and Management 215, 51–68. doi: 10.1016/j.foreco.2005.05.003.

Norton, J.B., Jungst, L.J., Norton, U., Olsen, H.R., Tate, K.W., Horwath, W.R., 2011. Soil carbon and nitrogen storage in upper montane riparian meadows. Ecosystems 14, 1217–1231. doi: 10.1007/s10021-011-9477-z.

Oren, R., Ewers, B.E., Todd, P., Phillips, N., Katul, G., 1998a. Water balance delineates the soil layer in which moisture affects canopy conductance. Ecological Applications 8, 990–1002. doi: 10.1890/1051-0761(1998)008[0990:WBDTSL]2.0.CO;2.

Oren, R., Phillips, N., Katul, G., Ewers, B.E., Pataki, D.E., 1998b. Scaling xylem sap flux and soil water balance and calculating variance: a method for partitioning water flux in forests. Annales des Sciences Forestieres 55, 191–216. doi: 10.1051/forest:19980112.

Oren, R., Sperry, J., Katul, G., Pataki, D., Ewers, B., Phillips, N., Schäfer, K., 1999. Survey and synthesis of intra-and interspecific variation in stomatal sensitivity to vapour pressure deficit. Plant, Cell & Environment 22, 1515–1526. doi: 10.1046/j.1365-3040.1999.00513.x.

Parker, A.J., 1991. Forest/environment relationships in Lassen Volcanic National Park, California, USA. Journal of Biogeography 18, 543–552. doi: 10.2307/2845690.

Pataki, D.E., Oren, R., Smith, W.K., 2000. Sap flux of co-occurring species in a western subalpine forest during seasonal soil drought. Ecology 81, 2557–2566. doi: 10.1890/0012-9658(2000)081[2557:SFOCOS]2.0.CO;2.

Pausch, R.C., Grote, E.E., Dawson, T.E., 2000. Estimating water use by sugar maple trees: considerations when using heat-pulse methods in trees with deep functional sapwood. Tree Physiology 20, 217–227. doi: 10.1093/treephys/20.4.217.

Peters, R.L., Fonti, P., Frank, D.C., Poyatos, R., Pappas, C., Kahmen, A., Carraro, V., Prendin, A.L., Schneider, L., Baltzer, J.L., et al., 2018. Quantification of

uncertainties in conifer sap flow measured with the thermal dissipation method. New Phytologist 219, 1283–1299. doi: 10.1111/nph.15241.

Petrie, M., Wildeman, A., Bradford, J.B., Hubbard, R., Lauenroth, W., 2016. A review of precipitation and temperature control on seedling emergence and establishment for ponderosa and lodgepole pine forest regeneration. Forest Ecology and Management 361, 328–338. doi: 10.1016/j.foreco.2015.11.028.

Phillips, N., Oren, R., Zimmermann, R., 1996. Radial patterns of xylem sap flow in non-, diffuse-and ring-porous tree species. Plant, Cell, & Environment 19, 983–990. doi: 10.1111/j.1365-3040.1996.tb00463.x.

Phillips, N.G., Ryan, M.G., Bond, B.J., McDowell, N.G., Hinckley, T.M., Čermák, J., 2003. Reliance on stored water increases with tree size in three species in the Pacific Northwest. Tree Physiology 23, 237–245. doi: 10.1093/treephys/23.4.237.

Porporato, A., D'odorico, P., Laio, F., Ridolfi, L., Rodriguez-Iturbe, I., 2002. Ecohydrology of water-controlled ecosystems. Advances in Water Resources 25, 1335–1348. doi: 10.1016/S0309-1708(02)00058-1.

Quiñonez-Piñón, M.R., Valeo, C., 2017. Allometry of sapwood depth in five boreal trees. Forests 8, 457. doi: 10.3390/f8110457.

Ratliff, R.D., 1985. Meadows in the Sierra Nevada of California: State of Knowledge. Technical Report PSW-84. USDA Forest Service, Pacific Southwest Forest and Range Experiment Station. Berkeley, CA, USA.

Raz-Yaseef, N., Rotenberg, E., Yakir, D., 2010. Effects of spatial variations in soil evaporation caused by tree shading on water flux partitioning in a semi-arid pine forest. Agricultural and Forest Meteorology 150, 454–462. doi: 10.1016/j.agrformet.2010.01.010.

Reich, K., Berg, N., Walton, D., Schwartz, M., Sun, F., Huang, X., Hall, A., 2018. Climate Change in the Sierra Nevada: California's Water Future. UCLA Center for Climate Science.

Rice, J.M., Halpern, C.B., Antos, J.A., Jones, J.A., 2012. Spatio-temporal patterns of tree establishment are indicative of biotic interactions during early invasion of a montane meadow. Plant Ecology 213, 555–568. doi: 10.1007/s11258-012-0021-9.

Roderick, M.L., Berry, S.L., 2001. Linking wood density with tree growth and environment: a theoretical analysis based on the motion of water. New Phytologist 149, 473–485. doi: 10.1046/j.1469-8137.2001.00054.x.

Royce, E.B., Barbour, M.G., 2001. Mediterranean climate effects. I. Conifer water use across a Sierra Nevada ecotone. American Journal of Botany 88, 911–918. doi: 10.2307/2657044.

Running, S.W., Mu, Q., Zhao, M., Moreno, A., 2019a. MOD16A2GF MODIS/Terra Net Evapotranspiration Gap-Filled 8-Day L4 Global 500 m SIN Grid V006. URL: https://doi.org/10.5067/MODIS/MOD16A2GF.00. (accessed 11 June 2021).

Running, S.W., Mu, Q., Zhao, M., Moreno, A., 2019b. User's Guide MODIS Global Terrestrial Evapotranspiration (ET) Product (MOD16A2/A3 and Year-End Gap-Filled MOD16A2GF/A3GF) NASA Earth Observing System MODIS Land Algorithm (For Collection 6). 2.2 ed. National Aeronautics and Space Administration. Washington, DC, USA.

Sanford, T.W., 2016. The water table and soil moisture response following the removal of conifers from an encroached meadow. Master's thesis. California Polytechnic State University. San Luis Obispo, CA, USA.

Schenk, H.J., Jackson, R.B., 2002. The global biogeography of roots. Ecological Monographs 72, 311–328. doi: 10.1890/0012-9615(2002)072[0311:TGBOR]2.0.CO;2.

Schlesinger, W.H., Jasechko, S., 2014. Transpiration in the global water cycle. Agricultural and Forest Meteorology 189, 115–117. doi: 10.1016/j.agrformet.2014.01.011.

Schoups, G., Vrugt, J.A., 2010. A formal likelihood function for parameter and predictive inference of hydrologic models with correlated, heteroscedastic, and non-Gaussian errors. Water Resources Research 46. doi: 10.1029/2009WR008933.

Shinohara, Y., Tsuruta, K., Ogura, A., Noto, F., Komatsu, H., Otsuki, K., Maruyama, T., 2013. Azimuthal and radial variations in sap flux density and effects on stand-scale transpiration estimates in a japanese cedar forest. Tree physiology 33, 550–558.

Smith, D., Allen, S., 1996. Measurement of sap flow in plant stems. Journal of Experimental Botany 47, 1833–1844.

Soil Survey Staff, 2020. Web soil survey. URL: http://websoilsurvey.sc.egov.usda.gov/. (accessed 21 September 2020).

Solum, J.R., 2020. Estimating Evapotranspiration of a Riparian Forest Using Sap Flow Measurements. Master's thesis. California Polytechnic State University. San Luis Obispo, CA, USA.

Spittlehouse, D., 2002. Sap flow in old lodgepole pine trees, in: Proc. 25th Conf. Agric. For. Meteorol, pp. 123–124.

Steinwand, A., Harrington, R., Or, D., 2006. Water balance for Great Basin phreatophytes derived from eddy covariance, soil water, and water table measurements. Journal of Hydrology 329, 595–605. doi: 10.1016/j.jhydrol.2006.03.013.

Steppe, K., De Pauw, D.J., Doody, T.M., Teskey, R.O., 2010. A comparison of sap flux density using thermal dissipation, heat pulse velocity and heat field deformation methods. Agricultural and Forest Meteorology 150, 1046–1056. doi: 10.1016/j.agrformet.2010.04.004.

Stewart, J., 1988. Modelling surface conductance of pine forest. Agricultural and Forest Meteorology 43, 19–35. doi: 10.1016/0168-1923(88)90003-2.

Stillwater Sciences, 2012. A Guide for Restoring Functionality to Mountain Meadows of the Sierra Nevada. Technical Memorandum Prepared for American Rivers, Nevada City, CA, USA. Berkeley, CA, USA.

Surfleet, C., Fie, N., Jasbinsek, J., 2020. Hydrologic response of a montane meadow from conifer removal and upslope forest thinning. Water 12, 293. doi: 10.3390/w12010293.

Surfleet, C., Sanford, T., Van Oosbree, G., Jasbinsek, J., 2019. Hydrologic response of meadow restoration the first year following removal of encroached conifers. Water 11, 428. doi: 10.3390/w11030428.

Surfleet, C.G., Tullos, D., 2013. Variability in effect of climate change on rain-on-snow peak flow events in a temperate climate. Journal of Hydrology 479, 24–34. doi: 10.1016/j.jhydrol.2012.11.021.

Swanson, F.J., Halpern, C.B., Cissel, J.H., 2007. Restoration of Dry, Montane Meadows Through Prescribed Fire, Vegetation and Fuels Management: A Program of Research and Adaptive Management in Western Oregon. Project 01C-3-3-10. Joint Fire Science Program. Boise, ID, USA.

Swanson, R., 1983. Numerical and experimental analysis of implanted-probe heat-pulse theory. Ph.D. thesis. University of Alberta. Alberta, Canada.

Swanson, R., Whitfield, D., 1981. A numerical analysis of heat pulse velocity theory and practice. Journal of Experimental Botany 32, 221–239. doi: 10.1093/jxb/32.1.221.

Swanson, R.H., 1962. An Instrument for Detecting Sap Movement in Woody Plants. Paper 68. USDA Forest Service Rocky Mountain Forest and Range Experiment Station. Fort Collins, CO, USA.

Swanson, R.H., 1994. Significant historical developments in thermal methods for measuring sap flow in trees. Agricultural and Forest Meteorology 72, 113–132. doi: 10.1016/0168-1923(94)90094-9.

Takaoka, S., Swanson, F.J., 2008. Change in extent of meadows and shrub fields in the central western Cascade Range, Oregon. The Professional Geographer 60, 527–540. doi: 10.1080/00330120802212099.

Tateishi, M., Kumagai, T., Utsumi, Y., Umebayashi, T., Shiiba, Y., Inoue, K., Kaji, K., Cho, K., Otsuki, K., 2008. Spatial variations in xylem sap flux density in evergreen oak trees with radial-porous wood: comparisons with anatomical observations. Trees 22, 23–30. doi: 10.1007/s00468-007-0165-8.

Taylor, A.H., 1990. Tree invasion in meadows of Lassen Volcanic National Park, California. The Professional Geographer 42, 457–470. doi: 10.1111/j.0033-0124.1990.00457.x.

Taylor, A.H., 1995. Forest expansion and climate change in the mountain hemlock (Tsuga mertensiana) zone, Lassen Volcanic National Park, California, USA. Arctic and Alpine Research 27, 207–216.

Topp, G.C., Davis, J., Annan, A.P., 1980. Electromagnetic determination of soil water content: Measurements in coaxial transmission lines. Water Resources Research 16, 574–582.

Tromp-van Meerveld, H., McDonnell, J., 2006. On the interrelations between topography, soil depth, soil moisture, transpiration rates and species distribution at the hillslope scale. Advances in Water Resources 29, 293–310. doi: 10.1016/j.advwatres.2005.02.016.

Tsuruta, K., Kume, T., Komatsu, H., Higashi, N., Umebayashi, T., Kumagai, T., Otsuki, K., 2010. Azimuthal variations of sap flux density within Japanese cypress xylem trunks and their effects on tree transpiration estimates. Journal of Forest Research 15, 398–403. doi: 10.1007/s10310-010-0202-0.

Vale, T.R., 1978. Tree invasion of Cinnabar Park in Wyoming. American Midland Naturalist 100, 277–284. doi: 10.2307/2424827.

Vale, T.R., 1981. Tree invasion of montane meadows in Oregon. American Midland Naturalist 105, 61–69.

Vale, T.R., 1987. Vegetation change and park purposes in the high elevations of Yosemite National Park, California. Annals of the Association of American Geographers 77, 1–18. doi: 10.1111/j.1467-8306.1987.tb00141.x.

Van Oosbree, G.F., 2015. Hydrologic response to conifer removal from an encroached mountain meadow. Master's thesis. California Polytechnic State University. San Luis Obispo, CA, USA.

Vandegehuchte, M.W., Steppe, K., 2012. Improving sap flux density measurements by correctly determining thermal diffusivity, differentiating between bound and unbound water. Tree Physiology 32, 930–942. doi: 10.1093/treephys/tps034.

Vankat, J.L., Major, J., 1978. Vegetation changes in Sequoia National Park, California. Journal of Biogeography 5, 377–402. doi: 10.2307/3038030.

Veatch, W., Brooks, P., Gustafson, J., Molotch, N., 2009. Quantifying the effects of forest canopy cover on net snow accumulation at a continental, mid-latitude site. Ecohydrology 2, 115–128. doi: 10.1002/eco.45.

Vergeynst, L.L., Vandegehuchte, M.W., McGuire, M.A., Teskey, R.O., Steppe, K., 2014. Changes in stem water content influence sap flux density measurements with thermal dissipation probes. Trees 28, 949–955. doi: 10.1007/s00468-014-0989-y.

Vertessy, R., Benyon, R., O'sullivan, S., Gribben, P., 1995. Relationships between stem diameter, sapwood area, leaf area and transpiration in a young mountain ash forest. Tree Physiology 15, 559–567. doi: 10.1093/treephys/15.9.559.

Vertessy, R.A., Watson, F.G., Sharon, K., et al., 2001. Factors determining relations between stand age and catchment water balance in mountain ash forests. Forest Ecology and Management 143, 13–26. doi: 10.1016/S0378-1127(00)00501-6.

Viers, J.H., Purdy, S.E., Peek, R.A., Fryjoff-Hung, A., Santos, N.R., Katz, J.V., Emmons, J.D., Dolan, D.V., Yarnell, S.M., 2013. Montane Meadows in The Sierra Nevada: Changing Hydroclimatic Conditions and Concepts for Vulnerability Assessment. Technical Report CWS-2013-01. University of California Davis. Davis, CA, USA.

Vinukollu, R.K., Wood, E.F., Ferguson, C.R., Fisher, J.B., 2011. Global estimates of evapotranspiration for climate studies using multi-sensor remote sensing data: evaluation of three process-based approaches. Remote Sensing of Environment 115, 801–823. doi: 10.1016/j.rse.2010.11.006.

Vrugt, J.A., 2016. Markov chain monte carlo simulation using the DREAM software package: Theory, concepts, and MATLAB implementation. Environmental Modelling & Software 75, 273–316. doi: 10.1016/j.envsoft.2015.08.013.

Wang, H., Guan, H., Liu, N., Soulsby, C., Tetzlaff, D., Zhang, X., 2020. Improving the Jarvis-type model with modified temperature and radiation functions for sap flow simulations. Journal of Hydrology 587, 124981. doi: 10.1016/j.jhydrol.2020.124981.

Wang, H., Guan, H., Simmons, C.T., 2016. Modeling the environmental controls on tree water use at different temporal scales. Agricultural and Forest Meteorology 225, 24–35. doi: 10.1016/j.agrformet.2016.04.016.

Ward, A.D., Trimble, S.W., 2016. Environmental Hydrology. Third ed., CRC Press.

Waring, R.H., Running, S.W., 1978. Sapwood water storage: its contribution to transpiration and effect upon water conductance through the stems of old-growth douglas-fir. Plant, Cell & Environment 1, 131–140.

Weixelman, D.A., Hill, B., Cooper, D., Berlow, E., Viers, J., Purdy, S., Merrill, A., Gross, S., 2011. A Field Key to Meadow Hydrogeomorphic Types for the Sierra Nevada and Southern Cascade Ranges in California. Technical Report R5-TP-034. USDA Forest Service Pacific Southwest Region. Vallejo, CA, USA.

Whitley, R., Medlyn, B., Zeppel, M., Macinnis-Ng, C., Eamus, D., 2009. Comparing the Penman–Monteith equation and a modified Jarvis–Stewart model with an artificial neural network to estimate stand-scale transpiration and canopy conductance. Journal of Hydrology 373, 256–266. doi: 10.1016/j.jhydrol.2009.04.036.

Whitley, R., Taylor, D., Macinnis-Ng, C., Zeppel, M., Yunusa, I., O'Grady, A., Froend, R., Medlyn, B., Eamus, D., 2013. Developing an empirical model of canopy water flux describing the common response of transpiration to solar radiation and

VPD across five contrasting woodlands and forests. Hydrological Processes 27, 1133–1146. doi: 10.1002/hyp.9280.

Williams, D., Cable, W., Hultine, K., Hoedjes, J., Yepez, E., Simonneaux, V., Er-Raki, S., Boulet, G., De Bruin, H., Chehbouni, A., et al., 2004. Evapotranspiration components determined by stable isotope, sap flow and eddy covariance techniques. Agricultural and Forest Meteorology 125, 241–258. doi: 10.1016/j.agrformet.2004.04.008.

Wilson, K.B., Hanson, P.J., Mulholland, P.J., Baldocchi, D.D., Wullschleger, S.D., 2001. A comparison of methods for determining forest evapotranspiration and its components: sap-flow, soil water budget, eddy covariance and catchment water balance. Agricultural and Forest Meteorology 106, 153–168. doi: 10.1016/S0168-1923(00)00199-4.

Wullschleger, S.D., Hanson, P., Todd, D., 2001. Transpiration from a multi-species deciduous forest as estimated by xylem sap flow techniques. Forest Ecology and Management 143, 205–213. doi: 10.1016/S0378-1127(00)00518-1.

APPENDIX A: ROCK CREEK MEADOW PLANT SPECIES LIST

Table A.1: Rock Creek Meadow plant species list adapted from Collins Almanor Forest Timber Harvest Plan by surveyors: K. Bovee and B. Johnson.

RCM Timber Harvest Plan Plant Survey		
Trees:	*Abies concolor*	*Pinus contorta ssp. murrayana*
	Pinus lambertiana	*Populus trichocarpa*
	Pinus jeffreyi	*Populus tremuloides*
Shrubs:	*Alnus incana ssp. tenuifolia*	*Amelanchier utahensis*
	Arctostaphylos nevadensis	*Arctostaphylos patula*
	Ceanothus cordulatus	*Ceanothus integerrimus*
	Ceanothus prostratus	*Ceanothus velutinus*
	Chrysolepis sempervirens	*Cornus sericea*
	Ericameria bloomeri	*Prunus virginiana*
	Ribes roezlii	*Rosa californica*
	Rubus parviflorus	*Salix lasiandra*
	Salix lemmonii	*Spiraea douglasii*
	Symphoricarpos mollis	
Graminoids:	*Agrostis pallens*	*Anthoxanthum aristatum*
	Bromus carinatus	*Bromus racemosus*
	Carex athrostachya	*Carex davyi*
	Carex douglasii	*Carex fracta*
	Carex integra	*Carex lenticularis var. impressa*
	Carex leporinella	*Carex nebrascensis*
	Carex pellita	*Carex subfusca*
	Carex whitneyi	*Cyperus squarrosus*
	Dactylis glomerata	*Danthonia californica*

Table A.1 continued from previous page

RCM Timber Harvest Plan Plant Survey		
	Deschampsia cespitosa	*Deschampsia danthanioides*
	Eleocharis macrostachya	*Elymus elymoides*
	Festuca idahoensis	*Hordeum brachyantherum*
	Juncus acuminatus	*Juncus balticus*
	Juncus bufonius	*Juncus nevadensis*
	Luzula comosa	*Melica subulata*
	Muhlenbergia filiformis	*Poa palustris*
	Poa pratensis	*Poa secunda*
	Stipa occidentalis	
Forbs:	*Achillea millefolium*	*Mentha arvensis*
	Aquifolium repens	*Microsteris gracilis*
	Aquilegia formosa	*Mimulus primuloides*
	Arnica nevadensis	*Monardella odoratissima*
	Barbarea orthocera	*Navarretia intertexta ssp. intertexta*
	Bistorta bistortoides	*Navarretia sinistra*
	Calochortus nudus	*Osmorhiza berteroi*
	Calyptridium umbellatum	*Packera pauciflora*
	Calystegia occidentalis	*Paeonia brownii*
	Camassia quamash	*Pedicularis densiflora*
	Castilleja applegatei	*Penstemon deustus*
	Castilleja lacera	*Penstemon heterodoxus var. shastensis*
	Castilleja tenuis	*Penstemon neotericus*
	Centaurea diffusa	*Penstemon rydbergii*
	Chamaesaracha nana	*Phleum pratense*
	Chimaphila menziesii	*Plagiobothrys (cognatus)*
	Cirsium andersonii	*Plantago major*

Table A.1 continued from previous page

RCM Timber Harvest Plan Plant Survey	
Cirsium scariosum	*Platanthera dilatata var. leucostachys*
Cirsium vulgare	*Polygonum sawatchense*
Clarkia sp.	*Potentilla gracilis*
Claytonia rubra	*Potentilla millefolium*
Collomia grandiflora	*Poteridium annuum*
Collomia tinctoria	*Prunella vulgaris*
Crepis modocensis	*Pterospora andromedea*
Cryptantha intermedia	*Pyrola picta*
Cynoglossum occidentale	*Ranunculus aquatilis*
Dieteria canescens	*Ranunculus occidentalis*
Elytrigia repens	*Ranunculus orthorhynchus*
Epilobium brachycarpum	*Rumex acetosella*
Epilobium pallidum	*Sarcodes sanguinea*
Equisetum arvense	*Senecio aronicoides*
Erigeron eatonii	*Senecio triangularis*
Erigeron inornatus var. calidipetris	*Sidalcea glaucescens*
Erigeron inornatus var. inornatus	*Sidalcea oregana*
Eriogonum nudum	*Silene lemmonii*
Fragaria vesca	*Sisyrinchium idahoense*
Galium aparine	*Solidago lepida var. salebrosa*
Galium (boreale)	*Stachys rigida ssp. rigida*
Gayophytum diffusum	*Stellaria longipes*
Geum macrophyllum	*Stephanomeria lactucina*
Gnaphalium palustre	*Symphyotrichum spathulatum*
Hackelia californica	*Taraxacum officinale*
Heterocodon rariflorum	*Taraxia tanacetifolia*

Table A.1 continued from previous page

RCM Timber Harvest Plan Plant Survey	
Hieracium albiflorum	*Thalictrum fendleri*
Horkelia fusca	*Tragopogon dubius*
Hosackia oblongifolia	*Trifolium longipes ssp. hansenii*
Hypericum anagalloides	*Trifolium productum*
Hypericum perforatum	*Triteleia hyacinthina*
Hypericum scouleri	*Veratrum californicum*
Kelloggia galioides	*Verbascum thapsus*
Lactuca serriola	*Veronica peregrina ssp. xalapensis*
Leucanthemum vulgare	*Vicia americana*
Ligusticum grayi	*Viola sp.*
Lilium pardalinum	
Lupinus lepidus var. sellulus	
Lupinus polyphyllus var. burkei	
Maianthemum racemosum	
Maianthemum stellatum	

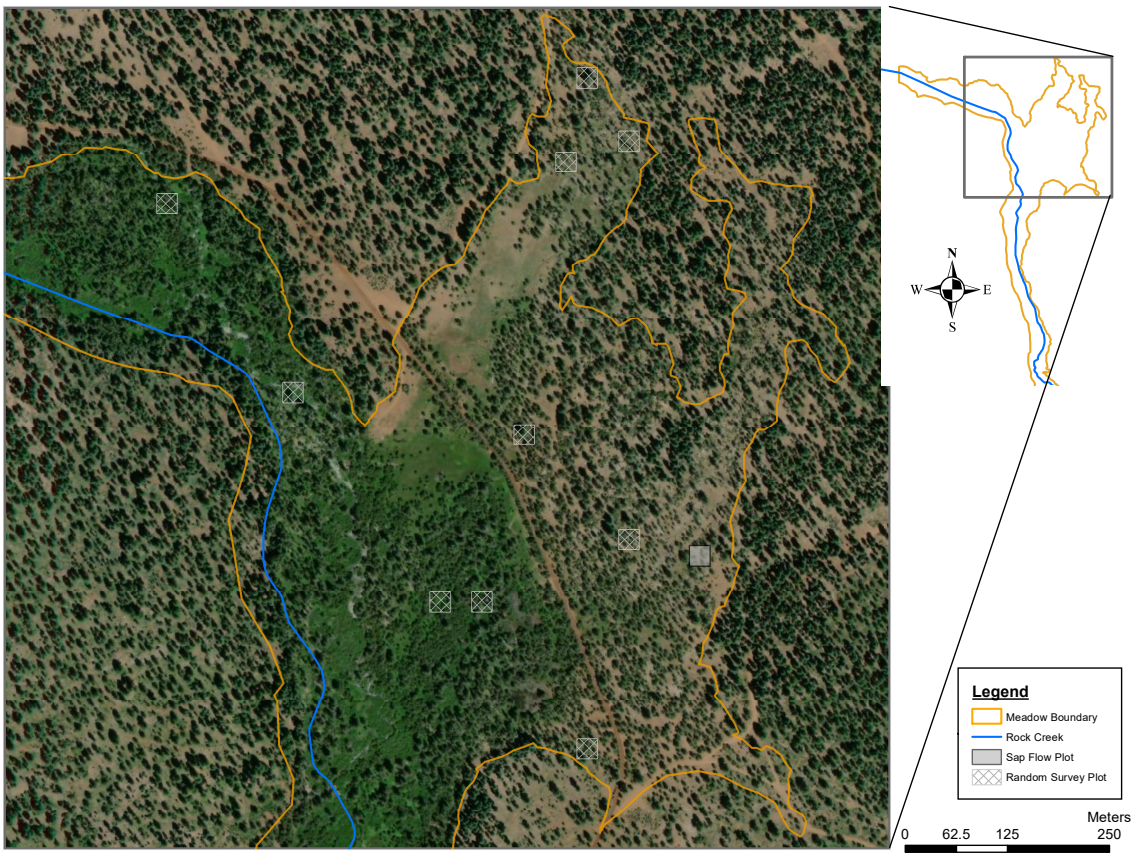

Figure B.1: RCM instrumented study area including the 25 m x 25 m SFP and random survey plots part of the stratified random sampling design overlaid on site aerial imagery (pre-restored meadow).

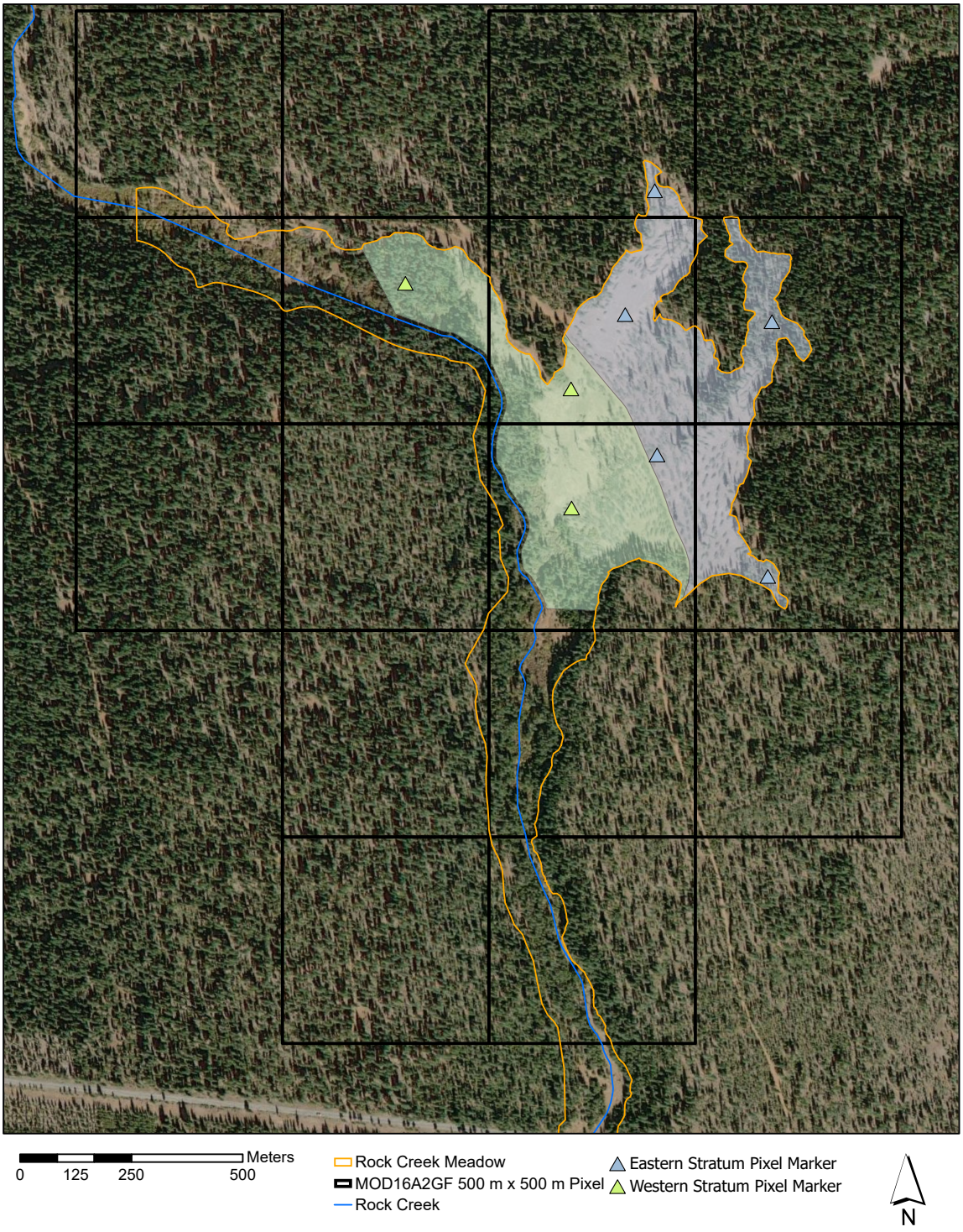

Figure B.2: RCM with overlapping MODIS Global Terrestrial ET Product pixels. The aerial imagery reflects post-restoration meadow conditions.

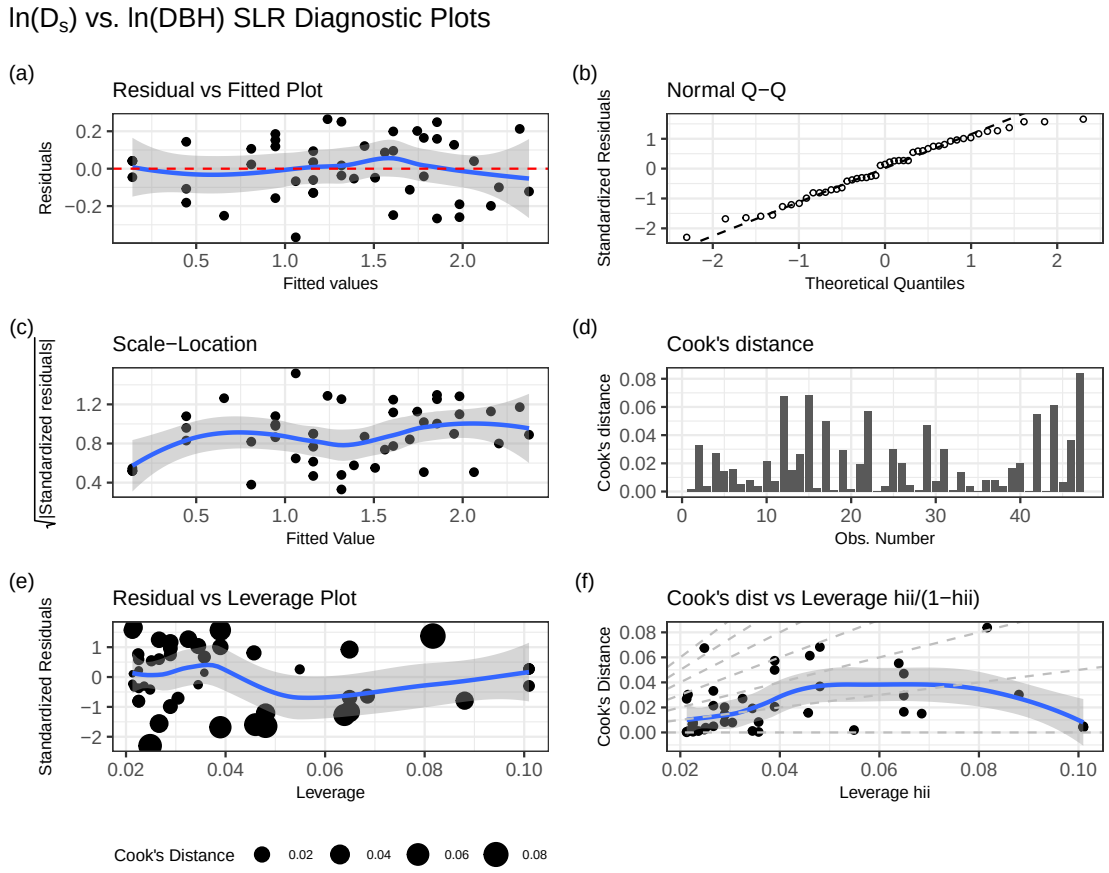

Figure C.1: Diagnostic plots for simple linear regression (SLR) assumptions- natural log sapwood depth (D_s) versus natural log diameter at breast height (DBH).

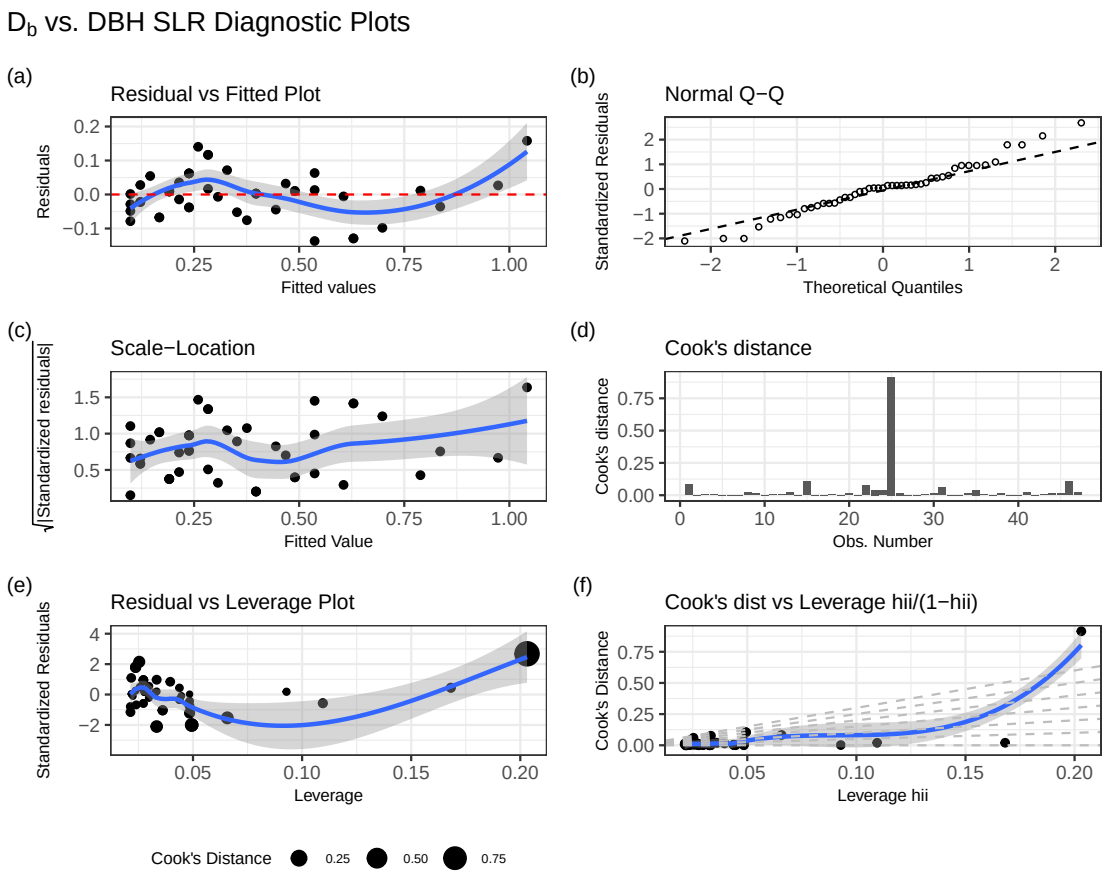

Figure C.2: Diagnostic plots for simple linear regression (SLR) assumptions- bark depth (D_b) versus diameter at breast height (DBH).

APPENDIX D: DIXIE FIRE SAP FLOW VALIDATION SITE DAMAGE

(a)

(b)

Figure D.1: Damage to the model validation sap flow site consequence of the Dixie Fire: (a) select instrumented trees and (b) sap flow enclosure/hardware.

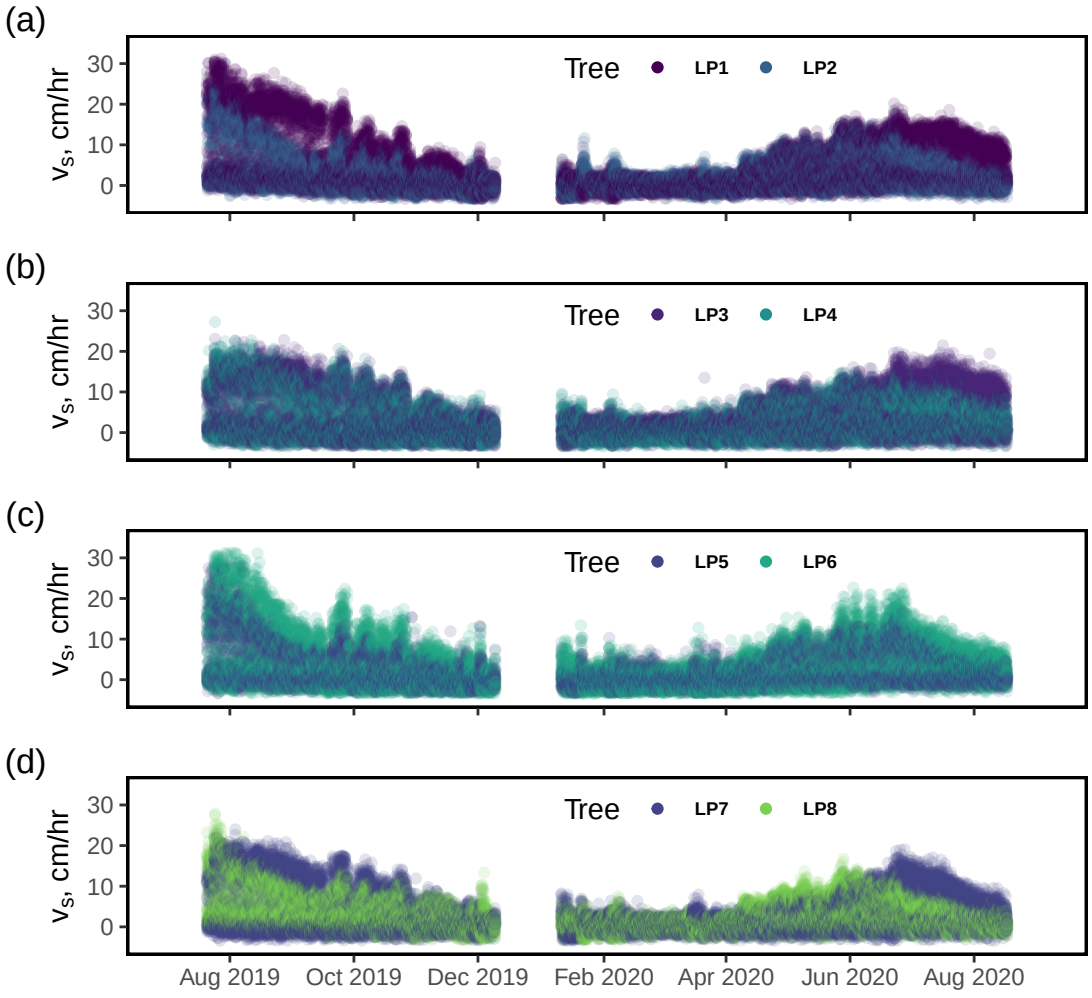

Figure E.1: 30-minute sap velocity (v_s) measurements for the sap flow plot (SFP) lodgepole pine (LP). Measurements were taken from each tree's active depth (sampled radial depth with the highest magnitude v_s): (a) LP1 and LP2 (17.5 mm); (b) LP3 and LP4 (5 mm); (c) LP5 and LP6 (5 mm); (d) LP7 (5 mm) and LP8 (30 mm).

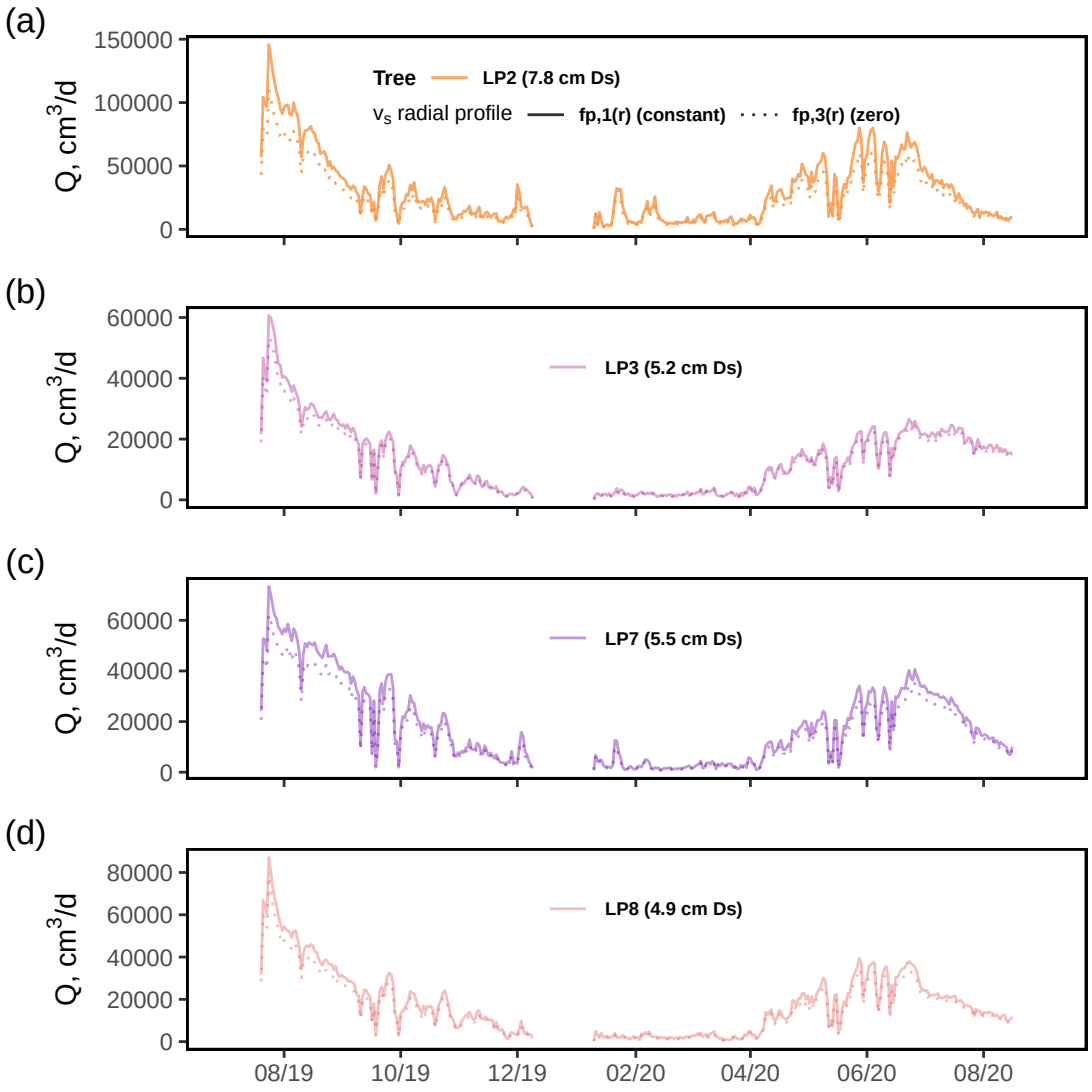

Figure E.2: Daily volumetric sap flow (Q) estimates for LP2, LP3, LP7, and LP8 given by the $f_{p,1}$ and $f_{p,3}$ sap velocity radial profiles over the sap flow plot (SFP) monitoring period. Note the differences in vertical scale used for the 4 trees.

Table E.1: Seasonal *stratum* daily mean transpiration (T) estimates by sap velocity radial profile. Italicized values represent one standard error of the mean. GS = growing season.

Season	Daily T, mm/d (***East***)			Daily T, mm/d (***West***)		
	$f_{p,1}(r)$	$f_{p,2}(r)$	$f_{p,3}(r)$	$f_{prof_1}(r)$	$f_{p,2}(r)$	$f_{p,3}(r)$
Summer 2019†	1.86	1.45	1.04	3.60	2.81	2.02
	0.15	*0.12*	*0.09*	*0.30*	*0.23*	*0.17*
Fall 2019	0.61	0.48	0.35	1.19	0.93	0.67
	0.16	*0.13*	*0.09*	*0.32*	*0.25*	*0.18*
Winter 2019†	0.12	0.09	0.07	0.23	0.18	0.13
	0.03	*0.03*	*0.02*	*0.06*	*0.05*	*0.03*
Spring 2020	0.47	0.36	0.26	0.90	0.70	0.50
	0.17	*0.13*	*0.09*	*0.32*	*0.25*	*0.18*
Summer 2020†	1.06	0.83	0.60	2.05	1.60	1.15
	0.14	*0.11*	*0.08*	*0.26*	*0.20*	*0.15*
Partial GS 2020†	0.87	0.68	0.49	1.69	1.32	0.95
	0.17	*0.13*	*0.10*	*0.33*	*0.26*	*0.15*

†T estimate incomplete for season

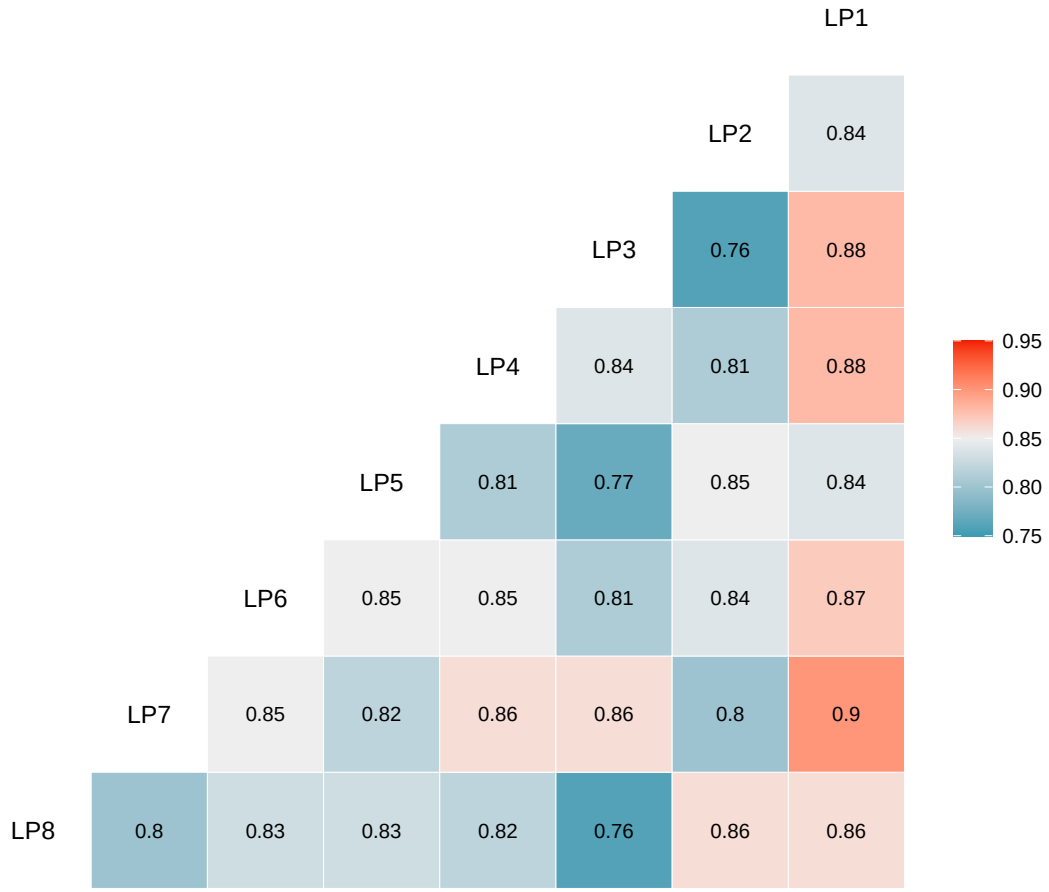

Figure E.3: Pearson correlation coefficients between active depth sap velocity measurements in the eight instrumented lodgepole pine for the SFP monitoring period (July 20, 2019 - August 17, 2020).

Table E.2: Seasonal *RCM* daily mean transpiration (T) estimates by sap velocity radial profile. Parenthetical values represent one standard error of the mean. GS = growing season.

	Daily T, mm/d		
Season	$f_{p,1}(r)$	$f_{p,2}(r)$	$f_{p,3}(r)$
Summer 2019†	2.76 (0.33)	2.15 (0.25)	1.55 (0.18)
Fall 2019	0.91 (0.19)	0.71 (0.15)	0.51 (0.11)
Winter 2019†	0.18 (0.04)	0.14 (0.03)	0.10 (0.02)
Spring 2020	0.69 (0.19)	0.54 (0.14)	0.39 (0.10)
Summer 2020†	1.57 (0.21)	1.22 (0.17)	0.88 (0.12)
Partial GS 2020†	1.30 (0.22)	1.01 (0.17)	0.73 (0.12)

†T estimate incomplete for season

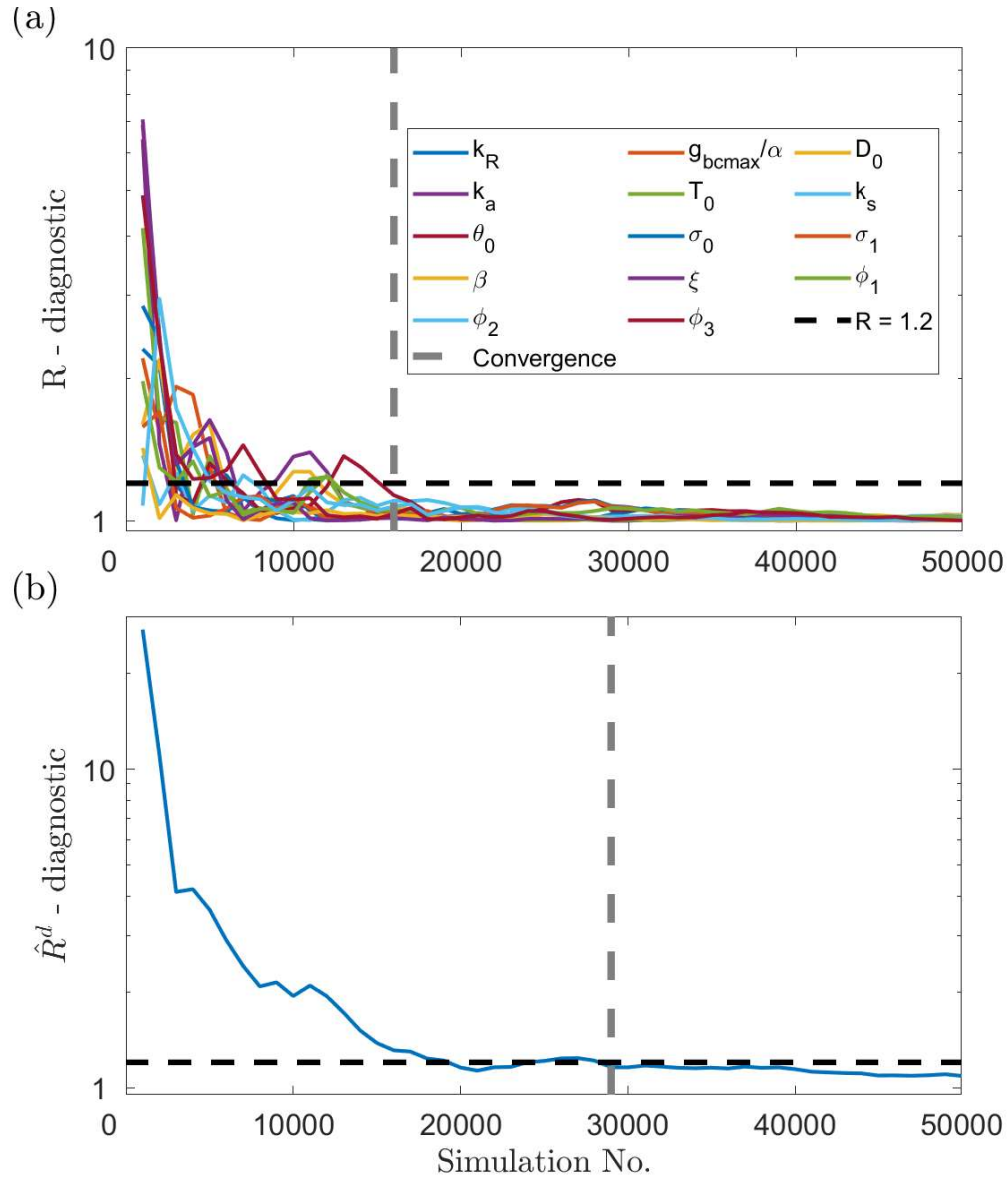

Figure F.1: (a) Convergence plot of the Gelman and Rubin (1992) R-statistic for the parameters analyzed in the modified Jarvis-Stewart (MJS) model. (b) Convergence plot of the multivariate R-statistic (R^d) (Brooks and Gelman, 1998).

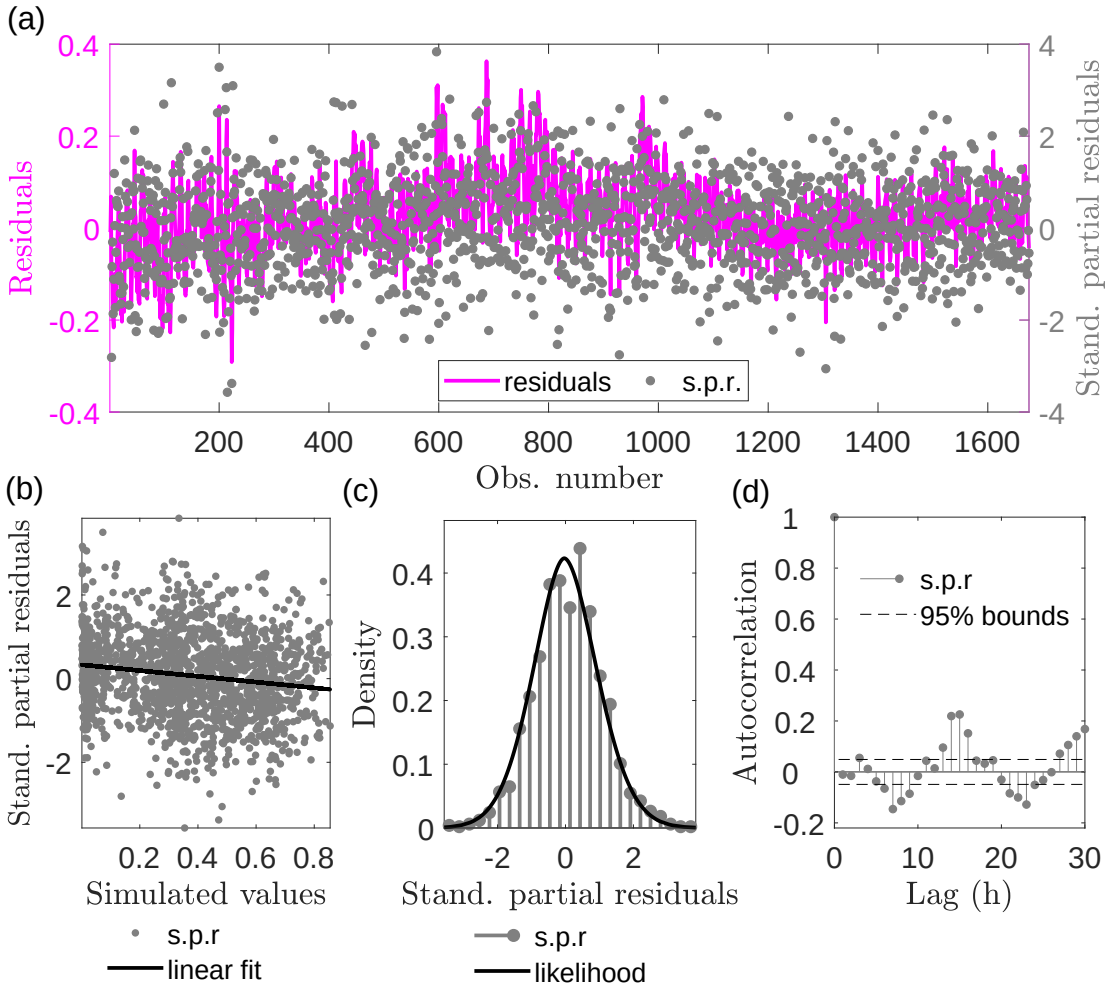

Figure F.2: Residual diagnostics for modified Jarvis-Stewart (MJS) calibration period, derived from the maximum likelihood parameter estimates (ML): (a) residual/standardized partial residual (s.p.r) versus observation order, (b) s.p.r versus simulated (predicted) values, (c) s.p.r density plot, and (d) s.p.r autocorrelation plot.

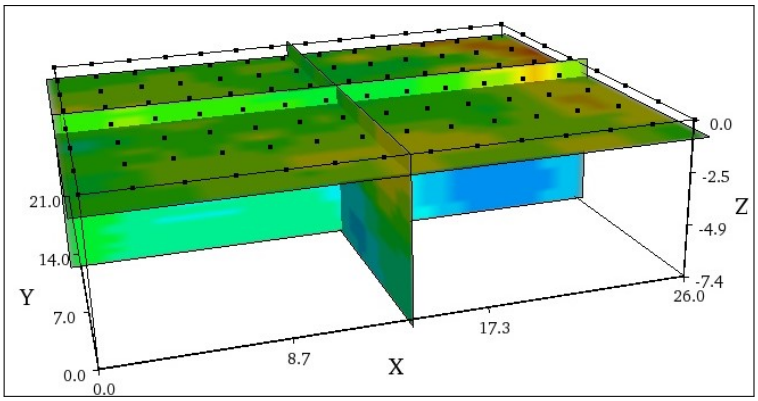

(a) July 2020 (pre meadow restoration)

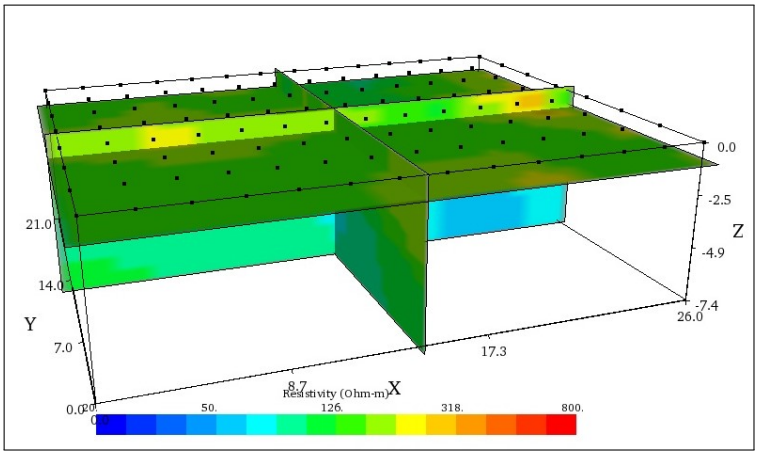

(b) July 2021 (post meadow restoration)

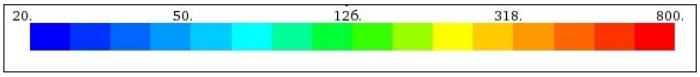

Resistivity (Ohm*m)

Figure G.1: Comparison of 3-D electrical resistivity tomography surveys for the sap flow plot (SFP) performed in (a) July 2020 and (b) July 2021. Units for axes are meters and the horizontal slice shown is at *1 m* depth.

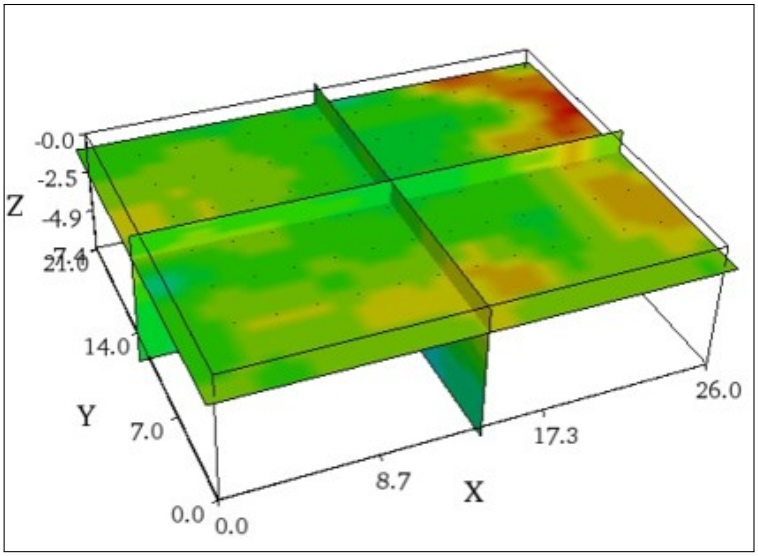

(a) July 2020 (pre meadow restoration)

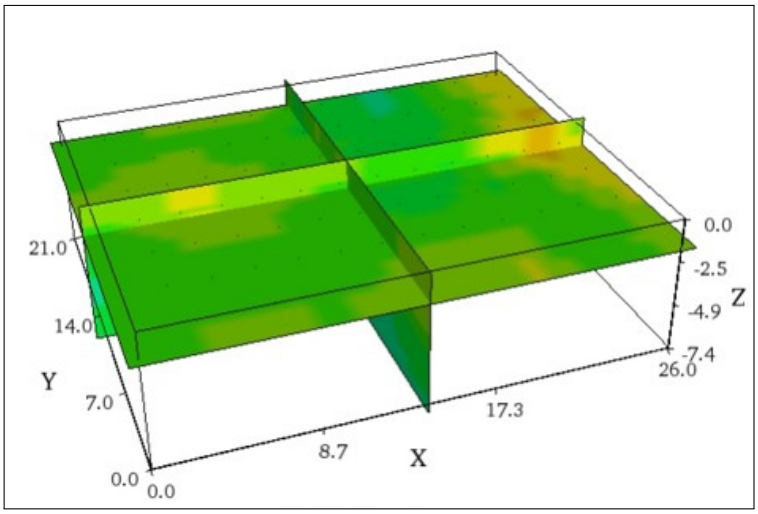

(b) July 2021 (post meadow restoration)

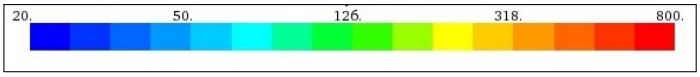

Resistivity (Ohm*m)

Figure G.2: Comparison of 3-D electrical resistivity tomography surveys for the sap flow plot (SFP) performed in (a) July 2020 and (b) July 2021. Units for axes are meters and the horizontal slice shown is at *2 m* depth.

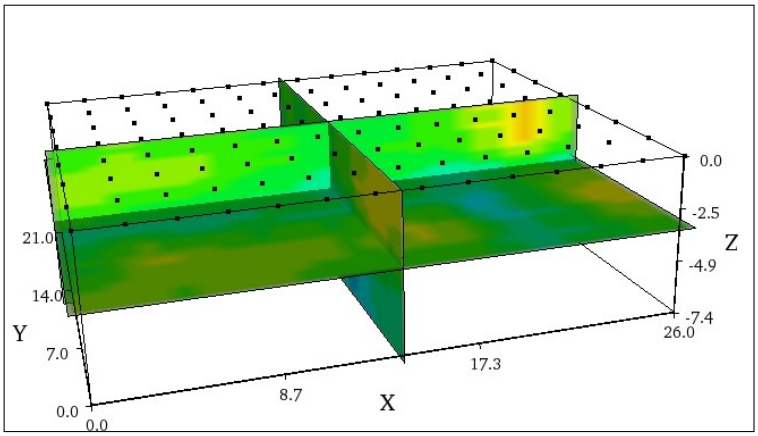

(a) July 2020 (pre meadow restoration)

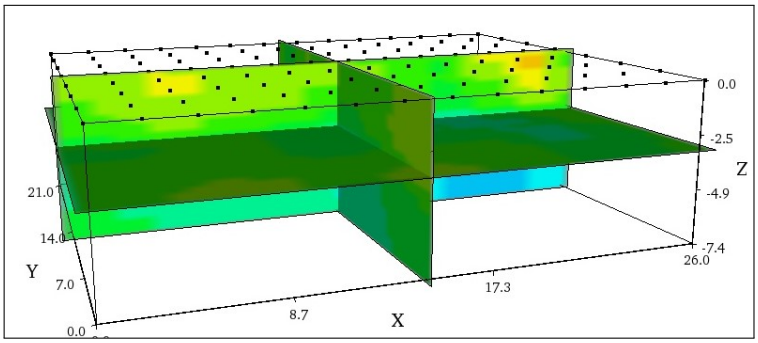

(b) July 2021 (post meadow restoration)

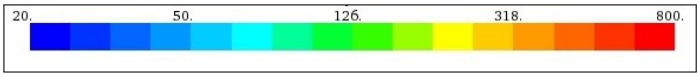

Resistivity (Ohm*m)

Figure G.3: Comparison of 3-D electrical resistivity tomography surveys for the sap flow plot (SFP) performed in (a) July 2020 and (b) July 2021. Units for axes are meters and the horizontal slice shown is at *3 m* depth.